JETIR.ORG ISSN: 2349-5162 | ESTD Year : 2014 | Monthly Issue
JOURNAL OF EMERGING TECHNOLOGIES AND INNOVATIVE RESEARCH (JETIR)
An International Scholarly Open Access, Peer-reviewed, Refereed Journal

Synthesis Characterization and Biological evaluation of Schiff base Containing Coumarine Moiety

M. S. More[1], B.G.Kharode, [1]N.V.Rathod, B.S.Bhise[2], D.L.Maske[3]
Email: more.m369@gmail.com
1. Department Of Chemistry, R.A.Art's, Shri M.K.Commerce and S.R.Rathi Scienece Mahavidhyalaya Washim. (M.S.India).
2. Department Of Chemistry, Shri Shivaji College Motala, Dist. Buldhana.
3. Department Of Chemistry, Shri Vasantrao Naik Mahavidyalaya Dharni, Dist.Amravati.

Abstracts: Schiff bases are versatile organic compounds commonly synthesized through the condensation reaction between a primary amine and an aldehyde or ketone. In the present work first coumarine was syntheses then the alkylation takes place and the Schiff base was synthesized. The physical measurement and structural elucidation by spectrum like FT-IR and 1H-NMR, used in this work.

Keywords: Coumarine, aromatic aldehyde, Ethyl acetoacetate.

Introduction:

Schiff bases containing coumarin represent a fascinating class of organic compounds with diverse applications in medicinal chemistry, materials science, and other fields. Coumarin, characterized by its unique aromatic structure fused with a lactone moiety, is widely known for its various biological activities, including antioxidant, anti-inflammatory, antimicrobial, and anticancer properties. Schiff bases incorporating coumarin moieties have attracted significant attention due to their enhanced pharmacological properties and structural versatility. The synthesis of Schiff bases containing coumarin typically involves the condensation reaction between a coumarin-derived aldehyde or ketone and a primary amine. This reaction yields a Schiff base with a coumarin scaffold, offering a platform for the design and development of compounds with tailored properties for specific applications.The incorporation of the coumarin moiety into Schiff bases imparts several advantages. Firstly, coumarin derivatives are known to exhibit fluorescence properties, making Schiff bases containing coumarin useful probes for fluorescence-based detection methods in biological and chemical sensing applications. Additionally, the presence of the coumarin scaffold can modulate the physicochemical properties and biological activities of Schiff bases, potentially enhancing their efficacy as therapeutic agents.

In medicinal chemistry, Schiff bases containing coumarin have shown promise as multifunctional agents with diverse biological activities. For instance, they have been explored as potential anticancer agents due to their ability to inhibit tumor cell proliferation and induce apoptosis. Moreover, their antioxidant and anti-inflammatory properties make them attractive candidates for the treatment of various diseases associated with oxidative stress and inflammation.

Overall, Schiff bases containing coumarin represent a versatile class of compounds with promising applications in various fields. Their unique combination of structural features, fluorescence properties, and biological activities makes them valuable tools for research and potential candidates for the development of novel therapeutics, diagnostic tools, and functional materials. Continued exploration of their chemical properties and biological functions is likely to uncover new opportunities for innovation and application in diverse areas of science and technology.Their structural versatility and potential therapeutic benefits continue to drive interest in exploring their biological activities and therapeutic potential.

EXPERIMENTAL

Solvents were employed as commercial anhydrous grade. The column chromatography was done over the silica gel (100-120 mesh). Melting points were determined in open capillary tube and are uncorrected. ^{1}H and ^{13}C NMR spectra were recorded on Bruker advance II-400 MHz spectrometer. The molar conductivity measurements of complexes in (1 × 10−3 M) DMSO solution were measured at 25 ^{0}C with a Bibby conduct meter.

Material and Methods:

All solvents were labouring as commercial anhydrous mark without further Refining. The column chromatography was carried out over silica gel (100120esh). Melting points determined by open capillary tube. ^{1}H NMR spectra were recorded on a Bruker 400 MHz spectrometer in DCl3 solvent TMS as internal standard. The crude product was recrystallizing from 80 percentage ethanol.

Present Work:

In the present work, the aromatic substituted Schiff bases were synthesized by condensing substituted amine containing coumarine moiety.

Step I: General Procedure for the synthesis of Schiff base:

The resorcinol (0.01 mole) and ethyl acetoacetate (0.01 mole) in round bottom flask containing 15ml ethanol and 3 ml of conc. Sulphuric acid was reflux for 1.5 hour a solid were obtain which is further cool and recrystallize from ethanol.

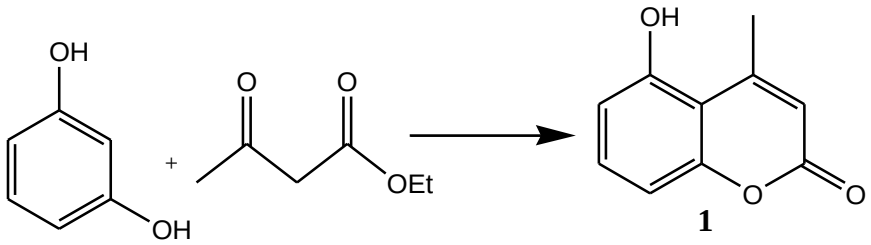

1

Scheme I

Step II :

The mixture of Coumarine (0.01 mole) and Chloroacethyl chloride (0.01 mole) in round bottom flask containing 10 ml potassium carbonate was stirred at room temperature for 1.5 hour. After completion of reaction (by TLC) the mixture was poured on ice cold water and dried at room temperature.

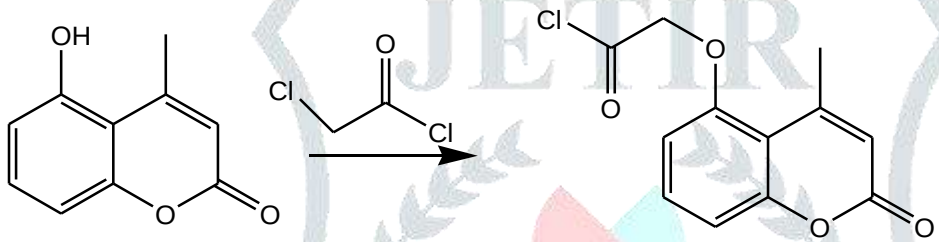

2

Scheme II

Step III:

The compound 2 was heated with hydrazine hydrate in ethanol on a water bath for 1 hour to obtain 2-[4-Methyl-2-oxo-2H-Croman-7-yl)oxy] acetohydrazide compound 3.

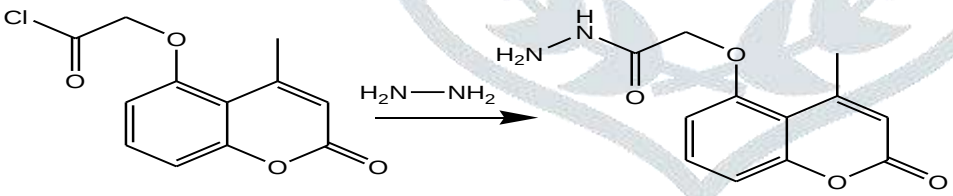

3

Scheme III

Step IV:

A mixture of alcohol (20 ml) and aromatic aldehyde (0.02 mol) was taken into a 100 ml round bottom flask. The mixture was stirred until a homogeneous solution was obtained; comarine Contain primary amine group (0.02 mol) was added with stirring. (As the reaction is exothermic it should be carried out by placing flask in a freezing mixture). Reaction mass is stirred for another 45 min. the Schiff base was precipitated out. The reaction mixture was cool with stirring. The isolated crude product is purified by the washing in acetone.

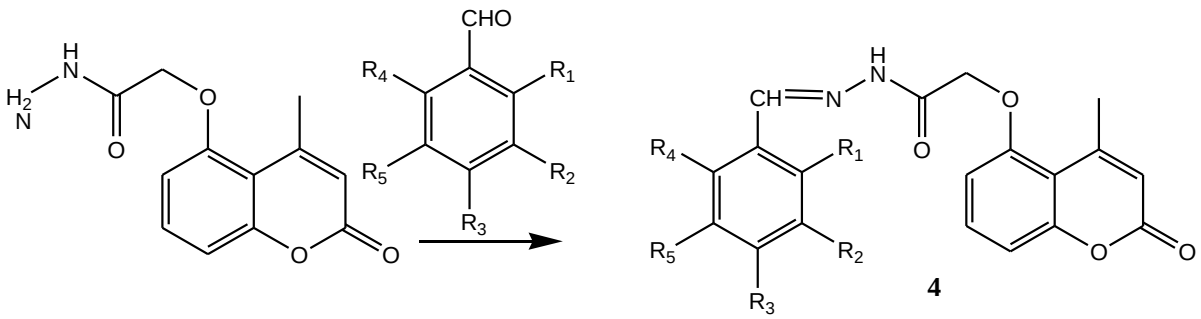

4

Scheme IV

Compound also purify by silica gel column chromatography eluent ethyl acetate hexane reaction was. Monitored by TLC & spot were visualized in iodine.

Table 1. Synthesis of M_1, M_2 M_3 & M_4 in terms of Yield and melting point

S.N.	Compound	R_1	R_2	R_3	R_4	R5	M.P.(^{0}C)	% Yield
1	M_1	H	H	H	Br	H	276	80.58
2	M_2	H	H	H	H	I	280	82.05
3	M_3	I	H	Cl	H	H	296	81.20
4	M_3	H	I	H	H	OCH_3	258	70.25
5	M_5	NO_2	I	H	H	OCH_3	270	60.25

1)**M_1**

FT-IR 660 cm^{-1} for aromatic C-C stretching, 770 cm^{-1} for aromatic C-I stretching, 1130 cm^{-1} for C-O stretching , 1620 cm^{-1} for C=N stretching , 1690 cm^{-1} for C=O stretching 1350 for C=C stretching, 1190 cm-1 for C-N stretching, 3110 for N-H stretching.

NMR :

^{1}H NMR (400 MHz, $CDCl_3$): δ 2.5 (s, 3H), δ 5.5 (s, 2H,), δ 6.6-7.6 (m, 9H), δ 8.0 (s, 1H NH), δ 8.4(s, 1H).

2) **M_2**

FT-IR, 670 cm^{-1} 1for C-I stretching, 750 cm^{-1} for aromatic C-C stretching, 1150 cm^{-1} for C-O stretching , 1070 cm-1 for C-N stretching, 1560 cm^{-1} for Ar C=C stretching, 1620 cm^{-1} for C=O stretching, 2960 cm^{-1} Ar C-H stretching 3190 for N-H stretching.

^{1}H NMR (400 MHz, $CDCl_3$): δ 2.1 (s, 3H), δ 5.5 (s, 2H,), δ 7.00-7.98 (m, 9H), δ 8.53 (s, 1H NH), δ 8.12(s, 1H).

3) **M_3**

FT-IR: 550 cm^{-1} for C-Cl stretching, 790 cm^{-1} for aromatic C-C stretching, 1060 cm-1 for C-O stretching, 1190 cm^{-1} for C-N stretching , 1440 cm^{-1} for Ar C=C stretching, 1670 cm^{-1} for C=O stretching,28100cm^{-1} Ar C-H stretching, 3120 for N-H stretching.

^{1}H NMR (400 MHz, $CDCl_3$): δ2.6 (S, 3H), δ 5.0 (S, 2H,), δ 6.20-7.98 (m, 9H), δ 8.55 (s, 1H NH), δ 8.20(s, 1H).

Antibacterial properties of the synthesized Schiff base metal complex [Zone of inhibition (mm)]

The in vitro antimicrobial activity of the investigated compounds was tested against the bacteria such as E. coli, S. aureus, by the serial dilution method. The minimum inhibitory concentration (MIC) values of the compounds against the growth of microorganisms are summarized in graph.

Antibacterial properties of the synthesized Schiff base metal complex

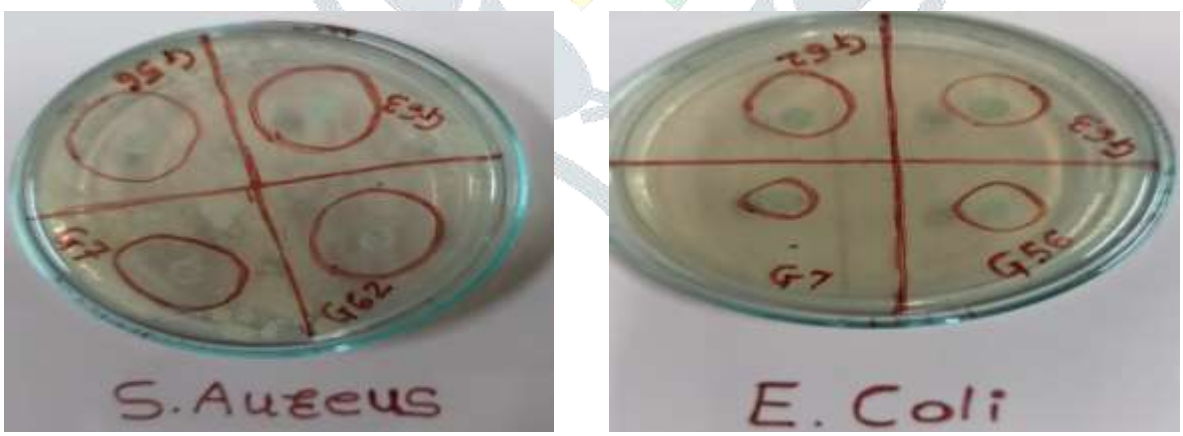

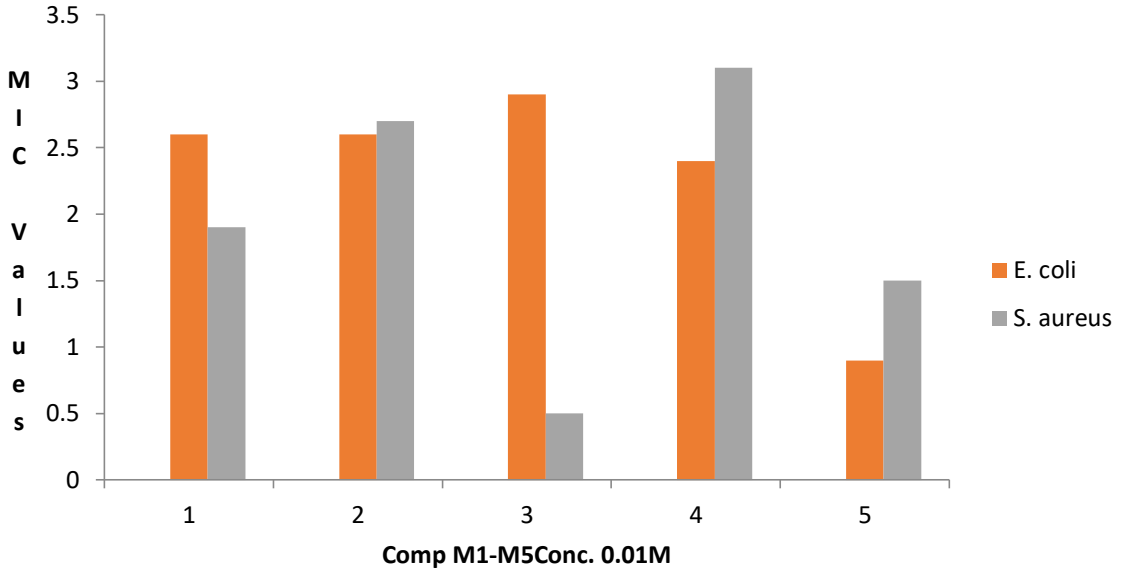

Fig : Zone of inhibition of comp. G_7, G_{56}, G_{63}, and G_{65} against S. Aureus and E. Coli.

Result and Discussion

All the six Schiff base Congaing coumarine moiety i.e. compounds M_1, M_2, M_3, M_4& M_5 were successfully synthesized in excellent yield and their structures are elucidated using elemental analysis, FTIR, & ^{1}HNMR spectroscopy. All the Synthesised Compound will screed for their biological activity.

References :

1) M.R. Grimmett, Imidazole and benzimidazole synthesis, *Academic press*, **1997**.
2) R. Sreedhar, S.V. Gadhinglajkar, Pharmacological neuroprotection, *Indian J Anaesth.* 47 (**2003**) 8–22.
3) Abu-Hussen,A.A.A.J.*Coord.Chem.***2006**,59,157.
4) Sithambaram Karthikeyan,M.;Jagadesh Prasad, D.; Poojary, B.;Subramanya Bhat,K.*Bioorg.Med.Chem.***2006**,14,7482.
5) Singh,K.;Barwa,M.S.;Tyagi'P.Eur.*J.Med.Chem.***2006**,41,1.
6) Pannerselvam,P.;Nair,R.R.;Vijayalakshim,G.;Subramanian,E.H.;Sridhar,S.K.Eur.*J.Med.Chem.***2005**,40,225.
7) Sridhar,S.K.;Saravan,M.;Ramesh,*A.Eur.J.Med.Chem.***2001**,36,615.
8) Pandeya,S.N,;Sriram,D.;Nath,G.;Declercq,*E.Eur.J.Pharmacol.***1999**,9,25.
9) Mladenova,R.;Ignatova,M.;Manolova,N.;Petrova,T.;Rashkov,I.;Rashkov,*I.Eur.Polym.J.***2002**,38,989.
10) Walsh,O.M.;Meegan,M.J.;Prendergast,R.M.;Nakib,T.A.*Eur.J.Med.Chem.***1996**,31,98.
11) Arora,K.;Sharma,K.P.Synth.React.*Inorg.Met.-Org.Chem.***2003**,32,913.

Chaos
An Interdisciplinary Journal of Nonlinear Science

RESEARCH ARTICLE | FEBRUARY 14 2024

Transition to period-3 synchronized state in coupled gauss maps

Pratik M. Gaiki ; Ankosh D. Deshmukh ; Sumit S. Pakhare ; Prashant M. Gade

Chaos 34, 023113 (2024)
https://doi.org/10.1063/5.0186541

Transition to period-3 synchronized state in coupled gauss maps

Cite as: Chaos 34, 023113 (2024); doi: 10.1063/5.0186541
Submitted: 6 November 2023 · Accepted: 19 January 2024 ·
Published Online: 14 February 2024

Pratik M. Gaiki,[1,a] Ankosh D. Deshmukh,[2,b] Sumit S. Pakhare,[3,c] and Prashant M. Gade[4,d]

AFFILIATIONS

[1]Department of Physics, Shri Shivaji Education Society Amravati's, Shri Shivaji Arts, Commerce & Science College, Motala 443103, Buldana District, Maharashtra, India
[2]Department of Scientific Computing, Modeling and Simulation, Savitribai Phule Pune University, Pune 411007, Maharashtra, India
[3]Department of Physics, Priyadarshini J. L. College of Engineering, Nagpur 440009, Maharashtra, India
[4]Department of Physics, Rashtrasant Tukadoji Maharaj Nagpur University, Nagpur 440033, India

[a)]pmgaiki@gmail.com
[b)]ankoshdeshmukh50@gmail.com
[c)]sumitspakhare@gmail.com
[d)]**Author to whom correspondence should be addressed:** prashant.m.gade@gmail.com

ABSTRACT

We study coupled Gauss maps in one dimension with nearest-neighbor interactions. We observe transitions from spatiotemporal chaos to period-3 states in a coarse-grained sense and synchronized period-3 states. Synchronized fixed points are frequently observed in one dimension. However, synchronized periodic states are rare. The obvious reason is that it is very easy to create defects in one dimension. We characterize all transitions using the following order parameter. Let x^* be the fixed point of the map. The values above (below) x^* are classified as +1 (−1) spins. We expect all sites to return to the same band after three time steps for a coarse-grained periodic or three-period state. We define the flip rate $F(t)$ as the fraction of sites i such that $s_i(3t-3) \neq s_i(t)$. It is zero in the coarse-grained periodic state. This state may or may not be synchronized. We observe three different transitions. (a) If different sites reach different bands, the transition is in the directed-percolation universality class. (b) If all sites reach the same band, we find an Ising-type transition. (c) A synchronized period-3 state where a new exponent is observed. We also study the finite-size scaling at critical points. The exponents obtained indicate that the synchronized period-3 transition is in a new universality class.

Dynamical phase transitions to an absorbing state in a spatially extended system are a nonequilibrium phase transition. They have been investigated from the phase transition viewpoint. A transition to a synchronized fixed point is an obvious candidate for an absorbing phase transition. It has a long-range order and often falls in the directed percolation universality class. We investigate a transition to a period-3 synchronized state in a coupled map lattice and show that it falls into different universality class. Such states are unlikely in one dimension. However, it is realized for weak coupling in coupled Gauss maps. We also observe a transition to an absorbing state with no long-range order. There is a three band attractor, and different sites converge to different bands at a given time. It is in the directed percolation universality class. A transition to a synchronized state of a high period, which has finitely many absorbing states, could show a departure from known universality classes.

I. INTRODUCTION

Non-equilibrium phase transitions occur in numerous situations. Of these transitions, the transition to an absorbing state is the most studied. These absorbing state transitions can be first-order or continuous. The continuous transitions are further classified into universality classes. There are very few known universality classes, such as directed percolation, the parity conservation class, the voter class, the Manna class, etc.[1] Of these, the directed percolation (DP) universality class is the most widely observed one.

DP in particle systems was found in threshold transfer processes, the Ziff–Gulari–Barshad model[2] and Domany–Kinzel automata.[3] It has been argued that all transitions from a fluctuating phase to a unique absorbing state is in a DP class under the most conditions.[4,5] The conditions are (a) the transition is characterized by a non-negative one-component order parameter, (b) the system has no special attributes, such as unconventional symmetries, conservation laws, or quenched randomness, (c) the transition is to a unique absorbing state from a fluctuating active phase, and (d) couplings are short-range. The exponents change if couplings are not short-range.[6] The question could be asked what happens if these prerequisites are relaxed. The transition is found to be very robust under the relaxation of many conditions.[7] This universality class can be observed even if the absorbing state is unique or has no long-range order in space.[8,9] We will present an example of a DP transition without long-range spatial order or a unique absorbing state in this work.

The synchronization transition is a transition to an absorbing state with long-range order. There are numerous instances of the occurrence of a synchronization transition in nature and society. A few examples of these are the synchronous flashing of fireflies and the chirping of crickets. On lattices, these transitions are often found to be in the DP universality class.[10] In this work, we show that even for an absorbing state with long-range order, we may not observe the DP universality class. On the other hand, we may observe it in systems, which can have infinite absorbing states in the thermodynamic limit and no long-range order.

A short review of absorbing state transitions other than DP may be in order. Apart from DP, a few other universality classes are studied. The directed Ising class is observed in a system with $\mathcal{Z}_2$ symmetry. It is observed in systems, such as nonequilibrium kinetic Ising models,[11,12] Grassberger's A and B models,[5,13] branching and annihilating random walks with two off-springs,[14–16] and the interacting monomer–dimer model.[17] Another notable universality class is the voter university class observed in several opinion formation models. In one dimension, the voter class is the same as the compact-directed percolation class and can be mapped to an equilibrium model.[1] There has been a long debate on whether the pair contact process with diffusion (PCPD) is a distinct universality class,[18,19] though it is likely that for large sizes and times, the PCPD falls in a DP universality class.[20] A new non-Markovian quantity called persistence is defined in this context. The persistence exponent has also been used to characterize these transitions. For example, coupled logistic maps with feedback are studied with linear or nonlinear coupling for different feedback times. Surprisingly, in this work, it was observed that ten different systems fall into two different classes. The classes depend on whether the system shows ferromagnetic or antiferromagnetic order at the transition.[21] One of the transitions observed in this paper is also an Ising-type transition, though the microscopic elements do not have Ising symmetry.

We work on a coupled map lattice model and focus on dynamic phase transitions. These are defined in thermodynamic and asymptotic limits. Phases are defined by the asymptotic states of an infinite system. We must mention that relatively fewer studies have been carried out on models involving continuous variable values. The DP universality class is observed in coupled circle maps[22,23] and piecewise linear maps.[24] The transition in the logistic map with delay (which can be mapped on a pseudospatiotemporal system) molds into the directed Ising universality class.[25] For some maps, we can observe transitions in the $q = 3$ Potts class in coupled map lattices.[26] In coupled logistic maps, the transition to an anti-ferromagnetic state is found to be in the Glauber–Ising class.[27] Studies in these systems have taken place in higher dimensions too. A study of the possibility of transitions in equilibrium and non-equilibrium classes has been made in two dimensions. Miller and Huse proposed the possibility of transitions in a coupled map lattice to the Ising class in two dimensions.[28] It has been argued that the nature of the update affects the universality class.[29–31] For example, it has been shown that a certain coupled map lattice model is in DP class only when the update is asynchronous.[29]

Apart from synchronization to fixed points, other types of synchronization, such as phase synchronization,[32] generalized synchronization,[33] chaotic synchronization,[34] etc., are studied in the literature. However, there are not many studies from a phase transition viewpoint. It is now well understood that chaotic synchronization requires nonlocal coupling because it requires a gap in the eigenvalue spectrum of the underlying connectivity matrix.[35] It is not possible with short-range coupling in any dimension. Can we have a periodic synchronized state in one dimension? Such states are observed in a globally coupled map.[36] However, we are not aware of such a state in one dimension with random initial conditions in the infinite lattice limit. The reason is simple. It is very easy to destroy the order in one dimension.[37] The domain walls do not have curvature and need not shrink in time. Thus, such states are not easy to realize in one dimension with random initial conditions and in an infinite lattice limit. In this work, we provide one such instance. We observe a synchronized period-3 state; i.e., the entire lattice goes through a synchronized (P, Q, R) cycle and is in a synchronized P (or Q or R) state after every three time steps. There are three such asymptotic attracting states, and departures from DP universality class are not ruled out. We indeed observe that this transition does not fall in the DP universality class. We also observe a transition to an unsynchronized state, which has a three-period in a coarse-grained sense. Each site is not exactly periodic but returns to the same band after three time steps. Infinitely, many such states are possible in the thermodynamic limit. Interestingly, this transition falls into the DP universality class. (If there are three bands, there are 3^N possible frozen configurations. Even if all of them are not realized, they will grow with N and there are infinitely many possible configurations in the thermodynamic limit.) We use the same order parameter for all transitions away from the states that have a period 3 at least in a coarse-grained sense. For the transition in a DP class, there are infinitely many absorbing states without long-range order. On the other hand, we observe a new universality class when there are finitely many (three) possible asymptotic states with long-range order. When the entire lattice goes to a single band, we observe an Ising-type transition. Thus, a rich variety of phase transitions are observed in a single system.

II. MODEL

The Gauss map is a one-dimensional map based on the Gaussian function. (It should not be confused with the term "Gauss map" used for a surface in differential geometry, and this map can be better described as shifted Gaussian. However, we stick to this name

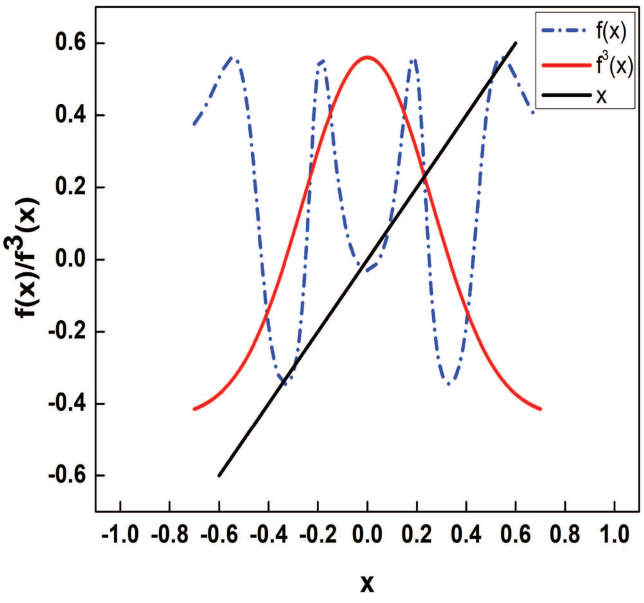

FIG. 1. We plot Gauss map $f(x)$ for $\nu = 7.5$ and $\beta = -0.44$. The function $f^3(x)$ is also plotted to show the possibility of period-3 in this map.

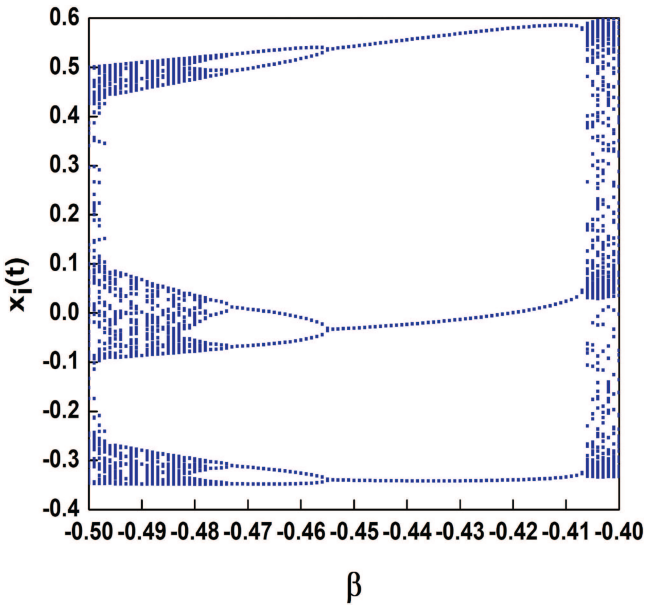

FIG. 2. We plot a bifurcation diagram for a single Gauss map for $\nu = 7.5$. We observe the range of dynamical behaviors from period 3 to a chaotic orbit.

because it is widely used for this iterative map.) It is defined as

$$f(x) = \exp\left(-\nu x^2\right) + \beta, \quad x \in \mathbb{R}, \tag{1}$$

where ν and β are map parameters. We fix the parameter $\nu = 7.5$ in our work. This function is a Gaussian shifted by β with variance proportional to $1/\nu$. It is not a map of the interval and shows phenomena, such as period-adding.[38] Because the map is defined over the entire real line, we can consider both positive and negative coupling for a coupled map lattice. We show the function and its third iterate in Fig. 1 for $\beta = -0.44$. The fixed points of $f^3(x)$ that do not match with the fixed points of $f(x)$ represent period-3. (The map rapidly goes to β for larger values of x, and hence, only the relevant range is shown.) For this map, period-3 is observed for $-0.454 < \beta < -0.407$. The bifurcation diagram of a single map is shown in Fig. 2.

We define a coupled map lattice as follows. Consider a lattice of length N. Let $x_i(t)$ be the variable at site i at time t. We assume periodic boundary conditions; i.e., the last site is connected to the first site. The evolution of $x_i(t)$ at discrete time t is given by the following equation:

$$x_i(t+1) = (1-\varepsilon) f(x_i(t)) + \frac{\varepsilon}{2}\left[f(x_{i+1}(t)) + f(x_{i-1}(t))\right], \tag{2}$$

where ε is the strength of diffusive coupling. In all simulations, $x_i(0)$ are chosen from random initial conditions in a unit interval. For $\varepsilon = 0$, we restore the single uncoupled map. This is a purely local coupling. We study the dynamics in the vicinity of the existence of the period-3 state. For small couplings, we expect the period-3 state to exist for a single map for both positive and negative coupling. We refer to Fig. 1 again. It shows seven fixed points of the function $f^3(x)$, one of which is also a fixed point for $f(x)$. The line $y = x$ is also shown as a reference. From Fig. 1, it is clear that the three fixed points with a positive slope have a slope greater than 1 and are, thus, unstable. There are three points with a negative slope. For $\beta = -0.44$, it can be verified that they have a slope fixed greater than -1 and are stable. One of these fixed points is above the fixed point x^* of $f(x)$ and the other two are below it. Thus, the period 3 orbit is expected to be below (above) x^* after every three iterates.

The effective way to visualize the dynamics of the system is the bifurcation diagram. We plot the bifurcation diagram of this system. For $N = 200$ maps, variable values of all sites are shown after $t = 4990$ time steps for the next 10 time steps. We plot $x_i(t)$ for all sites as a function of β for the fixed coupling parameter ε for $4990 < t \leq 5000$. The bifurcation diagram for both attractive $\varepsilon = -0.03$ and repulsive $\varepsilon = 0.03$ coupling parameters is shown in Fig. 3. We find that there are four points at which the three-period or a three-band attractor is lost, and we observe spatiotemporal chaos. This work focuses on these transitions. We study them as dynamic phase transitions and investigate their universality class because transitions from three-band or three-period states are not investigated to the best of our knowledge. A phase is defined only in the asymptotic and thermodynamic limits. Thus, this investigation demands systematic investigation of long-time properties of large lattices.

As noted above, two of the three bands of the three-band state or two of the periodic states of the three-period state are expected to be below or above the fixed point. This observation motivates us to identify the following order parameters for a three-band or three-period attractor. Let x^* be the fixed point of the Gauss map. (This is a transcendental equation, and the fixed point is obtained numerically using the bisection method.) We associate the spin $s_i(t) = 1$ for

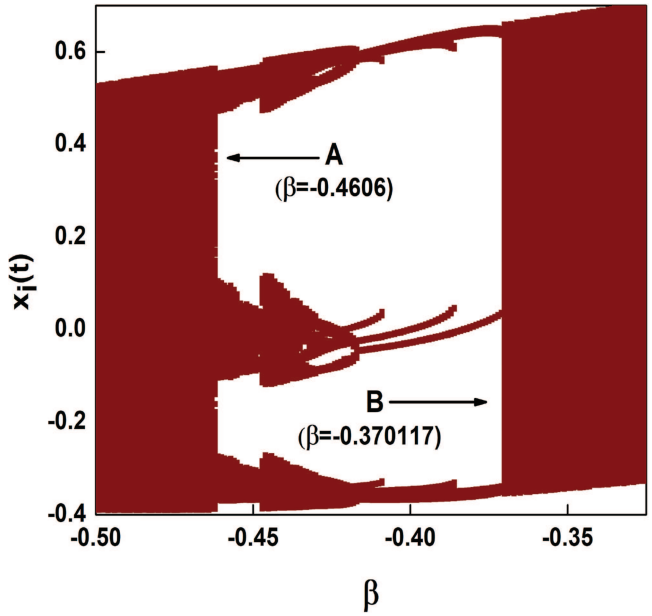

(a)

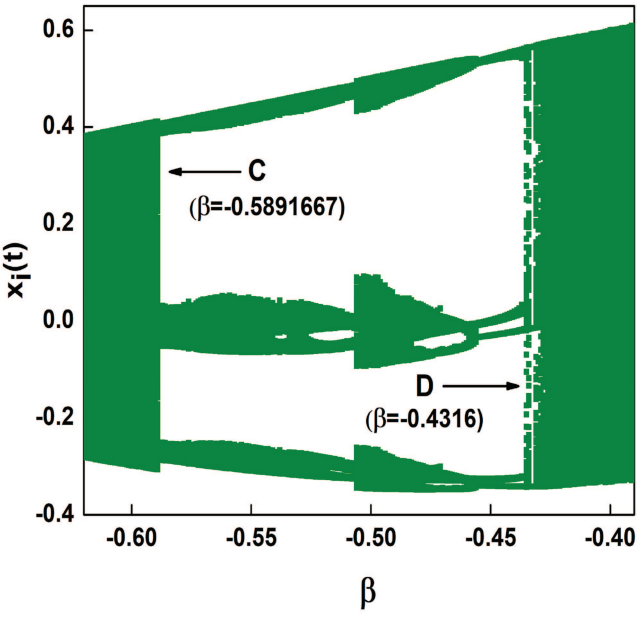

(b)

FIG. 3. We plot a bifurcation diagram for a coupled Gauss map for $\nu = 7.5$. We consider $N = 200$ and simulate it for $t = 5 \times 10^3$ and plot the last ten time steps. (a) For $\varepsilon = -0.03$. (b) For $\varepsilon = 0.03$. In this figure and all other figures, we start with uniform random initial conditions in a unit interval [0:1]. (Choosing a uniform initial condition between [−0.5:0.5] does not change the results.)

$x_i(t) > x^*$ and $s_i(t) = -1$ for $x_i(t) < x^*$. If the period is 3, we expect $s_i(3t+3) = s_i(3t)$. Any departure from the periodic state will lead to $s_i(3t+3) \neq s_i(3t)$. We define flip rate $F(t)$ *as a fraction of sites* i *for which* $s_i(3t) \neq s_i(3t-3)$. In other words, fraction of sites i such that $s_i(3t-3) \neq s_i(3t)$. $F(t) = \frac{1}{2N}\sum_{i=1}^{N} |s_i(3t) - s_i(3t-3)|$. The flip rate is zero for the periodic (or periodic in the coarse-grained sense) state and is nonzero otherwise. If all the sites with value $x < x^*$ stay below x^* after three iterates and all the sites with value $x > x^*$ stay above x^* after three iterates, the flip rate will be zero at that time. We fix the value of ε and find the value of a below which the flip rate goes to zero asymptotically. We would like to explore whether this order parameter that can shed light on changes in the structural properties of dynamics is affected by changing the control parameter.

Apart from the flip rate, another quantity we study at these critical points is persistence. It is the probability that the local value of a fluctuating nonequilibrium field does not change its sign until time t.[39–41] In the context of spin systems, the persistence $P(t)$ at time t is the fraction of spins that did not change their initial spin state even once until the given time.[27] We use modulo-3 time and define that *a site* i *is persistent until time* t *if* $s_i(3t') = s_i(0)$ *for all* $t' \leq t$. Nonzero persistence implies that at least a part of the system retains the memory of its initial conditions until that time. This is a non-Markovian quantity. It may exhibit a power-law decay at the critical point; the decay exponent can be said to be the persistence exponent. If $P(t) \sim t^{-\theta}$ at the critical point, θ is called the persistence exponent. Persistence exponents belong to a novel class of exponents, which are different from the commonly observed critical exponents. In our work, we study the behavior of persistence with time for critical points at which there is a transition to a coarse-grained or synchronized period-three state.

We observe two transitions to spatiotemporal chaos from the three-band state for $\varepsilon = -0.03$. These are labeled as A and B in the bifurcation diagram. We observe two transitions, one to a three-band state and the other one to a three-period state for $\varepsilon = 0.03$ as well. They are labeled as C and D in the bifurcation diagram for positive coupling. These four transitions fall into three different classes. The spatial profile at the transition points gives an idea of possible long-range order at the transition point. Only in one case, do we observe exact synchronization (Point D). In another case, we observe band synchronization (Point A). We could say that all sites are in the same band. However, in two of the cases, we observe that different sites approach different bands (Points B and C). This system converges to a state without any long-range spatial order (exact or coarse-grained) in space. (It still has a coarse-grained periodicity of period-3.)

For point A, where a single band is observed, the spatiotemporal dynamics are shown in Fig. 4. The three bands diffuse and annihilate, and we observe a single band asymptotically. Thus, there is a coarse-grained long-range order.

For points B and C, the sites reach a band-periodic state with period 3. However, different sites reach different asymptotically. Thus, there is no long-range order. However, the differential of the current spin values $s_i(3t)$ with the spin value three-time steps before; i.e., $s_i(3t-3)$ reaches zero. We plot defects for which $s_i(3t) \neq s_i(3t-3)$ as a function of time before the absorbing state is reached. We observe that the defects spread in a cone and

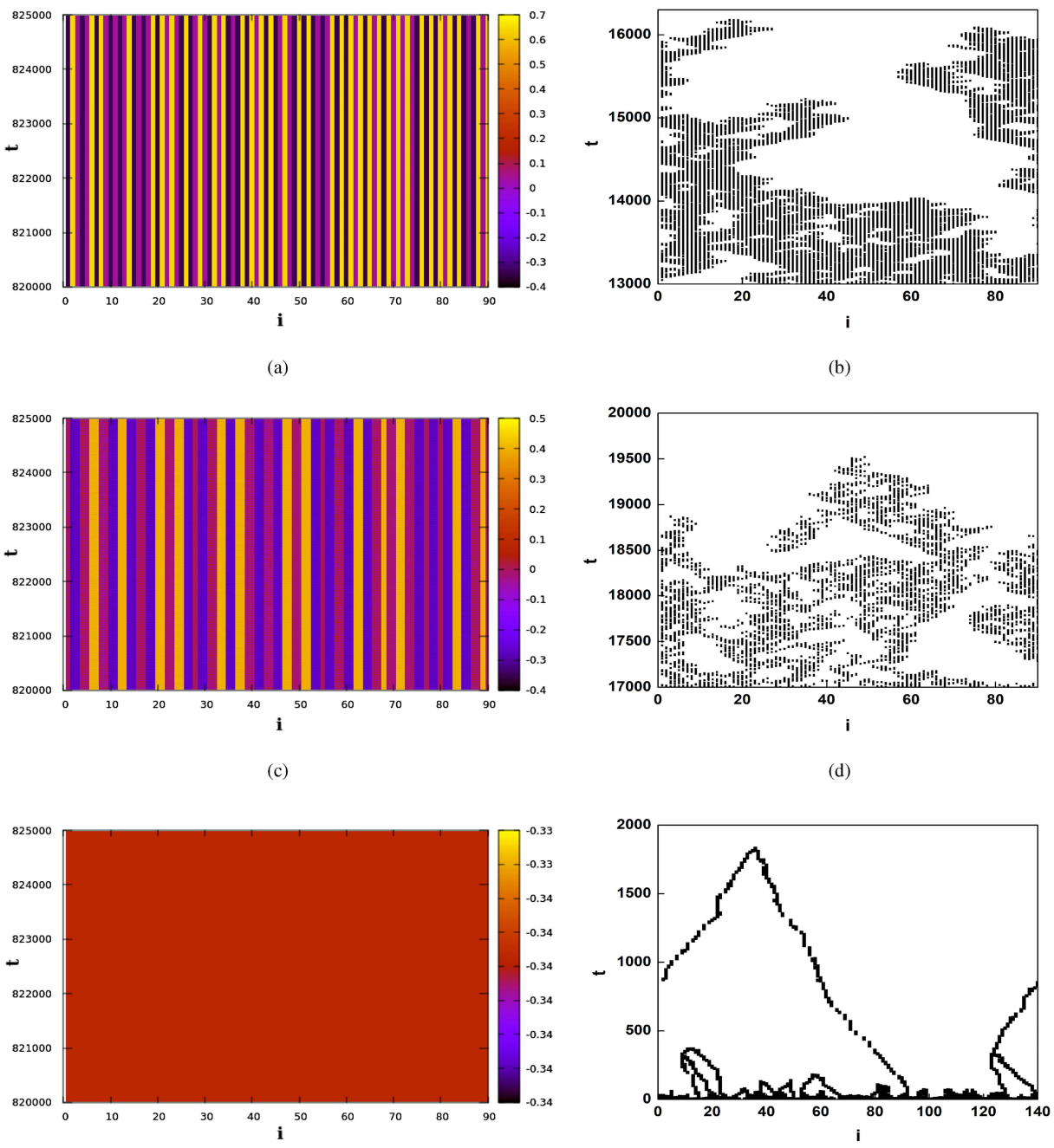

FIG. 5. Space-time plots for close to different transition points for points. The time is modulo-3. For Point B ($\varepsilon = -0.03$, $\beta = -0.370\,117$) and point C ($\varepsilon = 0.03$, $\beta = -0.589\,166\,7$), we observe a band-periodic state where periodicity is 3 in time with no long-range order in space. For point D ($\varepsilon = 0.03$, $\beta = -0.4316$), we see a clear synchronization of all sites to a period-3 state. If $x_i(3t-3) < x^*$ and $x_i(3t) > x^*$ or $x_i(3t-3) < x^*$ and $x_i(3t) > x*$, we have defect at site i at time t. The defects are represented by black dots. (a) We show an asymptotic color-coded heat map at B. Different sites converge to different bands. (b) Defect dynamics at B is similar to directed percolation. (c) The asymptotic heat map at C shows the same feature. (d) Defect dynamics at C is also similar to directed percolation. (e) The asymptotic heat map at D shows clear synchronization of all sites to a period-3 state. (f) Defect dynamics at D shows drifting and merging defects, which is very different dynamics than those observed at B and C.

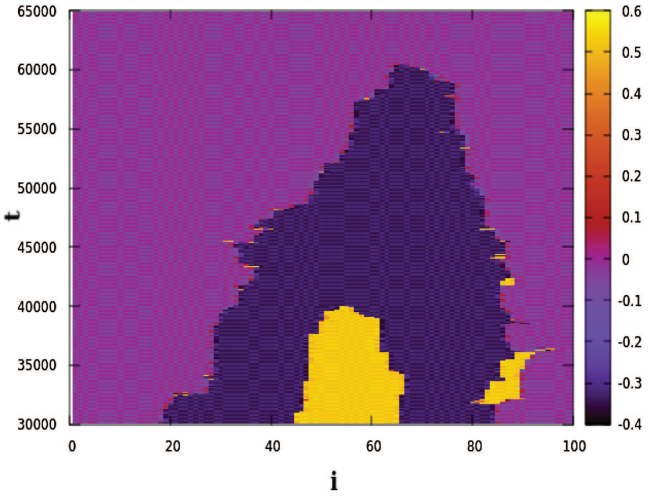

FIG. 4. Space-time plot for $\varepsilon = -0.03$, $\beta = -0.4607$ close to transition point A ($\varepsilon = -0.03$, $\beta = -0.4606$). The time is modulo-3. We observe that all sites reach the same band asymptotically at A.

annihilate. The asymptotic spatiotemporal states as well as initial defect dynamics are shown in Fig. 5.

At D, the sites get synchronized and show a period-3 state. The defects show some preferred direction and drift. They annihilate on the meeting (see Fig. 5).

The asymptotic spatial profile at critical points A, B, C, and D is shown in Fig. 6. The differences in the nature of the transitions are clear from the asymptotic spatial profile. We note that it is not clear from the bifurcation diagram alone.

Interestingly, all these transitions are continuous. We study the behavior of the order parameter defined above in all four cases. In all cases, the flip rate $F(t)$ approaches zero as a power-law at the critical point. For the transitions A, B, C, and D, we find that $F(t) \sim t^{-\delta_A}$, $F(t) \sim t^{-\delta_B}$, $F(t) \sim t^{-\delta_C}$, and $F(t) \sim t^{-\delta_D}$ at the transition points A, B, C, and D. For transitions B and C leading to a state where different sites approach different bands, we find that the critical exponent $\delta_B = \delta_C \sim 0.16$ indicating a directed percolation universality class. For transition A, we observe $\delta_A = 0.5$, which is like the Ising class. However, for transition D, we obtain a new exponent $\delta_D \sim 0.82$, which is not observed before [see Fig. 7(a)–7(d)].

In Fig. 7(b), we have plotted the evolution of the order parameter as a function of time for the critical point B. This is an absorbing state in a coarse-grained sense. The critical exponent obtained $\delta_B = 0.16$ is close to the exponent 0.1585 observed for 1-d directed percolation. We note that such a transition to a fully absorbing state in the coarse-grained sense at all times (modulo-2) has been noted previously.[8] This is yet another example showing that absorbing states without long-range order can show a directed percolation transition with appropriate modification in the definition of the order parameter. This state is not unique, and an infinite number of possible states are possible in the thermodynamic limit. Each site can be in three possible bands and the number of possible absorbing states is 3^N. Even if all of them are not realized, the number will grow with size and there are infinite absorbing states in the thermodynamic limit. This shows the robustness of a directed percolation transition even after dropping the prerequisite of a unique absorbing state.

The same transition to a band-state is observed at critical point C, and we obtain an exponent close to the exponent obtained for directed percolation. In Fig. 7(c), we have shown $F(t)$ as a function of time at critical point C. We find that $F(t) \sim t^{-\delta_C}$ with $\delta_C = 0.16$, which is close to the expected value for 1-d directed percolation.

Now, we consider the transition where all sites do not get synchronized but reach the same band. In Fig. 7(a), we have shown $F(t)$ as a function of time at critical point A. We find that $F(t) \sim t^{-\delta_A}$ with $\delta_A = 0.5$. The exponent is close to the Ising transition in 1d. This is surprising because the system does not have two states linked by symmetry. It does not have Ising symmetry or $\mathcal{Z}_2$ symmetry. It has three absorbing states in a coarse-grained sense.

Finally, we consider the most interesting case of a transition to a fully synchronized state with period 3. So far, an exactly synchronized state (apart from a synchronized fixed point) has not been obtained in coupled map lattice to the best of our knowledge. There are three possible absorbing states, which differ in phase. If (P, Q, R) is a three-period orbit, all sites could be synchronized to P or Q or R at times modulo-3. The flip rate $F(t)$ is plotted as a function of t at critical point D [Fig. 7(d)]. We observe $F(t) \sim t^{-\delta_D}$ with $\delta_D = 0.82$, which is a new exponent signaling a new universality class. Thus, though the directed percolation universality class is recovered when there are infinite possible absorbing states, there is a departure from known universality classes when there are three possible absorbing states.

For further characterization of the transitions, we carry out finite-size scaling at the critical points. We simulate the system at different sizes N at the critical point and a scaling collapse is expected if we plot the scaled order parameter $F(t)N^{z\delta}$ as a function of scaled time t/N^z for $N = 50$, 100, 200, 400, 800, and 1600. An excellent scaling collapse is observed for a transition at the critical point B for $z = 1.59$ and $\delta = \delta_B = 0.16$ (see Fig. 8). This value of z is close to the expected value of 1.58 for a DP transition. The transition at the critical point C is similar to the point B, and we expect the same dynamic exponent there.

For critical point D, the power law is followed by a cusp at any finite size. This is followed by sharp decay. The location of the cusp goes like $1/N$. However, the time taken for complete decay of $F(t)$ scales like $1/N^2$. Hence, we obtain an excellent scaling collapse by plotting $F(t)N^{z\delta_D}$ as a function of t/N^z for $N = 50$, 100, 200, 400, and 800 for $\delta_D = 0.82$ and $z = 2$, which captures the latter behavior (see Fig. 9).

Now, we study the persistence exponent at these critical points. At point A, we do not observe a well-defined persistence exponent. However, at points B, C, and D, we find that $P(t) \sim t^{-\theta_B}$, $P(t) \sim t^{-\theta_C}$, and $P(t) \sim t^{-\theta_D}$, respectively. In Fig. 10, we plot $P(t)$ as a function of t at points B and C. At points B and C, we obtain $\theta_B = \theta_C = 1.5$. This exponent matches the exponent observed in several models with a 1D DP transition.[2,3,42] We observe a well-defined persistence at D as well with $\theta_D = 1.1$. Thus, we expect $P(t)t^{\theta_D}$ to approach a constant asymptotically. This is what we observe in Fig. 11.

To investigate how generic the transition at D is, we investigate it at other values of ε. We find that the same transition

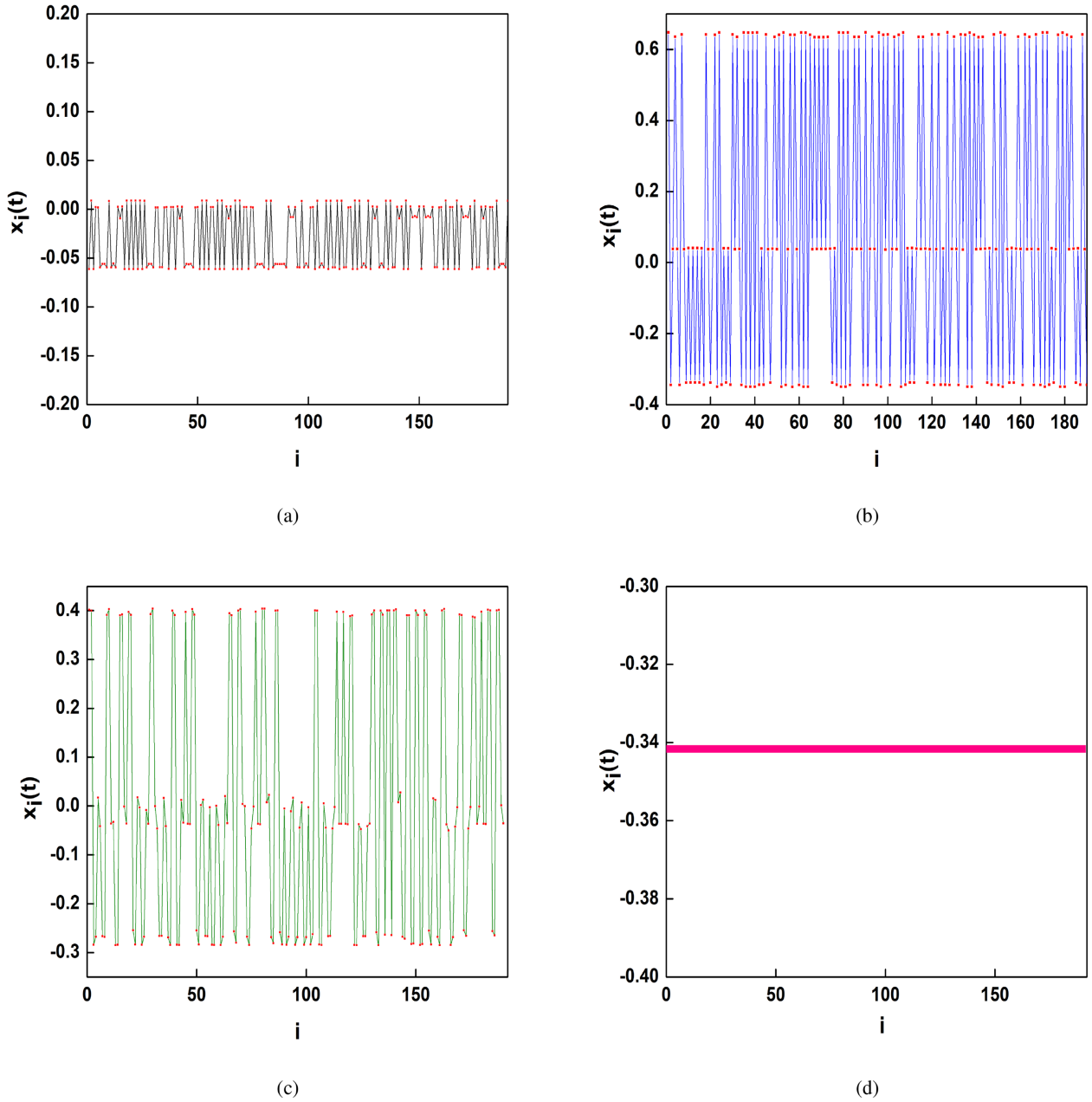

FIG. 6. Typical asymptotic spatial profile at A, B, C, and D is shown in (a)–(d). We plot $x_i(t)$ as a function of i for $t = 8.25 \times 10^5$. We find that all sites are in the same band at A showing a coarse-grained long-range order. At B and C, there is no long-range order, though the site returns to the same band after three time steps. Different sites are in different bands. At D, we observe a synchronized period 3 state, and the lattice is synchronized and periodic with period 3. In (d), the y axis has range [-.4:-.3] for visibility. The sites are synchronized.

is observed for $\varepsilon = 0.01$, $\varepsilon = 0.02$, and $\varepsilon = 0.04$ apart from $\varepsilon = 0.03$. (Of course, the critical value of β is different.). The flip rate decays with the exponent close to 0.82 in all these cases (see Fig. 12).

III. RESULTS AND CONCLUSIONS

We have studied various transitions from a three-period or three-band state in coupled Gauss maps. We define the order parameter flip rate, which is zero if all the sites are stuck in the same

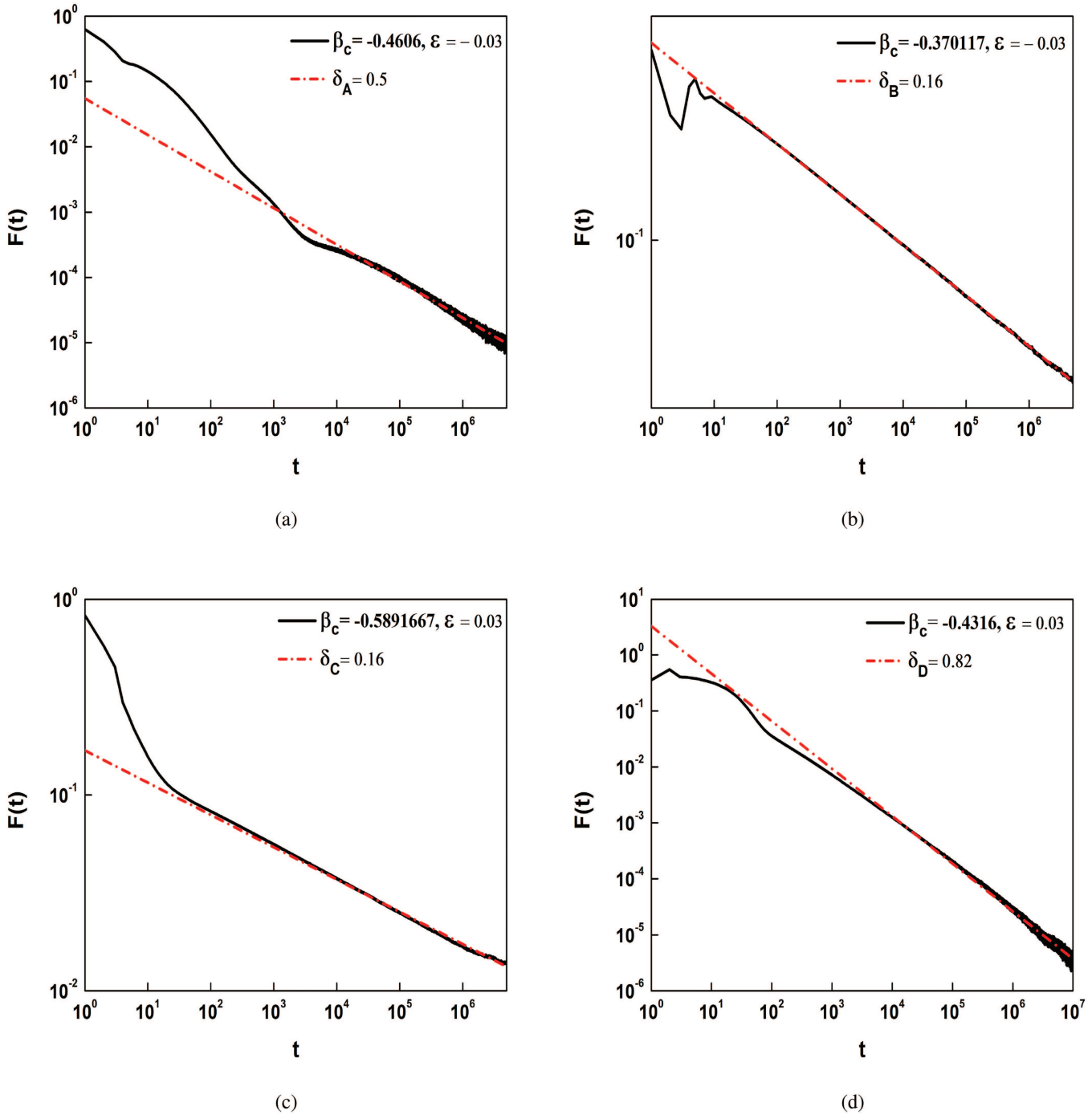

FIG. 7. We plot the order parameter $F(t)$ as a function of time t at different critical points. We simulate for $N = 2 \times 10^5$ and average for 100 configurations. We take the number of time steps $t = 5 \times 10^6$ for (a), (b), and (c), while we take $t = 10^7$ in the case of (d). (a) For the critical point A ($\beta_c = -0.4606$ and $\varepsilon = -0.03$), we observe a power law decay with exponent $\delta_A = 0.5$. (b) For the critical point B ($\beta_c = -0.370\,117$ and $\varepsilon = -0.03$), we get a power law decay with exponent $\delta_B = 0.16$. (c) We see a power law decay with the same exponent $\delta_C = 0.16$ for the critical point C ($\beta_c = -0.589\,166\,7$ and $\varepsilon = 0.03$). (d) We obtain a power law decay with exponent $\delta_D = 0.82$ for the critical point D ($\beta_c = -0.4316$ and $\varepsilon = 0.03$).

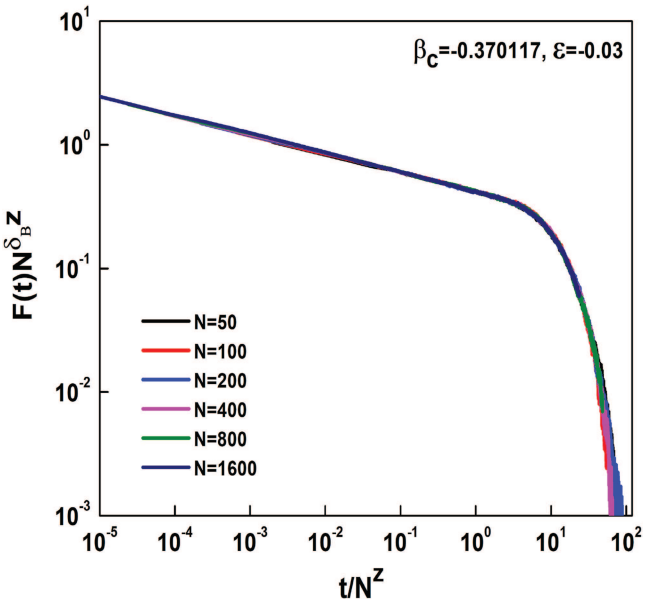

FIG. 8. We plot $F(t)N^{z\delta_B}$ as a function of t/N^z where $z = 1.59$ and $\delta_B = 0.16$ at the critical point B. We carry out simulations for $N = 50$, 100, 200, 400, 800, and 1600 sites. We average for 1600 configurations. Time steps range from 5×10^3 to 3×10^6 for different sizes considered.

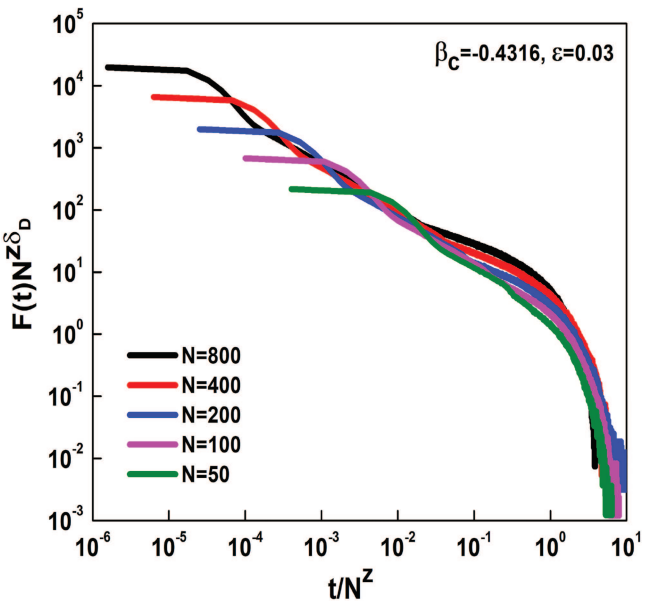

FIG. 9. We plot $F(t)N^{z\delta_D}$ as a function of t/N^z where z=2 and $\delta_D = 0.82$ at point D ($\beta_c = -0.4316$, $\varepsilon = 0.03$). Simulation is done for $N = 50$, 100, 200, 400, and 800 sites. We average over 2000, 10 000, 500, 350, and 325 configurations, respectively. Time steps range from 5×10^3 to 3×10^6 for different sizes.

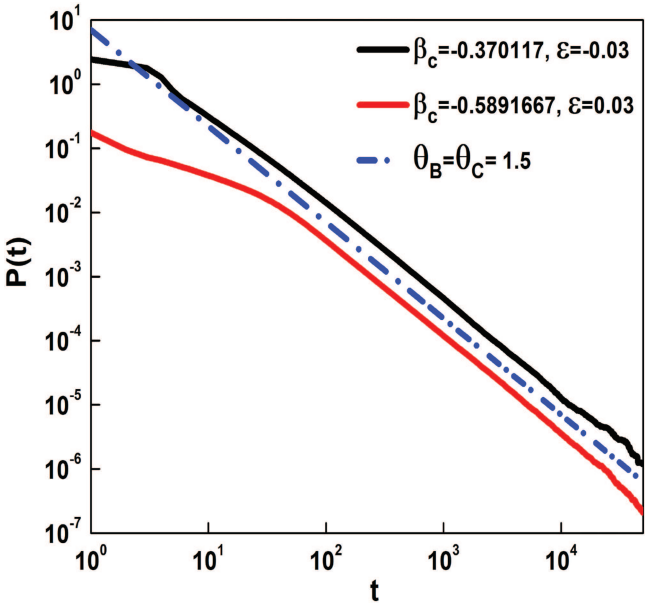

FIG. 10. We plot persistence $P(t)$ as a function of time t at the critical points: $\beta_c = -0.370\,117$ having $\varepsilon = -0.03$ and $\beta_c = -0.589\,166\,7$ with $\varepsilon = 0.03$. We take 2×10^5 sites and average over 500 configurations for 10^5 time steps. We observe a power law decay with exponent $\theta_B = \theta_C = 1.5$. The curves are multiplied by arbitrary constants for better visibility.

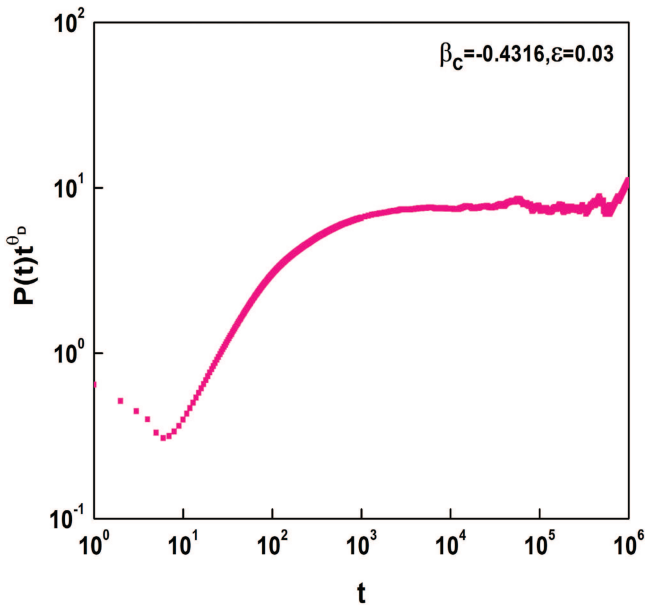

FIG. 11. We plot $P(t)t^{\theta_D}$ as a function of t where $\theta_D = 1.1$. We simulate for 10^6 sites and average over 25 configurations and $N = 2 \times 10^5$. The curve reaches a constant asymptotically.

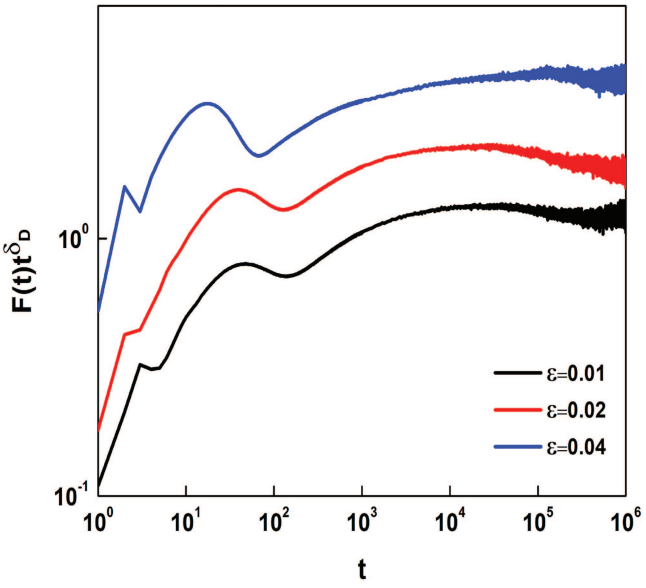

FIG. 12. We plot the order parameter $F(t)t^{\delta}$ as a function of time t at the critical points for which synchronized period-3 state is observed for different values of ε. We choose $\delta = 0.81$ for $\varepsilon = 0.01$ and $\varepsilon = 0.02$. We choose $\delta = 0.80$ for $\varepsilon = 0.04$. We average over 25 configurations. This quantity reaches a constant asymptotically. This exponent is close to 0.82 observed at point D for $\varepsilon = 0.03$. The curves are multiplied by arbitrary constants for better visibility.

band (or value) after every three-time step, and it is nonzero if at least some of the sites do not show this behavior. This order parameter shows clear power-law behavior at the critical points. This helps us to decide the corresponding universality class. We also carry out finite-size scaling to find the dynamic exponent z. Even persistence shows clear power-law behavior at three critical points and a well-defined persistence exponent is observed at these points. We observe three different possibilities: (a) Different sites get stuck in different bands forever leading to a spatially inhomogeneous state, which is frozen in time in a coarse-grained sense. This transition is in the directed percolation universality class. The exponents δ, z and even persistence exponent θ match with the expected values for the DP class. (b) All sites converge to the same band. This shows an Ising-type exponent at the critical point. (c) All sites get synchronized and are in period 3. This transition has not been observed before. It is an interesting transition because it is very easy to create defects in a 1D lattice. Hence, a synchronized periodic state is not expected. The exponent δ is 0.82. We also find a well-defined persistence exponent at this point. These exponents obtained using the same order parameters are different and point to a new universality class.

For very tiny coupling, it is conceivable to see a synchronized periodic state with period $T + 1$. If the universality class changes with T in this instance, this is interesting to note. Another curiosity could be whether one can observe comparable dynamics with stochastic cellular automata models. In such a model, every site can have clock-type dynamics along with some nearest-neighbor interaction. At every time, the site is updated, and if it is in state k, it goes to a $k + 1$ state. The state $T + 1$ is equivalent to state 0. Such models are introduced in the context of epidemic spread.[43] In this model, there is interaction with neighbors only if the agent is in state 0 and there is a need to suitably modify it so that periodic states exist. It would be interesting to see if the universality class depends on T in such a case.

ACKNOWLEDGMENTS

P.M.G. thanks DST-SERB for financial assistance (Ref. No. CRG/2020/003993).

AUTHOR DECLARATIONS

Conflict of Interest

The authors have no conflicts to disclose.

Author Contributions

Pratik M. Gaiki: Data curation (equal); Formal analysis (equal); Software (equal); Visualization (equal); Writing – original draft (equal); Writing – review & editing (equal). **Ankosh D. Deshmukh:** Investigation (equal); Software (equal); Validation (equal); Visualization (equal). **Sumit S. Pakhare:** Methodology (equal); Software (equal); Visualization (equal). **Prashant M. Gade:** Conceptualization (lead); Formal analysis (equal); Funding acquisition (equal); Methodology (equal); Project administration (lead); Resources (equal); Supervision (lead); Validation (equal); Writing – original draft (lead); Writing – review & editing (lead).

DATA AVAILABILITY

The data that support the findings of this study are available from the corresponding author upon reasonable request.

REFERENCES

[1] M. Henkel, H. Hinrichsen, S. Lübeck, and M. Pleimling, *Non-Equilibrium Phase Transitions* (Springer, 2008), Vol. 1.
[2] E. V. Albano and M. A. Munoz, "Numerical study of persistence in models with absorbing states," Phys. Rev. E **63**(3), 031104 (2001).
[3] H. Hinrichsen and H. M. Koduvely, "Numerical study of local and global persistence in directed percolation," Eur. Phys. J. B **5**(2), 257–264 (1998).
[4] H.-K. Janssen, "On the nonequilibrium phase transition in reaction-diffusion systems with an absorbing stationary state," Z. Phys. B **42**(2), 151–154 (1981).
[5] P. Grassberger, F. Krause, and T. von der Twer, "A new type of kinetic critical phenomenon," J. Phys. A: Math. Gen. **17**(3), L105 (1984).
[6] H. Janssen, K. Oerding, F. Van Wijland, and H. Hilhorst, "Lévy-flight spreading of epidemic processes leading to percolating clusters," Eur. Phys. J. B **7**(1), 137–145 (1999).
[7] P. D. Bhoyar, M. C. Warambhe, S. Belkhude, and P. M. Gade, "Robustness of directed percolation under relaxation of prerequisites: Role of quenched disorder and memory," Eur. Phys. J. B **95**(4), 64 (2022).
[8] S. S. Pakhare and P. M. Gade, "Novel transition to fully absorbing state without long-range spatial order in directed percolation class," Commun. Nonlinear Sci. Numer. Simul. **85**, 105247 (2020).
[9] I. Jensen, "Critical behavior of the pair contact process," Phys. Rev. Lett. **70**(10), 1465 (1993).
[10] P. M. Gade and C.-K. Hu, "Scaling and universality in transition to synchronous chaos with local-global interactions," Phys. Rev. E **73**(3), 036212 (2006).
[11] N. Menyhárd, "One-dimensional non-equilibrium kinetic Ising models with branching annihilating random walk," J. Phys. A: Math. Gen. **27**(18), 6139 (1994).

[12]N. Menyhárd and G. Ódor, "Non-equilibrium phase transitions in one-dimensional kinetic Ising models," J. Phys. A: Math. Gen. **28**(16), 4505 (1995).
[13]P. Grassberger, "Some further results on a kinetic critical phenomenon," J. Phys. A: Math. Gen. **22**(23), L1103 (1989).
[14]H. Takayasu and A. Y. Tretyakov, "Extinction, survival, and dynamical phase transition of branching annihilating random walk," Phys. Rev. Lett. **68**(20), 3060 (1992).
[15]A. Sudbury, "The branching annihilating process: An interacting particle system," Ann. Probab. **18**, 581–601 (1990).
[16]I. Jensen, "Conservation laws and universality in branching annihilating random walks," J. Phys. A: Math. Gen. **26**(16), 3921 (1993).
[17]M. H. Kim and H. Park, "Critical behavior of an interacting monomer-dimer model," Phys. Rev. Lett. **73**(19), 2579 (1994).
[18]H. Hinrichsen, "Pair contact process with diffusion: A new type of nonequilibrium critical behavior?," Phys. Rev. E **63**(3), 036102 (2001).
[19]J. D. Noh and H. Park, "Universality class of absorbing transitions with continuously varying critical exponents," Phys. Rev. E **69**(1), 016122 (2004).
[20]M. B. Matte and P. M. Gade, "Persistence as the order parameter in a generalized pair-contact process with diffusion," J. Stat. Mech.: Theory Exp. **2016**(11), 113203.
[21]B. P. Rajvaidya, A. D. Deshmukh, M. Gade, and G. G. Sahasrabudhe, "Transition to coarse-grained order in coupled logistic maps: Effect of delay and asymmetry," Chaos, Solitons Fractals **139**, 110301 (2020).
[22]Z. Jabeen and N. Gupte, "Spatiotemporal intermittency and scaling laws in the coupled sine circle map lattice," Phys. Rev. E **74**(1), 016210 (2006).
[23]G. I. Menon, S. Sinha, and P. Ray, "Persistence at the onset of spatio-temporal intermittency in coupled map lattices," Europhys. Lett. **61**(1), 27 (2003).
[24]H. Chaté and P. Manneville, "Spatio-temporal intermittency in coupled map lattices," Phys. D **32**(3), 409–422 (1988).
[25]A. V. Mahajan, M. A. Saif, and P. Gade, "Dynamic transitions in Domany-Kinzel cellular automata on small-world network," Eur. Phys. J. Spec. Top. **222**(3), 895–903 (2013).
[26]E. Salazar-Neumann, M. C. Vargas, and G. Pérez, "Critical behavior of a dynamic analog to the $q = 3$ potts model," Phys. Rev. E **71**(3), 036228 (2005).
[27]P. M. Gade and G. Sahasrabudhe, "Universal persistence exponent in transition to antiferromagnetic order in coupled logistic maps," Phys. Rev. E **87**(5), 052905 (2013).
[28]J. Miller and D. A. Huse, "Macroscopic equilibrium from microscopic irreversibility in a chaotic coupled-map lattice," Phys. Rev. E **48**(4), 2528 (1993).
[29]J. Rolf, T. Bohr, and M. H. Jensen, "Directed percolation universality in asynchronous evolution of spatiotemporal intermittency," Phys. Rev. E **57**(3), R2503 (1998).
[30]P. Marcq, H. Chaté, and P. Manneville, "Universality in ising-like phase transitions of lattices of coupled chaotic maps," Phys. Rev. E **55**(3), 2606 (1997).
[31]A. D. Deshmukh, N. D. Shambharkar, and P. M. Gade, "Effect of a mode of update on universality class for coupled logistic maps: Directed Ising to Ising class," Int. J. Bifurc. Chaos **31**(03), 2150042 (2021).
[32]M. G. Rosenblum, A. S. Pikovsky, and J. Kurths, "Phase synchronization of chaotic oscillators," Phys. Rev. Lett. **76**(11), 1804 (1996).
[33]S. Yang and C. Duan, "Generalized synchronization in chaotic systems," Chaos, Solitons Fractals **9**(10), 1703–1707 (1998).
[34]L. M. Pecora, T. L. Carroll, G. A. Johnson, D. J. Mar, and J. F. Heagy, "Fundamentals of synchronization in chaotic systems, concepts, and applications," Chaos **7**(4), 520–543 (1997).
[35]P. M. Gade, "Synchronization of oscillators with random nonlocal connectivity," Phys. Rev. E **54**(1), 64 (1996).
[36]T. Shinbrot, "Synchronization of coupled maps and stable windows," Phys. Rev. E **50**(4), 3230 (1994).
[37]T. Bohr, G. Grinstein, Y. He, and C. Jayaprakash, "Coherence, chaos, and broken symmetry in classical, many-body dynamical systems," Phys. Rev. Lett. **58**(21), 2155 (1987).
[38]D. R. da Costa, J. G. Rocha, L. S. de Paiva, and R. O. Medrano-T, "Logistic-like and gauss coupled maps: The born of period-adding cascades," Chaos, Solitons Fractals **144**, 110688 (2021).
[39]S. N. Majumdar, "Persistence in nonequilibrium systems," Curr. Sci. **77**, 370–375 (1999).
[40]A. J. Bray, S. N. Majumdar, and G. Schehr, "Persistence and first-passage properties in nonequilibrium systems," Adv. Phys. **62**(3), 225–361 (2013).
[41]B. Derrida, V. Hakim, and V. Pasquier, "Exact first-passage exponents of 1D domain growth: Relation to a reaction-diffusion model," Phys. Rev. Lett. **75**(4), 751 (1995).
[42]G. I. Menon, S. Sinha, and P. Ray, "Persistence at the onset of spatio-temporal intermittency in coupled map lattices," Europhys. Lett. **61**(1), 27 (2003).
[43]P. M. Gade and S. Sinha, "Dynamic transitions in small world networks: Approach to equilibrium limit," Phys. Rev. E **72**(5), 052903 (2005).

Peer Reviewed and Refereed Journal 2023 **(ISSN : 09726330)**

Rashtrasant Tukadoji Maharaj Nagpur University
SCIENCE JOURNAL 2023
Vol.: XVI

Study of Persistence in Kinetic Ising Model of Glass Transition by Fredricson and Andersen

Pratik M. Gaiki1*, Prashant M. Gade2

1Department of Physics, Shri Shivaji Education Society Amravati's, Shri Shivaji Arts, Commerce & Science College, Motala, Dist. Buldhana-443103
2Department of Physics, RTM Nagpur University, Nagpur-440033.

Corresponding author email:
pmgaiki@gmail.com

ABSTRACT

We study the persistence in the microscopic theory of glass transition based on the kinetic Ising model with cooperative spin flip rates. We consider spin models that are standard Ising ferromagnetic ones (and not the ones used for modelling spin glasses). However, they have spin flip rules which have very cooperative spin flip rates. We perform a graphical analysis to study the persistence of spins. We also observe the glass transition. Local persistence shows stretched exponential behavior in time in the glassy phase.

Keywords : Persistence; Ising Model; Glass Transition.

Introduction

The relaxation period for structural rearrangements sharply increases when liquids are cooled down enough. If significant cooling rates prevent crystallization, the majority of supercool liquids transition into a metastable glassy state. Glass transition is experimentally characterized using relaxation periods of a few minutes or hours, which correspond to viscosities of roughly 10^{23} poise. The freezing in of the translational degrees of freedom causes a steady decrease in several thermodynamic parameters at this transition temperature T_g, including compressibility, specific heat, and thermal expansion. This is the so-called glass transformation range, where the length of the tests determines different observed quantities [1].

The study of the following problem—which of the stated stages of aggregation can glasses be assigned to—was one of the first topics explored with the start of a scientific investigation into glasses. On the one hand, experimental data showed that glasses had a defined form, a nearly limitless viscosity, and mechanical properties of solids. Nonetheless, glasses also exhibit classic liquid characteristics, such as their isotropy and amorphous structure, which refer to the lack of long-range topological and orientational organisation.

Gases are far smaller in free volume and have a much lower density than liquids. As such, it is not possible to translate the liquid's building blocks independently. In liquids and melts, molecular motion takes on a cooperative nature, and the interactions between the particles greatly influence the system's characteristics [2].

One of the most significant thermophysical characteristics of amorphous polymers is

the glass transition temperature (T_g). This temperature is sometimes referred to as the "melting point of amorphous materials," and although this term may not sound scientific, it accurately describes the glass transition: polymeric materials are soft and rubbery in the highly viscous region above the T_g, whereas they are hard and brittle below it. However, there is a crucial distinction between glass transition and melting: melting represents a true first-order phase transition, whereas glassification (vitrification) is only a pseudo-second-order transition. In other words, while melting produces a discontinuity in the first derivative of the Gibbs free energy (volume, entropy), glassification only causes a (pseudo) discontinuity in the second derivative (e.g. heat capacity, expansion coefficient, etc.).

The glass transition is a complex process that is controlled by a number of parameters, including heating rate, ageing history, morphology, and molecular weight. In truth, the actual nature of the glass transition is not widely understood. Over time, a number of theories have been proposed to explain the glass transition. Kinetic and equilibrium theories can be used to categorise the theories. The glass transition is viewed as a dynamic process in the kinetic theories. The process of "freezing" the motions of chain segments (kinetic units) results in vitrification or glassification. The initial (solid-state) transition starts at extremely low temperatures, at which point side chain motions and localised bond bending and stretching can happen. This is referred to as the T_γ gamma transition. The material begins to acquire some toughness as the temperature rises and other localised motions involving whole side chain and localised group movements become active. The beta transition (T_β) is the name given to this change. T_g is reached while the heating continues. Large-scale coordinated motions of the polymer chains take place in this area, and a noticeable shift in characteristics is seen [3].

Leutheusser created a microscopic model of the hard-sphere fluid's glass transition. He developed a straightforward non-linear solution for the time evolution of the density correlation function that forecasts a glass transition by roughly analysing mode coupling equations. A highly cooperative spin-flip rate kinetic ising model is the foundation of the glass transition microscopic theory. Through graphical analysis, one can derive conclusions for the spin systems that closely resemble Leutheusser's findings for hard spheres. This observation might represent the addition of a universality aspect for the glass transition [4].

2. The Ising Model:

The physics of phase transitions, which happen when a slight change in a parameter like temperature or pressure results in a large-scale, qualitative change in a system's state, is the focus of the Ising model. Phase transitions are a widespread occurrence in everyday life and physics. "Spontaneous magnetization" is a characteristic of ferromagnetism.

The Ising model is intended to describe how short-range interactions, for example, between molecules in a crystal, result in long-range, correlative behaviour and, in a way, to forecast the possibility of a phase transition. The Ising model has also been used to solve issues in molecular biology, chemistry, and other fields that study the "cooperative" behaviour of complex systems.

Assigning an independent variable σ_i to every lattice site i = 1,..., N is the first thing we do. There are only two potential values for the σ_i variables; σ_i = +1 or -1, which we will refer to as the lattice site's two conceivable states. As we will explain below, this reflects the physical premise that there are only two possible outcomes at each lattice site: up or down or occupied or vacant. A system configuration is the assignment of values (σ_1, σ_2,..., σ_N) to every lattice site. A sum across all conceivable configurations will be a crucial component of the Ising model. If N is even somewhat large, this sum obviously has a huge number of terms because there are 2^N configurations. One such configuration for 2-dimensional lattice is shown in Fig. 1. One should never even consider performing a numerical computation for a macroscopic crystal with N!

After that, we create the system's Hamiltonian. The total energy of a system is known as the Hamiltonian in mathematical physics, and it controls motion. The ideal and seemingly extremely severe assumption that only short-range, "nearest-neighbor" interactions and interactions between the lattice sites and an "external field" contribute to the system's energy level is the basis for the definition of the Hamiltonian for the Ising model. For each configuration $\sigma = (\sigma_1, \sigma_2,..., \sigma_N)$we have,

$$\mathbf{H = H(\sigma) = -\sum_{<i,j>} E\left(\sigma_i \cdot \sigma_j\right) - \sum_i J\,\sigma_i}$$

where the first sum is over all pairs of the lattice's nearest neighbours and the second sum is over all lattice sites. E and J are the parameters in this equation. For nearest-neighbor interactions and interactions with the external field, respectively, the parameters E and J stand for the "energies" involved. A ferromagnet has an energy level that is lower than a non-magnetized configuration because a "magnetised" configuration (where the majority of nearest-neighbor pairings have parallel moments,$\sigma_i = \sigma_j$) has a positive E. When an "external magnetic field" (represented by the parameter J) is present, the magnetic moments will seek to align with the field's direction, once more "favouring" configurations with shorter energy levels [5].

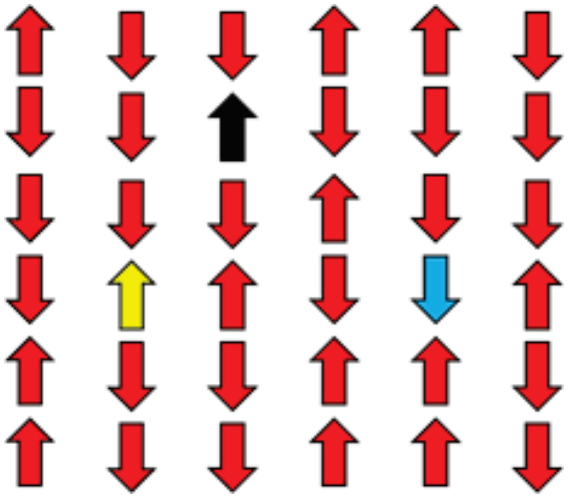

Fig. 1: The Ising model applied to a two-dimensional square lattice. Every arrow is a "spin," a magnetic moment that might point upward or downward.

3. The Model:

A master equation that satisfies the concept of detailed balance and permits only one spin to change state in a differential time increment dt (i.e., a single flip model) is used to characterise the dynamics of the spin system. Potential cooperative relaxation models include a family of facilitated kinetic ising models.

Here, an extremely cooperative spin-flip rate kinetic Ising model-based microscopic theory of the glass transition is presented. An n-spin facilitated model is defined as one for which the flip rate of the j^{th} spin is nonzero only if *n* or more near neighbors of spin *j* are in the spin-up state in spin configuration [4]. In this case, we study a variant of the Fredrickson-Andersen model in which we use the following update rule.

a) Choose a site randomly on the lattice.

b) If none of the neighbors is 'up' spin, the spin at this site is not changed.

c) If the site has at least one 'up' neighbor, and the site itself has an 'up' spin, it is flipped. If the site has at least one 'up' neighbor and the site itself has a 'down' spin, it is flipped with probability p.

We have run simulations for this model with different values of p. The state that all spins "down" is the absorbing state for any value of p. Spins for p=0 will occasionally be "down." This isn't guaranteed for higher values of p.

We have looked into this system's short-time dynamics and memory retention. It is common to observe extended exponential dynamics in glassy systems. For lesser values of p, the dynamics should be exceedingly sluggish. This will show up as autocorrelation with starting conditions. We have examined the likelihood that the initial conditions will be

precisely maintained, or persistence, a stronger quantifier. This quantifier has recently been the subject of multiple investigations.

In our study, we simulate the system on 50,000 sites for 1,00,000-time steps and averaged over 25,000 configurations. The figures we plot are those of logarithm of persistence versus time. The graphs are plotted for different values of probability **p** and the exponent **β**. We take the value of p=0.1 onwards in steps of 0.1 and the corresponding value of β. We note that the value of β increases with p every time but never becomes 1. The nature of the graph is depicted by a stretched exponential function.

4. Persistence:

A concept presented in the field of statistical physics is persistence, which is a generalization of first passage time. The fraction of spins in a spin system that has not altered their original spin state at all until a specific period is known as (local) persistence in spin systems. Non-zero persistence therefore suggests that the system preserves the initial conditions indefinitely. Nonzero persistence indicates that the system keeps track of its starting conditions indefinitely, as can be seen from the definition. The decay exponent is referred to as the persistence exponent when the persistence exhibits power-law decay at the critical point. A novel class of exponents, distinct from the typical critical exponents, is discovered - persistence exponents. This is a non-Markovian quantity and we need to know time correlations of arbitrary order to compute persistence. The exponents are found to be nontrivial even in the simplest of cases [6].

We set a parameter *b* to be the degree of asymmetry of the kinetic constraints. The limiting value of b for the Fredrickson-Andersen (FA) model is b=1/2 [4]. The value of b=0 or 1 corresponds to the asymmetrically constrained ising chain (ACIC) model [7]. The stretched exponential is thus obtained as $P(t)e(-t/\tau\_ACIC)^{\beta}$ where $\beta= (1+1/T \ln 2)^{-1}$. Here t is the time, T stands for temperature and τ corresponds to the equilibrium relaxation time. For short times the persistence is dominated by the fastest exponential decay. It is possible to approximate the long-term behavior by substituting an integral evaluated in the saddle point approximation for the sum of the values [8]. Menon, Sinha, and Ray have extended this definition to CML. They suggested that the initial variable value of a site should be represented by + spin if it is more than the fixed point and − spin if it is less than the fixed point. It is now possible to specify the persistence in a way that is similar to spin systems. They defined this in the context of coupled circle maps transitioning to an absorbing fixed-point state. [6].

5. Results:

We work on 1d array of size 50,000 simulated for 1,00,000 time steps on 25,000 configurations. We plot the graphs of the logarithm of persistence versus time considering the values of p and β. In Figs. 2-10, we show persistence P(t) as a function of t^{β} on semilogarithmic scale for p=0.1 to 0.9. The straight line indicates that the behavior is well described by the stretched exponential function. Following are the plots of 'persistence vs time'. (Abbreviations: Probability-p, exponent- β)

p	0.1	0.2	0.3	0.4	0.5	0.6	0.7	0.8	0.9
β	0.4 (Fig.2)	0.5 (Fig.3)	0.57 (Fig.4)	0.59 (Fig.5)	0.615 (Fig.6)	0.625 (Fig.7)	0.650 (Fig.8)	0.715 (Fig.9)	0.760 (Fig.10)

Table 1: Probabilities (p), the respective exponents (β) and figure numbers of the graphs .

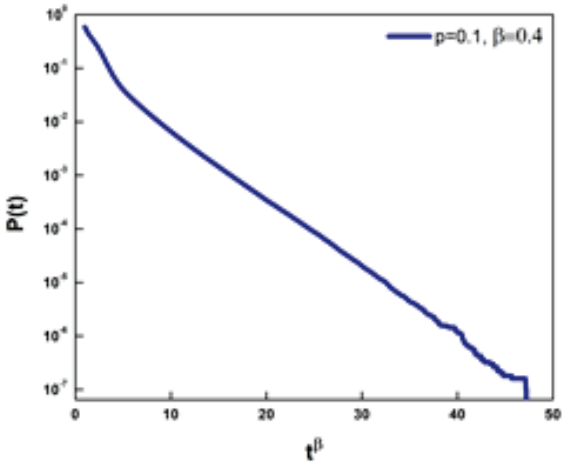

Fig. 2: p=0.1, β= 0.4

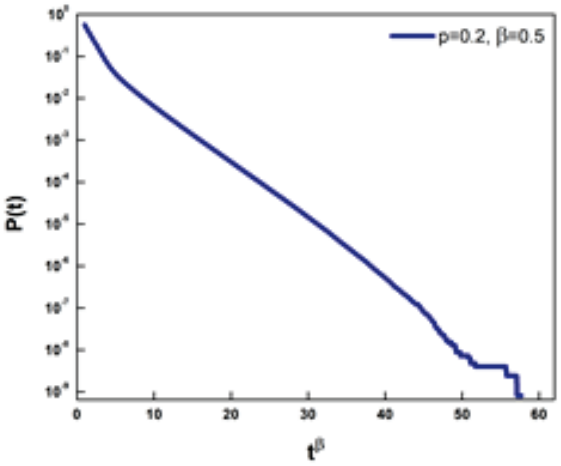

Fig. 3: p=0.2, β= 0.5

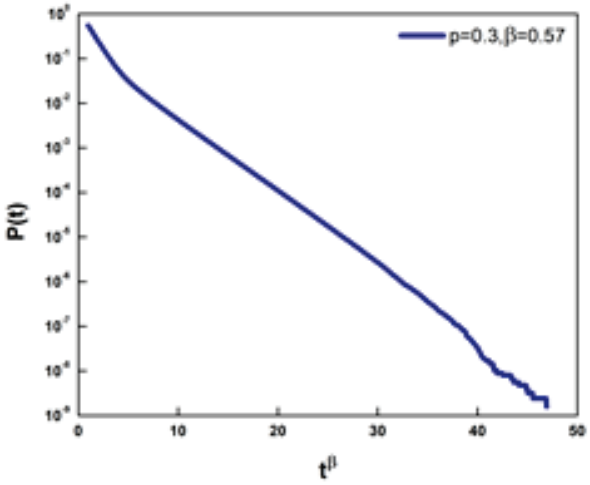

Fig. 4: p=0.3, β=0.57

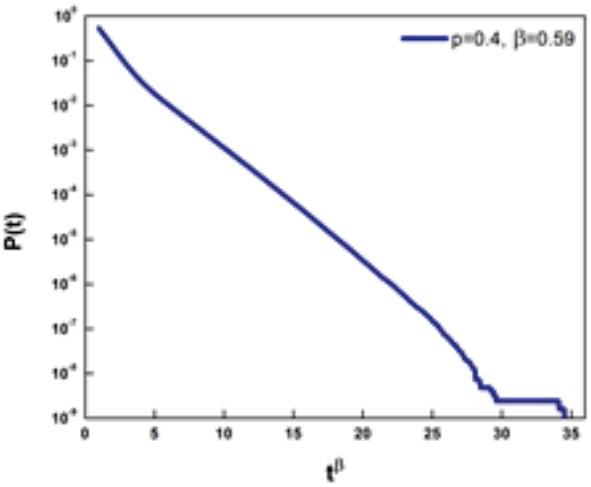

Fig. 5: p=0.4, β=0.59

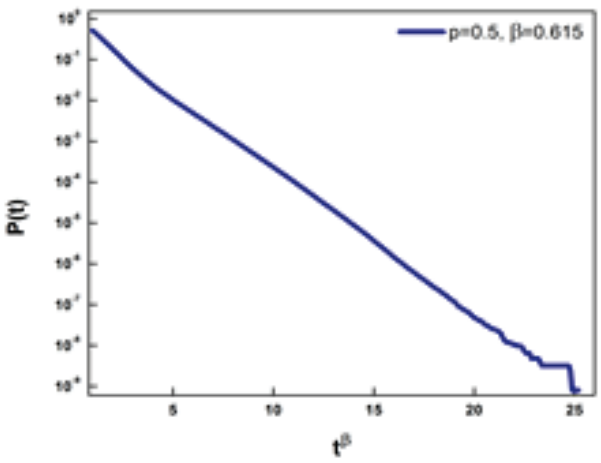

Fig. 6: p=0.5, β=0.615

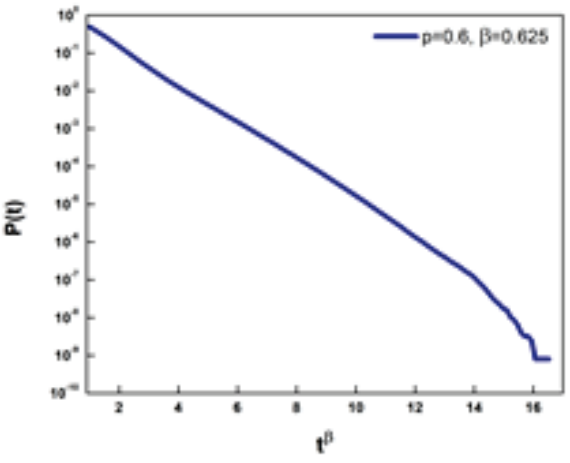

Fig. 7: p=0.6, β=0.625

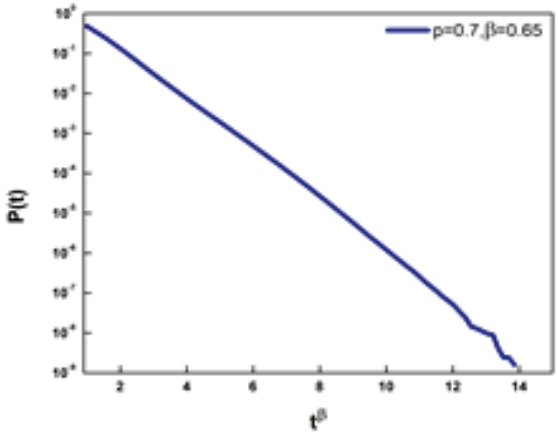

Fig. 8: p=0.7,β=0.65

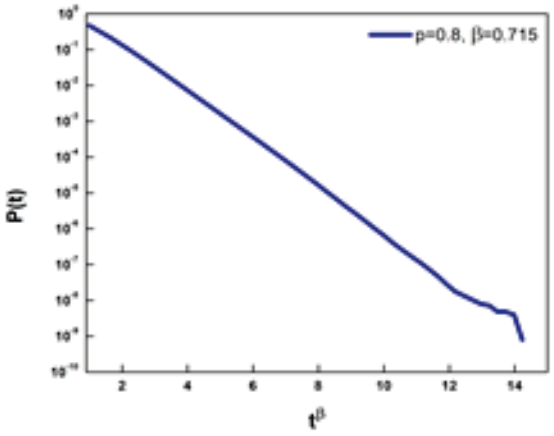

Fig. 9: p=0.8, β=0.715

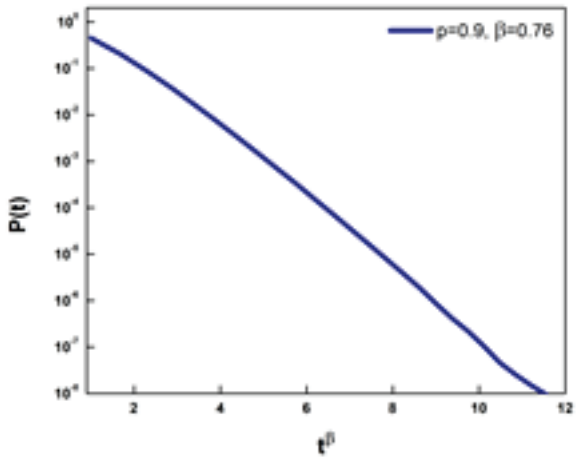

Fig. 10: p=0.9, β=0.76

6. Discussion:

Fredrickson and Andersen introduced the kinetic ising model of glass transition [4]. In our work, we make a study of the existence of persistence in this model and observe the characteristics. Our function consists of a Hamiltonian that comprises the sum over all pairs of the lattice's nearest neighbours along with the sum over all lattice sites We get a stretched exponential function by inserting a fractional power law into the function. Studies in higher dimensions could be of interest. For every value of the probability (p), we get a corresponding exponent (β). In some cases, saturation can also be seen at the tail. The stretched exponent β lies between 0 and 1. It increases with probability. Thus, the persistence of the ising spins (how long the spins remain + (up)) shows stretched exponential behavior in glass transition.

7.References:

[1] Leutheusser, E. Phys. Rev. A (1984): 29(5); 2765.

[2] Schmelzer J.W.P., Gutzow I.S., WILEY-VCH Verlag GmbH & Co. KGaA, (2011).

[3] https://polymerdatabase.com/polymer%20physics/GlassTransition.html

[4] Fredrickson G.H., Andersen H.C. Phys. Rev. Lett. (1984): 53(13); 1244.

[5] Cipra B.A. The American Mathematical Monthly (1987): 94(10); 937.

[6] Gade P.M., Sahasrabudhe G.G, Phys. Rev. E (2013): 87; 052905.

[7] Buhot A, Garrahan JP, Phys. Rev. E. (2001):64(2);021505.

[8] Palmer RG, Stein DL, Abrahams E, Anderson PW, Phys. Rev. Lett. (1984):53(10);958.

Indian J Phys
https://doi.org/10.1007/s12648-024-03135-1

ORIGINAL PAPER

Existence of multistability in the dynamical behavior of q-deformed Lozi map

P M Gaiki[1], P D Bhoyar[2]*, D D Joshi[3] and P M Gade[3]

[1]Department of Physics, Shri Shivaji Education Society Amravati's, Shri Shivaji Arts, Commerce and Science College, Motala, Dist. Buldhana, Maharashtra 443103, India

[2]Department of Physics, Seth Kesarimal Porwal College of Arts and Science and Commerce, Kamptee, Nagpur, Maharashtra 444101, India

[3]Department of Physics, R.T.M. Nagpur University, Nagpur, Maharashtra 440033, India

Received: 05 August 2023 / Accepted: 12 February 2024

Abstract: Dynamics, bifurcations, strange attractors, and related nonlinear phenomena have been investigated in numerous one and two-dimensional maps. The maps could be smooth, non-differentiable, or even discontinuous. Various deformations of these systems could yield valuable insight into the dynamics of these maps. The quantum deformation or q-deformation of nonlinear maps has been investigated recently in this context. It leads to large excursions in the phase space, and the nature of attractors is very different from those usually observed. We investigate the q-deformed Lozi map. The q-deformation of either variable or both variables is studied from the viewpoint of bifurcations, possible multistability, and the nature of attractors. A rich structure of basins of coexisting attractors for various strengths of q-deformation is investigated. The initial conditions that lead to unbounded trajectories in the absence of q-deformation may get confined for slight q-deformation. Chaotic synchronization of two coupled q-deformed Lozi maps is observed, and an analytic criterion has been given for the same.

Keywords: Lozi map; q-Deformation; Discrete nonlinear maps; Strange attractor; Multistability; Coexisting orbits

1. Introduction

Discrete dynamical systems, popularly known as maps, have been an indispensable and important tool in the study of dynamical systems. Different dynamical systems demonstrate different physical phenomena. Dynamics in two dimensions is obviously richer than dynamics in one dimension. The Hénon map is probably the oldest and most studied two-dimensional map. It was introduced as a Poincare map for Lorenz system [1]. A more analytically tractable version of the same was proposed by Lozi, in a brief remark in 1978 [2]. It replaces the quadratic term in Hénon map with a piecewise linear term. It enables the rigorous demonstration of the chaotic nature of particular attractors [3] and a thorough examination of their basins of attraction [4]. Bifurcations in the Lozi map have been studied by Bottella-Soler and coworkers. They explored a particular bifurcation where there is a presence of continuum of neutrally stable cycles in one-dimensional maps, when the function becomes collinear with the identity map. [5]. Lozi map has been extremely popular and well investigated since its formulation. It continues to spark interest and investigations. Elhadj argued that "It seems that Lozi mapping bridges the gap between Axiom A systems and more complicated systems like the Hénon map called *quasi-attractors*". It is a hyperbolic system and is more tractable [6]. Notable difference with Hénon map is that it does not show a period-doubling sequence and a chaotic attractor is created via border collision. Piecewise linear maps have applications in several real-life systems, and the Lozi map is one of its earliest examples [7].

Chaotic maps have numerous applications, such as cryptography and secure communications using synchronization. Maps showing robust chaos, such as the Lozi map are very useful in this context [8]. Control and synchronization schemes have been demonstrated using the Lozi map. In game theory as well as in evolutionary algorithms, random switching between strategies or variation operators

Pratik M. Gaiki, Priyanka D. Bhoyar and Divya D. Joshi have contributed equally to this work.

*Corresponding author, E-mail: pribhoyar@gmail.com

Published online: 16 March 2024

has been replaced by chaotic switching. Such algorithms and their effects are investigated using the Lozi map. (A compilation of these applications can be found in a comprehensive book [6].) In a remarkable result, the piecewise linear nature of this map enabled mathematicians to establish the rigorous demonstration of the chaotic nature of attractors [3]. Several properties that limits the chaotic properties of the case of conservative map ($|b| = 1$) such as the domain of existence of the strange attractor, fixed points, invariant manifolds, and the basin of attraction are studied [9]. Of late, fractional variants and complex fractional variants of the Lozi map have been studied [10].

The Lozi map is piecewise linear. The mathematical nature of the functions has a profound influence on the dynamics they could display. Quadratic maps, cubic maps, maps on circles, and piecewise linear maps display different phenomena and bifurcations and could be useful in different contexts. The circle map shows Arnold tongues [11, 12]. The Gaussian map or other maps with long tails show period-adding cascades [13]. Piecewise linear maps show border collision bifurcations [14]. For the Lozi map, non-hyperbolicity plays an important role in determining the nature of possible bifurcations [15].

This work deals with the q-deformation of such a map. The underlying map is a rational function for such deformation and has singularities. The dynamics of maps with singularities have not been studied much. Therefore, we study q-deformation in two dimensions.

One more deformation of the Lozi map has been studied previously. Aharonov *et al* studied a variant of the Lozi map where $|x|$ is replaced by $\sqrt{x^2 + \epsilon}$. For very small deformation $\epsilon = 0.01$, they observe a chaotic region with several hexagonal islands [16]. The orbit of a single point has a chaotic trajectory where 13 hexagonal islands are excluded. Thus deformation can lead to several new phenomena. In this context, the q-deformation of maps could be of interest. In our case, the rational functions can have simple zeros in the denominator and dynamics can show a blow-up in the vicinity of these zeros. However, there can be a folding because a large value in the denominator leads to a small value. Hence, the overall system can stay bounded. It will become apparent in the subsequent discussion that q-deformation introduces such singularities. Sometimes its strength can be controlled as well. It can help us to carry out a systematic study of bifurcation structure in the presence of singularities.

We use the definition of q-deformation of numbers given by Jagannathan and Sinha [17]. Historically, the q-deformation has been studied in the context of quantum groups [18]. It is found to be useful in the study of quantum Yang-Baxter equations, quantum inverse scattering methods [19] and even statistical physics [20]. Any quantity (*i.e.* numbers, series, functions, etc.) could be studied by introducing an additional parameter q into the definition of the quantity such that under $q \to 1$, we recover the original quantity. The generalization of a mathematical quantity, operator, or function need not be unique [21]. For instance, there exist several definitions of fractional derivatives, and at least three independent definitions have been pursued actively. Similarly, q-deformation could be defined in several ways. For example, the q-exponential function has been defined in couple of ways [22]. The q-analogues of constants ϵ and π have been defined. Similarly, q-logarithms [23], q-Gaussian [24], q-factorials and q-binomial coefficients [25, 26] are defined. These functions are useful in combinatorics. Particularly, q-Gaussian is useful in statistical physics [20].

In this work, we study the q-deformation of numbers that leads to q-deformation of functions. Sinha and Jagannathan derived a q-deformation of integers based on a comparison between an exponential and its q-deformation [17]. They extended it to a real number. Furthermore, they used it to study nonlinear maps. The first study has been on the logistic map which is the most popular nonlinear map. There are numerous differences in the bifurcation diagram, including the absence of a complete period-doubling cascade. Logistic map shows multistability which is rare in one-dimensional maps. Multistability is the coexistence of several qualitatively different states. It can be reached asymptotically for a given set of parameters. Dynamics is not ergodic. The long-term dynamics of an attractor in a system depend upon the initial state. The study of the basin of the attractor can reveal the complex nature of underlying multistability. The phenomenon of multistability is encountered in nature as well as artificial systems such as optical systems [27] and semiconductor materials [28]. Several biological systems show functional flexibility in reacting to the external stimulus [29]. The coexisting species in an ecosystem possess several alternative dynamical states [30]. Gupta and Chandrmouli studied the q-deformation of the logistic map using deformation on the right as well as the left-hand side [31]. It does not display any qualitatively different behavior. It shows a period-doubling cascade independent of the deformation parameter. Later, Patidar and Sud studied Gaussian maps. This map has coexisting attractors even without the q-deformation (This is unique in one-dimensional maps). The q-deformed map exhibits coexisting attractors as well [32]. Canovas and Munoz-Guillermo studied the q-deformed Gaussian maps in further detail and investigated the topological entropy in these maps [33]. Using the sign of Schwazian derivative and the topological entropy, they carried out extensive studies in dynamics [34]. In 2-dimensional maps, Patidar, Purohit, and Sud studied q-deformed Hénon map. They demonstrated that chaos suppresses if the values of

q-deformation are chosen appropriately [35]. The q-deformation of the Tinkerbell map is studied by Iyengar and Balakrishnan. They observed several regions of chaos among the periodic windows [36]. They also studied its application to the encryption and decryption of messages.

2. The q-deformed Lozi map

In this work, we study the dynamical behavior of the Lozi map subjected to q-deformation. A Lozi map is a two-dimensional piecewise-linear map. The canonical form is as follows:

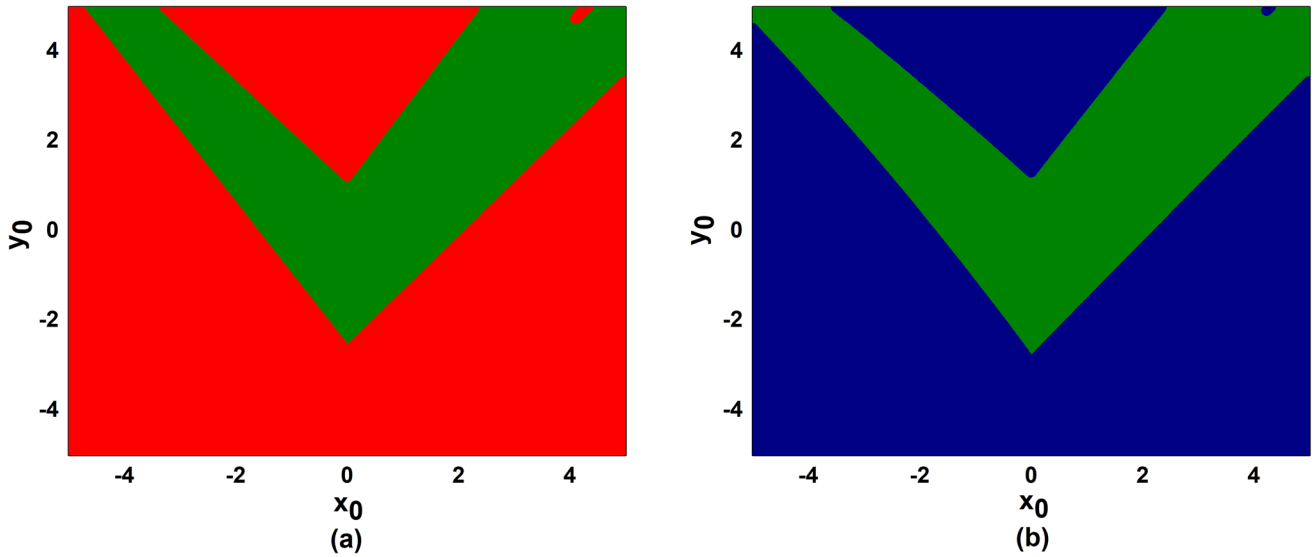

Fig. 1 (**a**) Shows the basin of an attractor for an non-deformed Lozi map. The initial conditions in the red part blow up to infinity. The rest of the initial conditions lead to a chaotic attractor. (**b**) Shows the basin of an attractor for a q-deformed Lozi map with deformation value $\epsilon_x = 0.01$ and $\epsilon_y = 0.01$. None of the initial conditions blow up to infinity for double deformation. The initial conditions in the blue region converge to a fixed point and those in the green region lead to a chaotic attractor. Several of the initial conditions that blew up in non-deformed cases are in the basin of the fixed point for double deformation

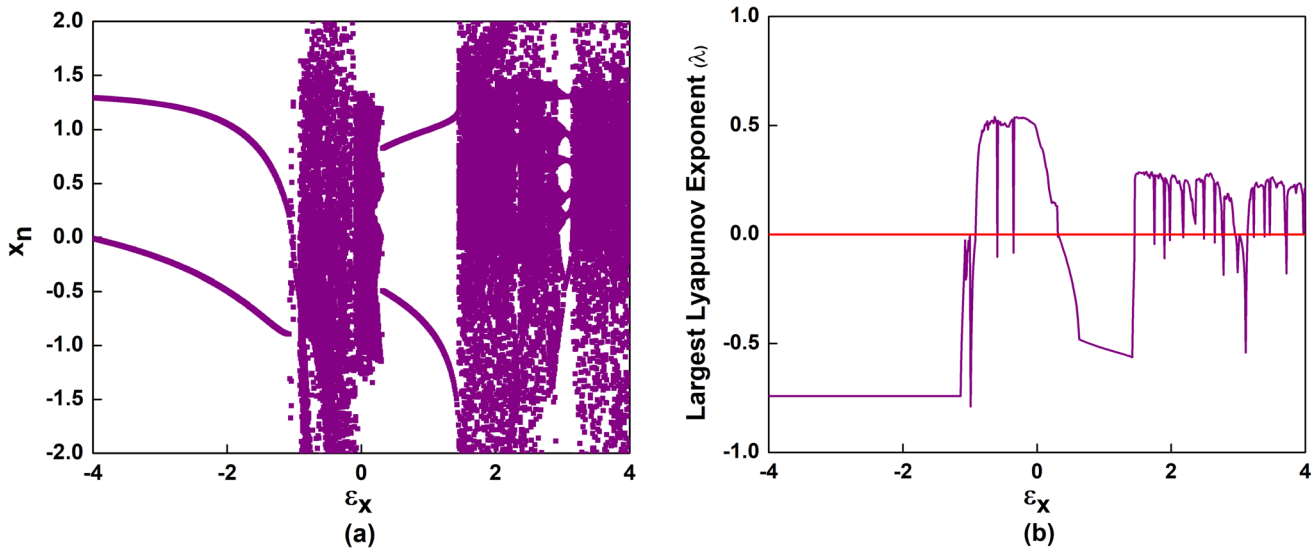

Fig. 2 (**a**) Shows the bifurcation diagram of the Lozi map with q-deformed x variable in the deformation range $-4 \leq \epsilon_x \leq 4$ and $\epsilon_y = 0$. We restrict the y-axis to a range and ignore large but rare values. (**b**) Shows the largest Lyapunov exponent λ as a function of ϵ_x for $a = 1.7$ and $b = 0.5$. Positive values of λ indicate the existence of chaos

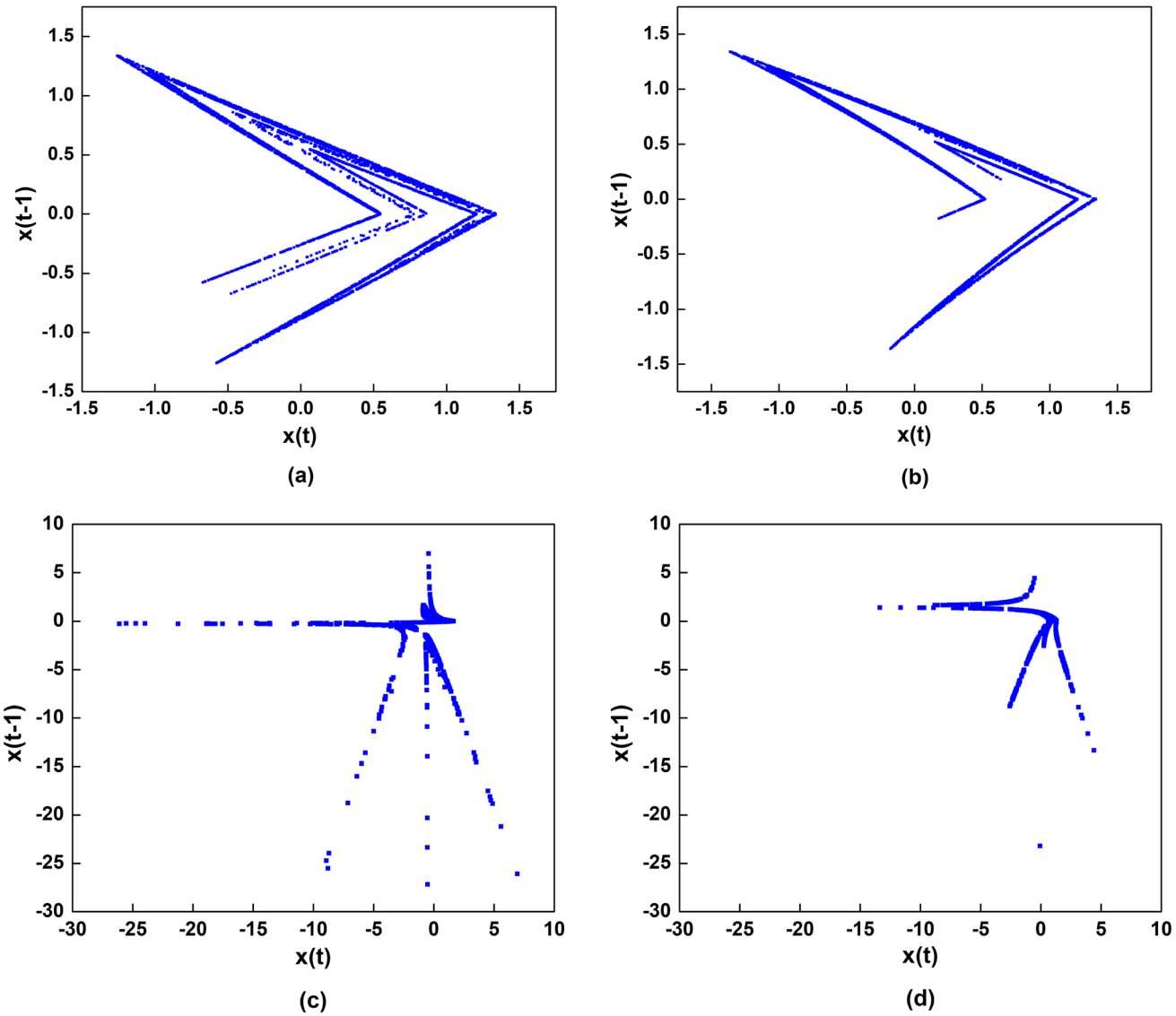

Fig. 3 (**a**), (**b**), (**c**) and (**d**) show the strange attractor of the x-deformed Lozi map obtained at $\epsilon_x = -0.02$, $\epsilon_x = 0.1$, $\epsilon_x = -0.8$ and $\epsilon_x = 2$, respectively. Here $a = 1.7$ and $b = 0.5$. Nature of chaotic attractor does not change much for small values of ϵ_x, whereas for comparatively larger values of ϵ_x such as -0.8 and 2, the nature of the attractor changes. In all figures, x and y values are restricted in the region. Large but rare values are not shown for better visibility

$$\begin{aligned} x_{(n+1)} &= f(x_n, y_n) = 1 - a|x_n| + y_n \\ y_{(n+1)} &= g(x_n, y_n) = bx_n \end{aligned} \tag{1}$$

where a and $b \neq 0$ are real constant. Generally used parameter values are $a = 1.4$ and $b = 0.3$. We note that the Lozi map displays a singular hyperbolic chaotic attractor at the typical control parameter value $a = 1.7$ and $b = 0.5$. We study the q-deformed map at $a = 1.4$ and $a = 1.7$ for various values of b.

The q-deformation of maps can be done in numerous ways. We use the q-deformation scheme proposed by Jaganathan and Sinha [17]. We study the cases where (a) only the x variable is q-deformed, (b) only the y variable is q-deformed, and (c) both the variables are q-deformed, essentially in the context of multistability. The doubly q-deformed Lozi map is as follows:

$$\begin{aligned} x_{(n+1)} &= f([x_n]_{q_x}, [y_n]_{q_y}) \\ y_{(n+1)} &= g([x_n]_{q_x}, [y_n]_{q_y}) \end{aligned} \tag{2}$$

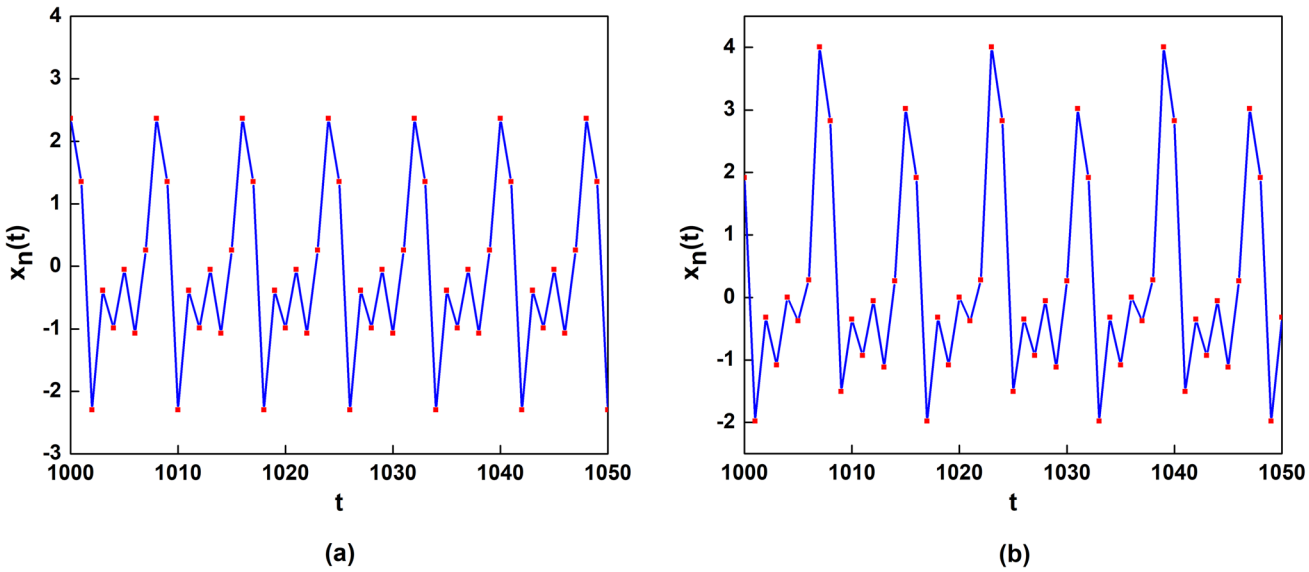

Fig. 4 (**a**) Shows the space-time plot for $\epsilon_x = 2.78$. The time series shows a period-8 orbit. (**b**) Shows a period-16 orbit obtained in the time series plot for $\epsilon_x = 2.998$

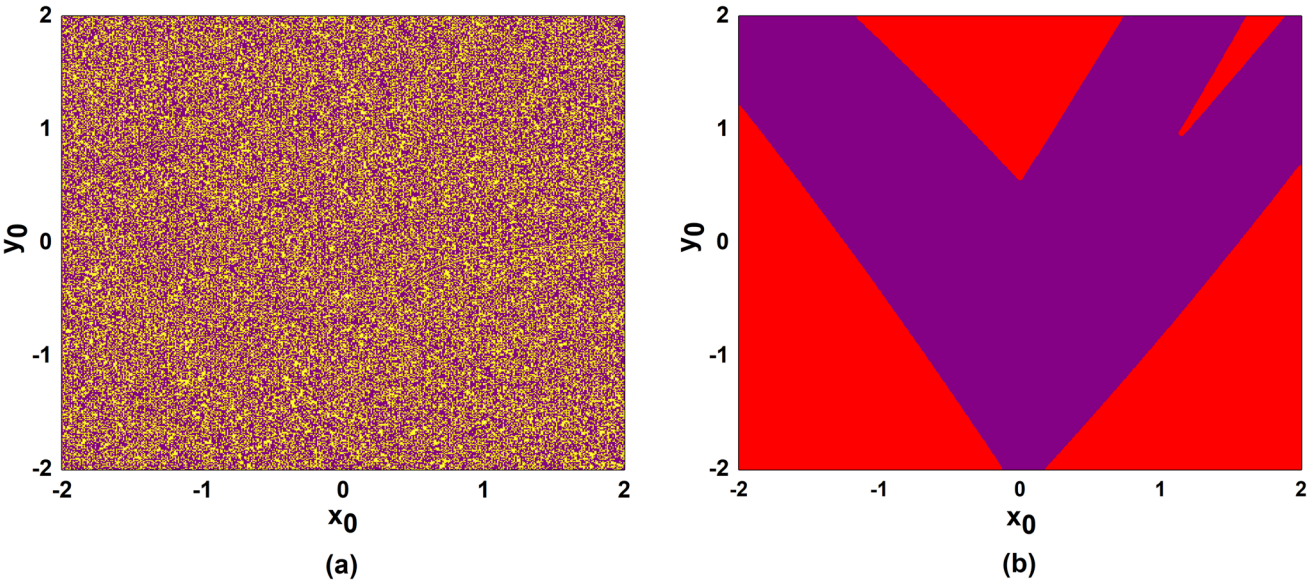

Fig. 5 Figure (**a**) shows the distribution of the initial conditions emerging into different dynamical conditions. We observe a period-2 orbit (*yellow*) and a chaotic (*purple*) attractor coexisting for $\epsilon_x = -0.912$ in the initial value plane. Figure (**b**) shows the initial condition emerging into fixed points (*red*) and chaos (*purple*) coexisting for $\epsilon_x = 0.05$

where,

$$[x]_{q_x} = \frac{x}{1 + (1 - q_x)(1 - x)} \tag{3}$$

$$[y]_{q_y} = \frac{y}{1 + (1 - q_y)(1 - y)} \tag{4}$$

Similarly, with the q-deformed x variable alone, the equations are as follows:

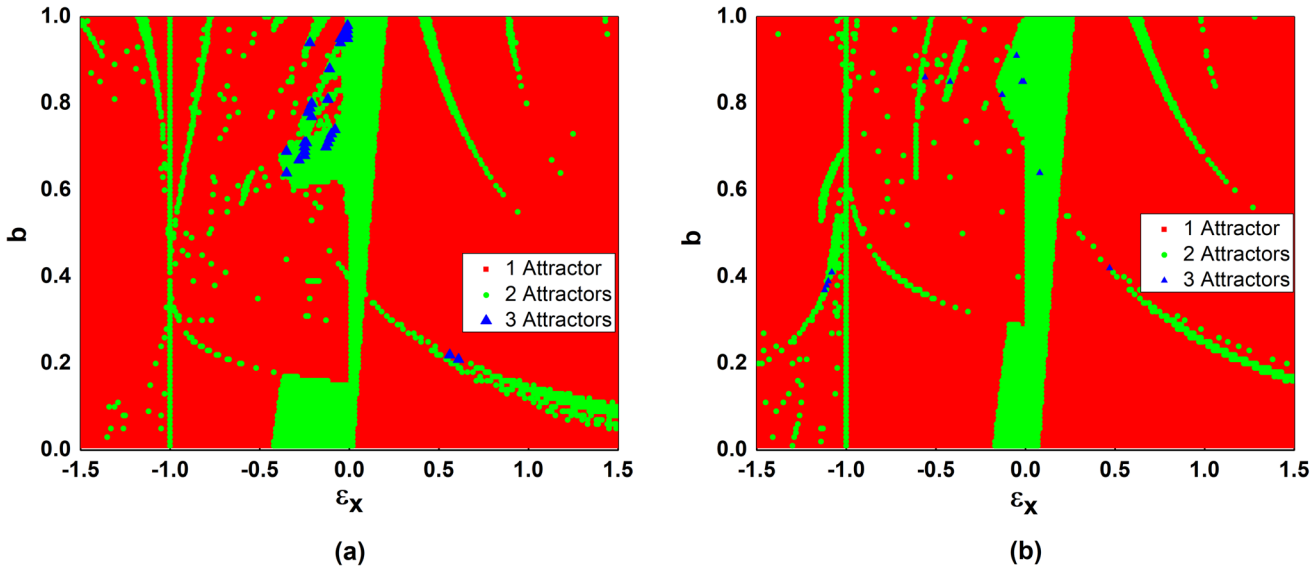

Fig. 6 Phase diagram for several attractors found for various combinations of ϵ_x and b. Here, (**a**) $a = 1.4$ and (**b**) $a = 1.7$. *Red* color corresponds to parameter values leading to a single attractor while *green* represents two attractors. *Blue* color symbolizes three attractors

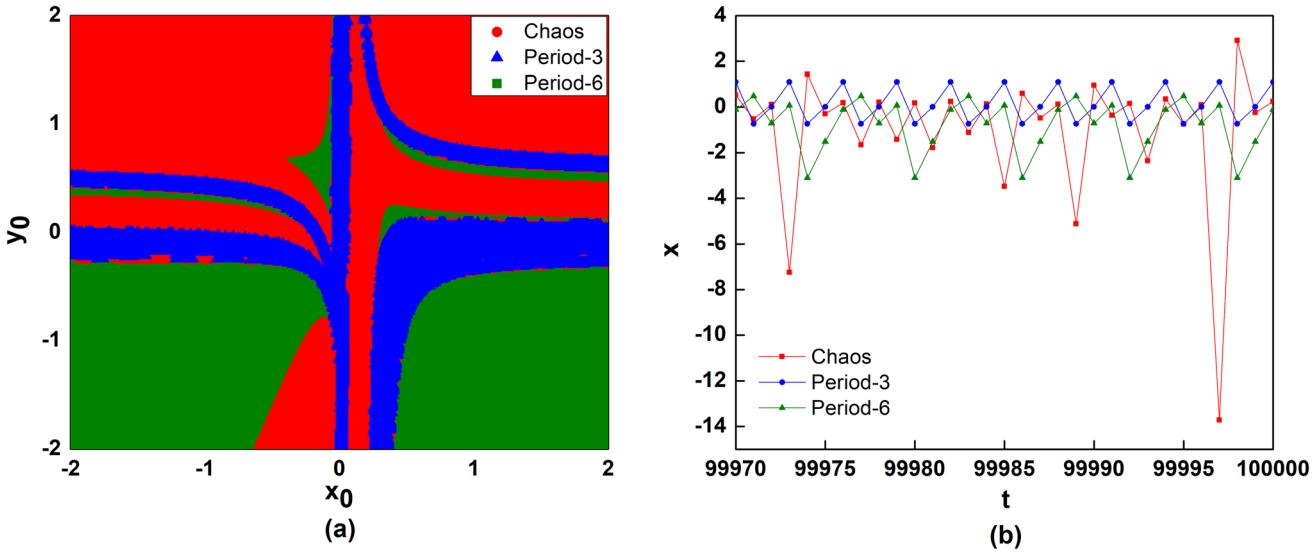

Fig. 7 (**a**) Basin of attractor for $a = 1.7$, $b = 0.3899$, and $\epsilon_x = -1.1$. Figure shows the existence of three different attractors for different initial conditions. (**b**) Time series for different values of initial conditions showing three different attractors

$$\begin{aligned} x_{(n+1)} &= f([x_n]_{q_x}, y_n) \\ y_{(n+1)} &= g([x_n]_{q_x}, y_n) \end{aligned} \tag{5}$$

If we deform only the y-variable, the equations are as follows:

$$\begin{aligned} x_{(n+1)} &= f(x_n, [y_n]_{q_y}) \\ y_{(n+1)} &= g(x_n, [y_n]_{q_y}) \end{aligned} \tag{6}$$

We introduce new variables ϵ_x and ϵ_y such that $\epsilon_x = 1 - q_x$ and $\epsilon_y = 1 - q_y$. As $q_x \to 1, \epsilon_x \to 0$ and as $q_y \to 1, \epsilon_y \to 0$

We study the attractors and possible multistability in this system under the variation of various parameters. (For $\epsilon_x = -1$, $x_{q_x} = 1$ always. Similarly for $\epsilon_y = -1$, $y_{q_y} = 1$ always. We do not study these pathological cases. But we note that in all the bifurcation diagrams, we certainly observe a bifurcation near $\epsilon_x = -1$ or $\epsilon_y = -1$.) The study

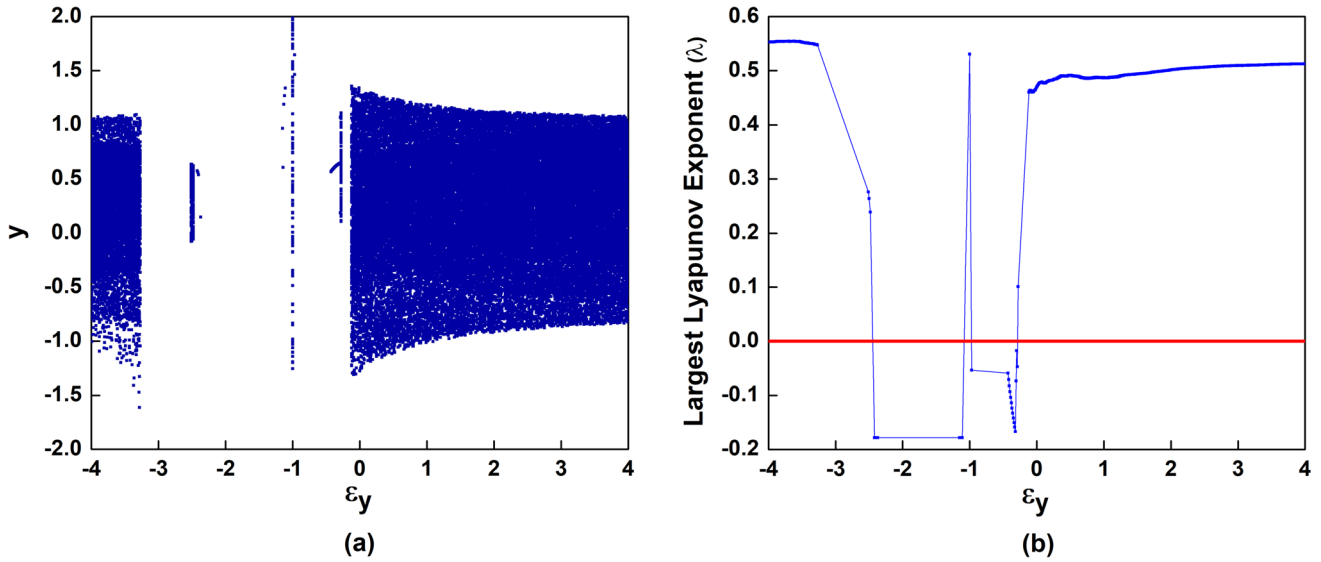

Fig. 8 (**a**) Bifurcation diagram of the Lozi map is plotted as a function of the deformation variable ϵ_y. The deformation range is $-4 \leq \epsilon_y \leq 4$. The parameter values are $a = 1.7$ and $b = 0.5$. (**b**) Shows the largest Lyapunov exponent λ plotted as a function of ϵ_y

of multistable systems has many applications and has attracted a lot of interest in the past [37].

We also study two diffusively coupled q-deformed Lozi maps in the last section. In this case, both variables are q-deformed. There is a possible blow up when $x = \frac{1+\epsilon_x}{\epsilon_x}$ or $y = \frac{1+\epsilon_y}{\epsilon_y}$. We ignore the initial conditions that correspond exactly to the pole of the function. However, if the values are close to the pole and not exactly at the pole, their value can immediately reduce due to the q-deformation, and the trajectories do not escape to infinity. Thus, q-deformation could lead to the confinement of the trajectories that could blow up in the absence of deformation. We illustrate it with the following example. Consider the Lozi map for $a = 1.4$ and $b = 0.3$. In the absence of q-deformation, there is a single chaotic attractor obtained for initial conditions in the basin of this chaotic attractor. All the initial conditions outside this basin blow up to infinity (See Fig. 1a). For q-deformation values $\epsilon_x = 0.01$ and $\epsilon_y = 0.01$, the basin of the chaotic attractor does not change much. However, the initial conditions that reached infinity in the absence of deformation tend towards a fixed point for these values. Thus, there are two coexisting attractors—a chaotic attractor and a fixed point. The basin of the chaotic attractor is connected simply (See Fig. 1b). As we shall see later, in case of double deformation, a few initial conditions blow up to infinity.

2.1. Case I: q-deformed x-variable

First, we study the dynamics of the Lozi map with the q-deformed x variable only, keeping the y variable untouched. We study the bifurcation diagrams, the Lyapunov exponent, and the phase diagrams to reveal the parameter-dependent bifurcation behavior and multistability. The bifurcation diagram is a great tool to comprehend the dynamics of a system. Figure 2a shows the bifurcation diagram of the q-deformed x variable as a function of the deformation variable ϵ_x in the range $[-4 : 4]$. We start with a random initial condition with control parameter $a = 1.7$, $b = 0.5$.

We observe period-2 state for $\epsilon_x < -1$. A crisis is observed at $\epsilon_x = -0.89$ and a chaotic regime begins. Another period-2 state extends from $\epsilon_x = 0.33$ to 1.5. Eventually, the periodicity ceases to exist, and a chaotic region is observed in range $\epsilon_x \in [1.5, 4]$. We calculate the finite-time largest Lyapunov exponent (λ) to affirm the existence of chaos by iterating the q-deformed Lozi map 10^5 times. At $\epsilon_x = 1.6$, the largest Lyapunov exponent $\lambda = 0.27495$ and at $\epsilon_x = -0.64$, $\lambda = 0.51242$. A positive value implies chaos. λ is plotted as a function of deformation parameter ϵ_x in the range $-4 \leq \epsilon_x \leq 4$ in Fig. 18b. As expected, we obtain a positive Lyapunov exponent in the chaotic regions.

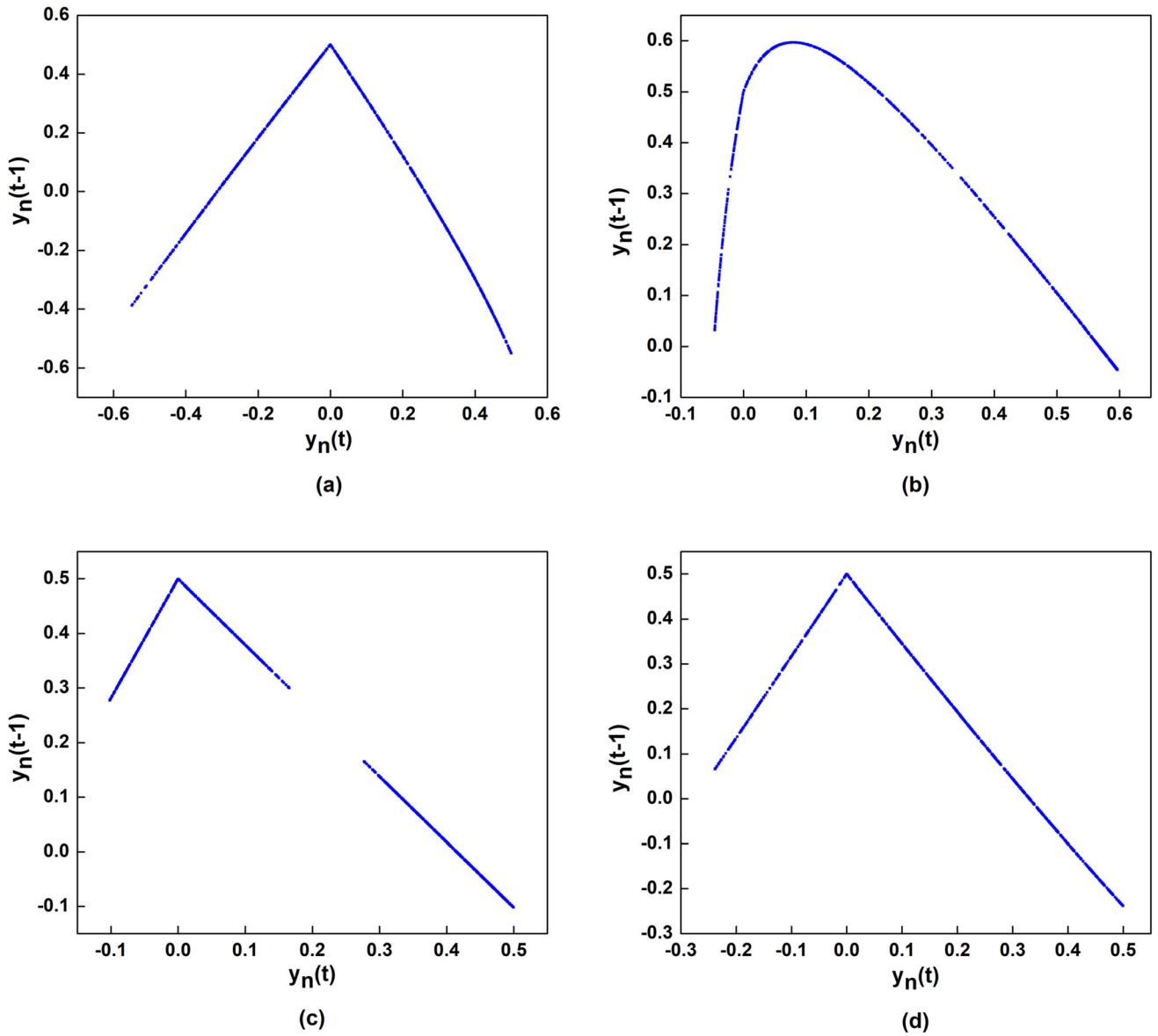

Fig. 9 A continuous strange attractor is obtained in case of y variable q-deformed Lozi map (**a**) for $\epsilon_y = -4.5$. (**b**) Shows a continuous attractor obtained for $\epsilon_y = -0.9$. (**c**) A discontinuous attractor obtained for $\epsilon_y = 0.02$. We observe a discontinuity between $\epsilon_y = 0.16 - 0.27$. (**d**) Shows a continuous attractor obtained for $\epsilon_y = 2.5$

The attractors obtained for small values of deformation $\epsilon_x = -0.02$ and $\epsilon_x = 0.1$ are shown in Fig. 3a and b, respectively. Deforming the x variable does not immediately change the nature of the attractor. However, it changes completely for large deformation values of ϵ_x. We show the attractor for $\epsilon_x = -0.8$ and $\epsilon_x = 2$ in Fig. 3c and d, respectively. The chaotic region and periodic orbits are interspersed. For example, we observe a period-8 attractor for $\epsilon_x = 3.1$ and a period-16 attractor for $\epsilon_x = 2.998$ (See Fig. 4a and b). Multistability can be observed for some of the deformation values ϵ_x. We observe two different attractors for different initial conditions for deformation parameters $\epsilon_x = -0.912$ and 0.05. The initial conditions that blew up in the absence of the deformation ($\epsilon_x = 0$) are

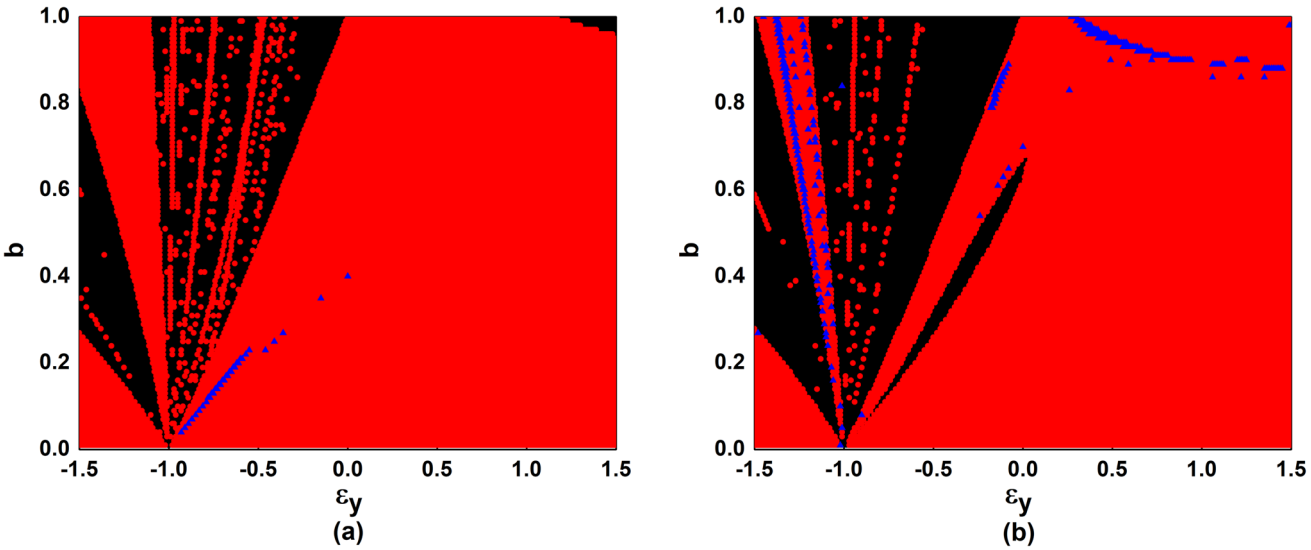

Fig. 10 Phase diagram for several attractors found for various combinations of ϵ_y and b. Here, (**a**)$a = 1.4$ and (**b**) $a = 1.7$. *Red* color corresponds to parameter values where all initial conditions blow up. *Black*color stands for the parameter values for which some initial conditions lead to an attractor and some blow up. *Blue* color represents the parameter values where two distinct attractors exist with initial states that blow up

now in the basin of attraction of the fixed point. The basins of coexisting attractors for $\epsilon_x = -0.912, 0.05$ are shown in Fig. 5a and b. Here, we represent the different initial conditions leading to different dynamics by different colors. Coexisting period-2 orbit and chaos are observed for $\epsilon_x = -0.912$. Fixed point and chaotic attractor coexist for $\epsilon_x = 0.05$. The basins could be either smooth or intermingled. In one case, the basins are intermingled. While in the other, they are well separated.

We carry out a systematic study of multistability for control parameter values $a = 1.4$ and $a = 1.7$ for various values of ϵ_x and b. Coexisting attractors were observed only for a small range of ϵ_x. In this region, the basin is fragmented and the nearby initial conditions can lead to entirely different attractors. For $\epsilon_x > 0$, we find a chaotic attractor coexisting with the fixed point for small values of ϵ_x. This is similar to the doubly deformed case discussed above.

We plot a phase diagram consisting of regions of different asymptotic number of attractors for $a = 1.4, 1.7$. There are predominantly two regions: a) a single attractor and b) two attractors. Few values of b and ϵ_x lead to three attractors. They are often on the borderline of the one attractor and two attractor phases. (Fig. 6). We do not come across the parameter values that yield more than three possible attractors. The q-deformation of the x variable leads to a very stable system, and any initial condition rarely blows up. Thus, the system remains bounded for most parameter values and initial conditions. We consider a case where there are three possible attractors. We have shown three basins of attraction for parameter values $a = 1.7$, $b = 0.3899$, and $\epsilon_x = -1.1$ (Fig. 7a). These are smooth basins. We have observed period-3, period-6, and chaotic attractors for different initial conditions. Three different asymptotic time series for various initial conditions are shown in Fig. 7b.

2.2. Case II: q-deformed y-variable

We study the effect of the q-deformed y variable on the dynamics of the Lozi map, while keeping the x variable as it is. Figure 8a shows the bifurcation diagram of the q-deformed y variable. The diagram is plotted over the range of deformation parameter $-4 \leq \epsilon_y \leq 4$. The control parameters are $a = 1.7$ and $b = 0.5$. We observe a region of strange chaotic attractor extending from $\epsilon_y = -4$ to -3.1. Two disjoint bands in the attractor come together, and a single continuous attractor is observed in this range. The Lyapunov exponent λ in this range is small but positive as shown in Fig. 8b.

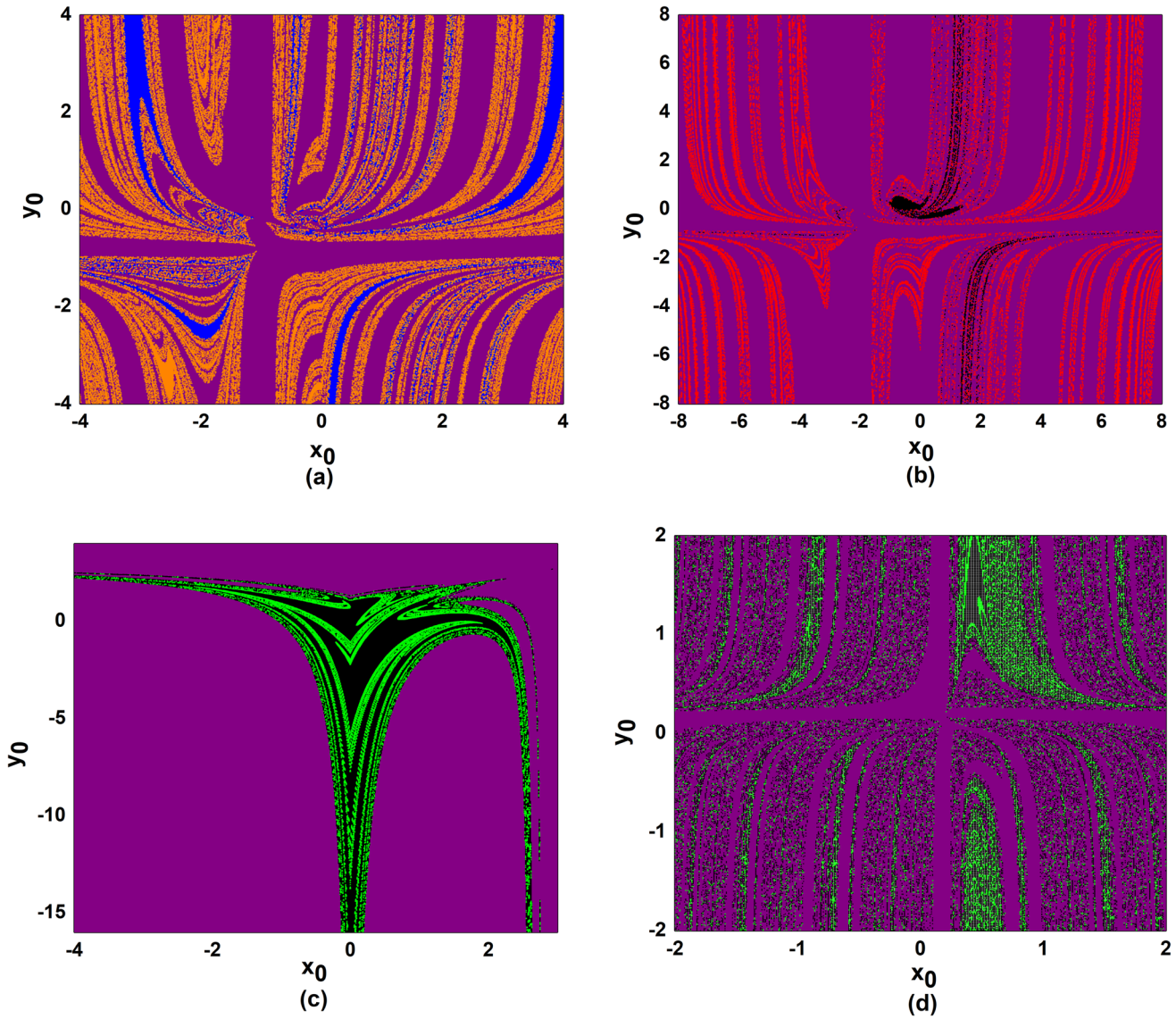

Fig. 11 Basin of attractor for (**a**) control parameter $a = 1.4$, $b = 0.789$ and $\epsilon_y = -0.55$. The color code is *purple* = ∞, *blue* = period-8, *yellow* = chaos, (**b**) control parameter $a = 1.4$, $b = 0.3889$ and $\epsilon_y = -0.56$. The color code is *purple* = ∞, *black* = period-2, *red* = 6-band attractor, (**c**) control parameter $a = 1.7$, $b = 0.9499$ and $\epsilon_y = 0.4699$. The color code is *purple* = ∞, *black* = period-2, *green* = period-6, and (**d**) control parameter $a = 1.7$, $b = 0.9699$ and $\epsilon_y = -1.23$. The color code is *purple* = ∞, *black* = period-2, *green* = period-6

Unlike the case of q-deformed x variable, some initial conditions always blow up. The nature of the Lozi attractor changes as well. An attractor obtained at $\epsilon_y = -4.5$ is shown in Fig. 9a. Figure 9b shows a strange attractor at $\epsilon_y = -0.9$ which is not linear. The attractor at $\epsilon_y = 0.02$ comprises two chaotic bands (Fig. 9c). A strange attractor with discontinuity is observed between $0.16 - 0.27$. The attractor becomes continuous with an increase in the strength of the deformation variable ϵ_y. With further increase in ϵ_y, the bands merge, and we obtain a single continuous attractor for $\epsilon_y = 2.5$ as shown in Fig. 9d. The nature of the strange attractor is entirely different from that of the q-deformed x variable case.

We carry out an extensive study of multistability, for $a = 1.4$ and $a = 1.7$ for various values of b and ϵ_y. We show the phase diagram for the parameter values at which

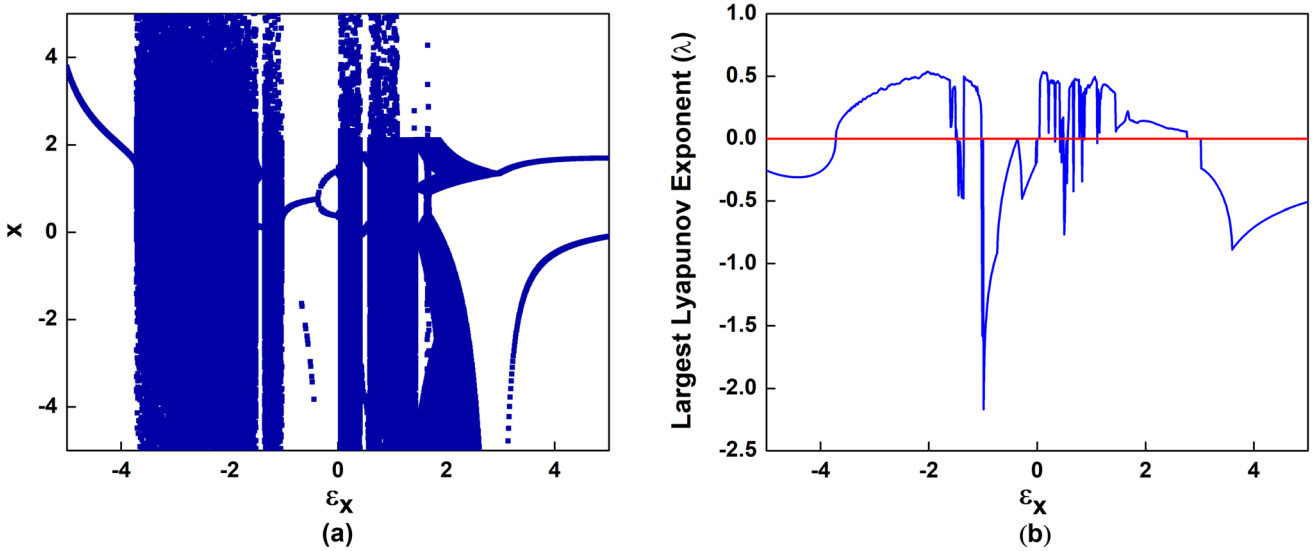

Fig. 12 (**a**) Shows the bifurcation diagram of a doubly q-deformed Lozi map for a fixed value of $\epsilon_y = -1.1$. The control parameters $a = 1.7$ and $b = 0.5$. The diagram is plotted over the range $-5 \leq \epsilon_x \geq 5$. (**b**) Shows the plot of the largest Lyapunov exponent λ calculated over the deformation range $-5 \leq \epsilon_x \leq 5$. ϵ_y fixed at -1.1

we have a) all the initial conditions leading to infinity b) some initial conditions leading to blow-up coexisting with conditions leading to a single attractor, and c) initial conditions that can blow up or lead to two possible attractors (See Fig. 10). Because we do not consider infinity to be an attractor, true multistability can be claimed only for case c). In such cases, we observe a rich structure as shown in Fig. 11. Fig. 11 show a basin of attractors obtained for $a = 1.4$ and $a = 1.7$ for different values of ϵ_y and b.

2.3. Case III: Doubly q-deformed

In this section, we simultaneously q-deform the x and y variables. Now we have multiple free parameters a, b, ϵ_x and ϵ_y. For convenience, we fix ϵ_y and study the parameter dependence on ϵ_x and b, for $a = 1.4$ and $a = 1.7$. We study two cases (a) $\epsilon_y = -1.1$ and (b) $\epsilon_y = 1.1$, for the existence of multistability for different values of ϵ_x.

The bifurcation diagram with varying deformation variable ϵ_x in the range $-5 \leq \epsilon_x \leq 5$ keeping $\epsilon_y = -1.1$ is shown in Fig. 12a. We observe an extended chaotic regime in the range $-3.77 < \epsilon_x < -1.5$, followed by period-2 orbit up to -1.38. Another chaotic region emerges in the range $-1.38 < \epsilon_x < -0.95$. We plot the largest Lyapunov exponent of the doubly q-deformed Lozi map for ϵ_y fixed at -1.1 and ϵ_x in the range [-5:5] in Fig. 12b). Several periodic attractors were observed for positive values of ϵ_x which cannot be noticed in the bifurcation diagram (See Fig. 13a–c). Period-6, period-9 and period-3 orbits are obtained for $\epsilon_x = 0.42$, 0.45, and 0.5, respectively. The nature of the strange attractor obtained at $\epsilon_x = 0.8$ is shown in Fig. 13d. We further investigate the underlying initial value-dependent coexisting dynamical phenomenon by varying the strength of the q-deformed variable ϵ_x keeping $\epsilon_y = -1.1$. We obtain the kinetic map for $\epsilon_x = -0.0499$. In the initial value plane, some set of initial conditions adhere to period-2 and period-6 attractor, while the rest of them are fixed points (See Fig. 14a). Figure 14b shows the coexistence of chaotic attractor and fixed points for $\epsilon_x = -0.8$. At the onset of the fixed point emerging into period-2, we observe the coexistence of the period-2 orbit and fixed point at $\epsilon_x = -0.3$ (see Fig. 14c). Figure 14d shows the fixed points and period-4 orbit coexisting at the transition of period-2 to period-4 for $\epsilon_x = 0.02$.

In case (b) we fix $\epsilon_y = 1.1$. We observe multistability in this case as well. Figure 15a shows the bifurcation diagram plotted over the range $-5 \leq \epsilon_x \leq 5$. Period-2 orbit extends up to $\epsilon_x = -1.46$, which leads to period-4 orbit. A chaotic regime begins at $\epsilon_x - 1.21$. Another chaotic region extends between -0.8 to -0.25. It is followed by two bands merging into period-4 and eventually period-2 orbit. Another chaotic region extends in the range $2 \leq \epsilon_x \leq 5$. The

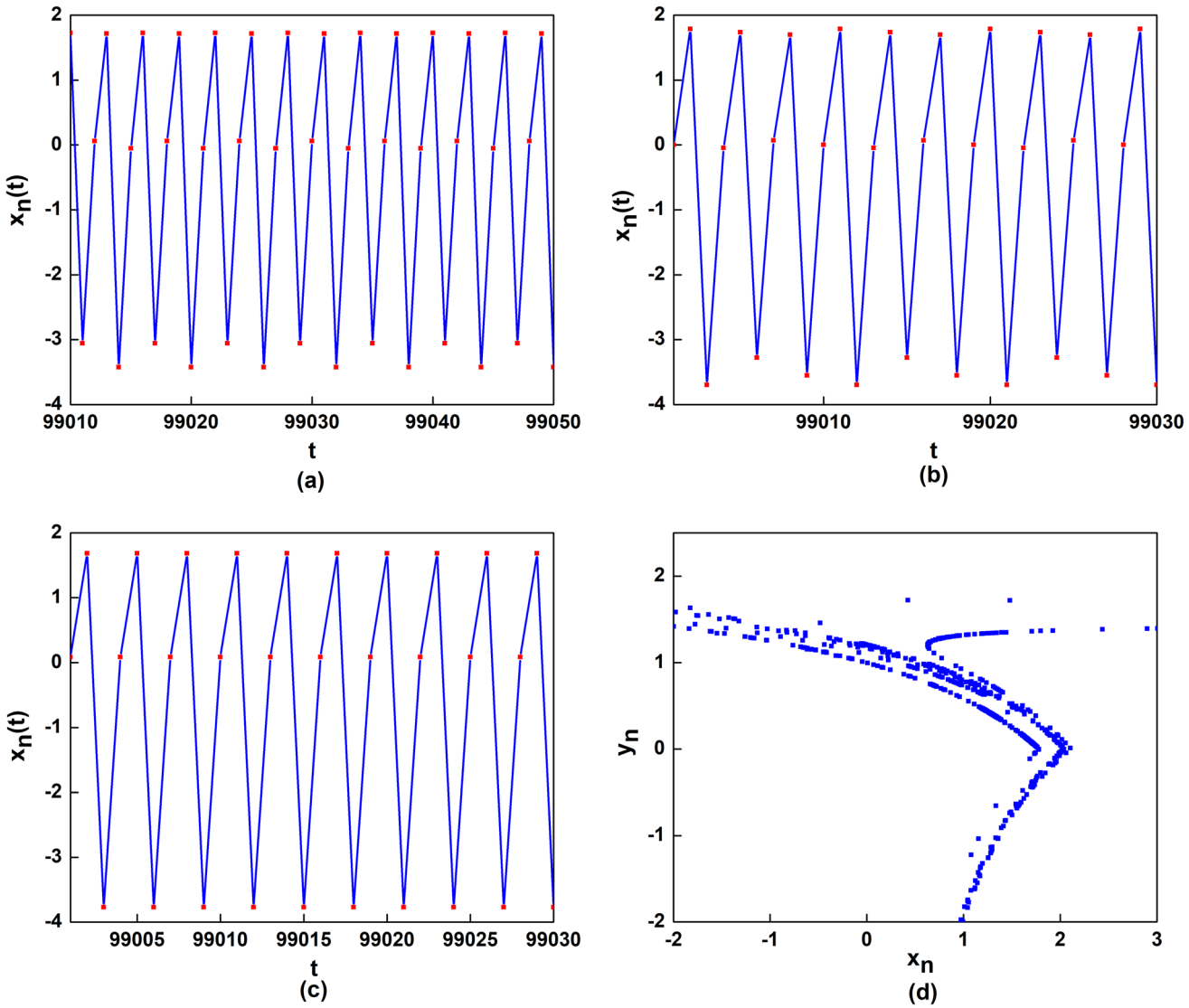

Fig. 13 (**a**) Represents period-6 attractor existing in the doubly q-deformed Lozi map for $\epsilon_x = 0.42$ and $\epsilon_y = -1.1$. (**b**) shows period-9 attractor obtained at $\epsilon_x = 0.45$. (**c**) shows the time evolution of period-3 attractor obtained for $\epsilon_x = 0.5$. (**d**) Shows a strange attractor obtained for $\epsilon_x = 0.8$. ϵ_y is fixed at -1.1 in all cases

plot of the Lyapunov exponent is shown in Fig. 15b. Figure 16a shows the time evolution of period-6 attractor obtained for $\epsilon_x = -1.18$ and $\epsilon_y = 1.1$. Figure 16b–d shows the change in dynamics of the strange attractor with a change in the value of ϵ_x. For $\epsilon_x = 0.45$, the strange attractor shows a single discontinuity in the range $0.22 - 0.8$ (See Fig. 16c). For $\epsilon_x = 0.55$ the strange attractor shows multiple discontinuities in the range -0.63 to $-0.17, 0.12 - 0.96$ and $0.75 - 0.99$ (Fig. 16d).

Multistability is reflected in Fig. 17a–d. We represent the initial values emerging into different dynamics with the help of different color regions. In Fig. 17a, we observe coexisting period-6 and chaotic attractor for $\epsilon_x = -1.18$ in the initial value plane. Period-10 and period-8 attractors are found to be coexisting for $\epsilon = -1.05$(See Fig. 17b). Figure 17c and d shows chaotic and fixed points existing simultaneously for $\epsilon_x = 0.0599$ and $\epsilon_x = -0.1$, respectively. The number of initial conditions converging to chaotic dynamics increases with an increase in ϵ_x. In all the

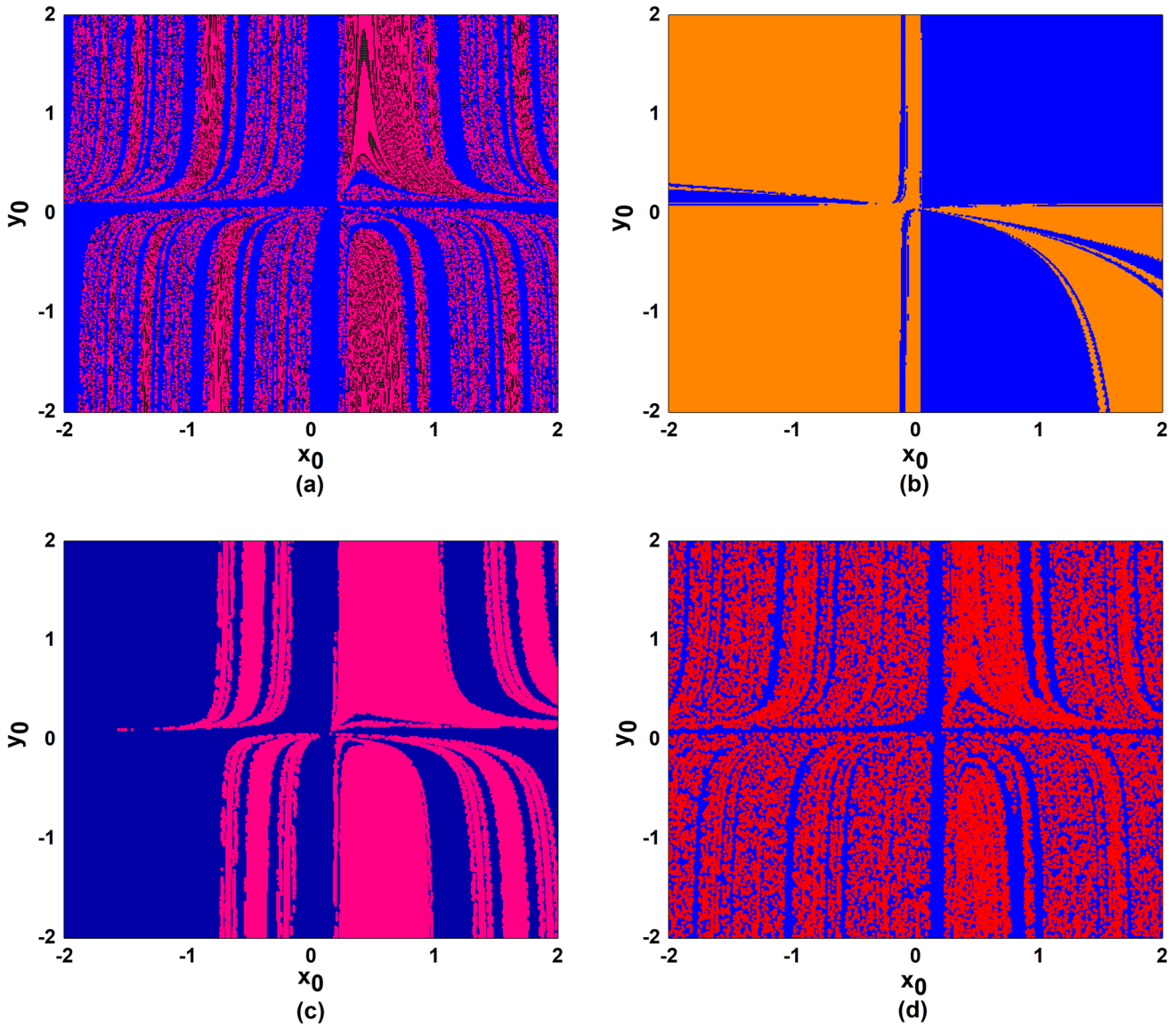

Fig. 14 We have plotted various basins for $\epsilon_y = -1.1$ for various values of ϵ_x. (**a**) For $\epsilon_x = -0.0499$, we find the coexistence of the fixed point(*blue*), period-2 (*pink*), period-6 (*black*). (**b**) For $\epsilon_x = -0.8$, we find the coexistence of the chaotic (orange) and the fixed points (*blue*). (**c**) For $\epsilon_x = -0.3$, we find coexisting fixed points (*blue*) and the period-2 attractor (*pink*). (**d**) For $\epsilon_x = 0.02$, we observe the fixed points (*blue*) attractor coexisting with a period-4 (*red*)

above cases, we study the coexisting hidden periodic orbit, chaotic attractor, and fixed points that are not evident in the bifurcation diagrams. The existence of a hidden attractor confirms the existence of multistability in the doubly q-deformed Lozi map.

We carry out a systematic study of multistability for $a = 1.4$ and $a = 1.7$ for various values of ϵ_x, ϵ_y and b. We study the basin of attractor for $a = 1.4$, $b = 0.3$, $\epsilon_x = -0.6599$, $\epsilon_y = -1.6499$ and $a = 1.7$, $b = 0.5$, $\epsilon_x = -0.9799$, $\epsilon_y = -1.6599$(See Fig. 18). The basin of attractors is well-distributed in the case of $a = 1.4$ whereas we obtain completely intermingled basins for $a = 1.7$. We plot the phase diagram of different attractors obtained for $a = 1.4, b = 0.3$ and $a = 1.7, b = 0.3$ for different combinations of ϵ_x and ϵ_y (See Fig. 19). The green color represents parameter values that lead to one attractor, red leads

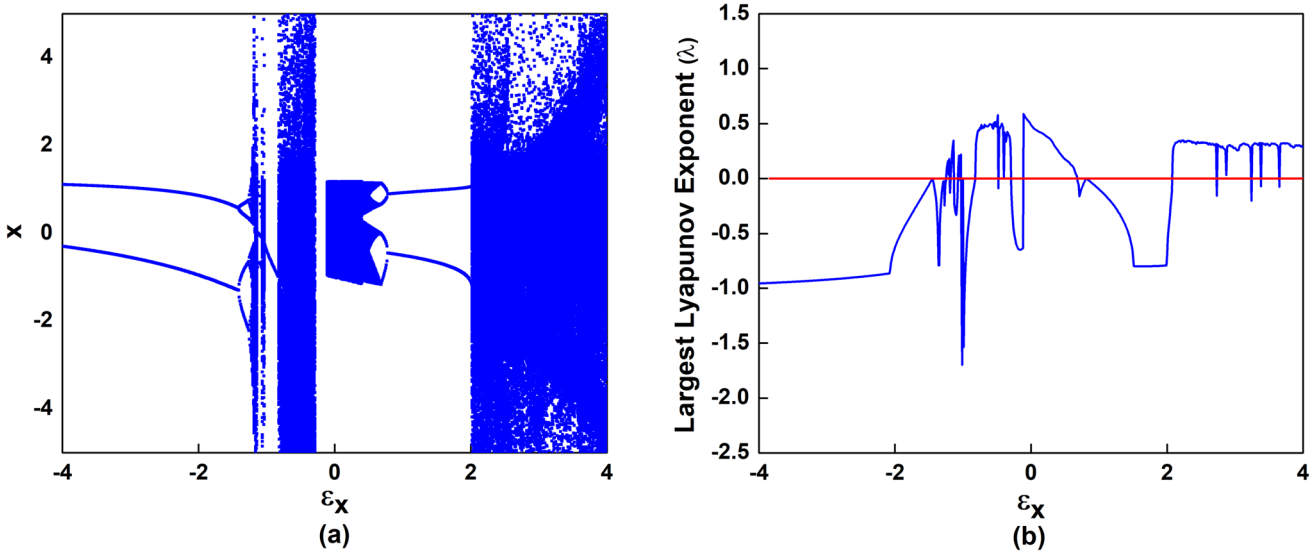

Fig. 15 (**a**) Shows the bifurcation diagram of the doubly q-deformed Lozi map for a fixed value of deforming parameter $\epsilon_y = 1.1$. Here $a = 1.7$ and $b = 0.5$. The range of deformation parameter is $-4 \leq \epsilon_x \leq 4$. (**b**) Represents the largest Lyapunov exponent λ obtained for deformation parameter ϵ_x in the range $[-4 : 4]$

to two attractors, and blue leads to three attractors. Single attractor and double attractor regions are dominant in the parameter space. Very few parameter values lead to coexisting three attractors. The q-deformation of both variables has rarely led to initial conditions that blow up to infinity. Therefore, the system remains bounded similar to the q-deformed x variable only.

3. Coupled q-deformed Maps

Multistability can be observed often in coupled systems due to an increase in complexity. It has resulted in the loss of synchronization in the case of Logistic maps [38] and Hénon map [39, 40].

We study chaotic synchronization in two doubly deformed Lozi maps. We simultaneously deform both x and y variables and define two coupled maps in a standard manner. The first map is attributed the variables $(x1, y1)$ and the second has $(x2, y2)$. The coupling constant is d.

The coupled q-deformed Lozi map is as follows:

$$x1_{(n+1)} = (1-d)f([x1_n]_{\epsilon_x}, [y1_n]_{\epsilon_y}) + df([x2_n]_{\epsilon_x}, [y2_n]_{\epsilon_y})$$
$$y1_{(n+1)} = (1-d)g([x1_n]_{\epsilon_x}, [y1_n]_{\epsilon_y}) + dg([x2_n]_{\epsilon_x}, [y2_n]_{\epsilon_y})$$
$$x2_{(n+1)} = (1-d)f([x2_n]_{\epsilon_x}, [y2_n]_{\epsilon_y}) + df([x1_n]_{\epsilon_x}, [y1_n]_{\epsilon_y})$$
$$y2_{(n+1)} = (1-d)g([x2_n]_{\epsilon_x}, [y2_n]_{\epsilon_y}) + dg([x1_n]_{\epsilon_x}, [y1_n]_{\epsilon_y})$$

where,

$$[x]_{\epsilon_x} = \frac{x}{1+\epsilon_x(1-x)}$$
$$[y]_{\epsilon_y} = \frac{y}{1+\epsilon_y(1-y)}$$

The Jacobian around a synchronized solution (x_n, y_n, x_n, y_n) is given by:

$$J_n = \begin{bmatrix} (1-d)f_x & (1-d)f_y & df_x & df_y \\ (1-d)g_x & (1-d)g_y & dg_x & dg_y \\ df_x & df_y & (1-d)f_x & (1-d)f_y \\ dg_x & dg_y & (1-d)g_x & (1-d)g_y \end{bmatrix} \tag{7}$$

where

$$f_x = \frac{\partial f([x_n]_{\epsilon_x}, [y_n]_{\epsilon_y}, [x_n]_{\epsilon_x}, [y_n]_{\epsilon_y})}{\partial x_n}$$

and f_y, g_x and g_y are defined analogously. This matrix can be block diagonalized as:

$$J_n = \begin{bmatrix} f_x & f_y & 0 & 0 \\ g_x & g_y & 0 & 0 \\ 0 & 0 & (1-2d)f_x & (1-2d)f_y \\ 0 & 0 & (1-2d)g_x & (1-2d)g_y \end{bmatrix} \tag{8}$$

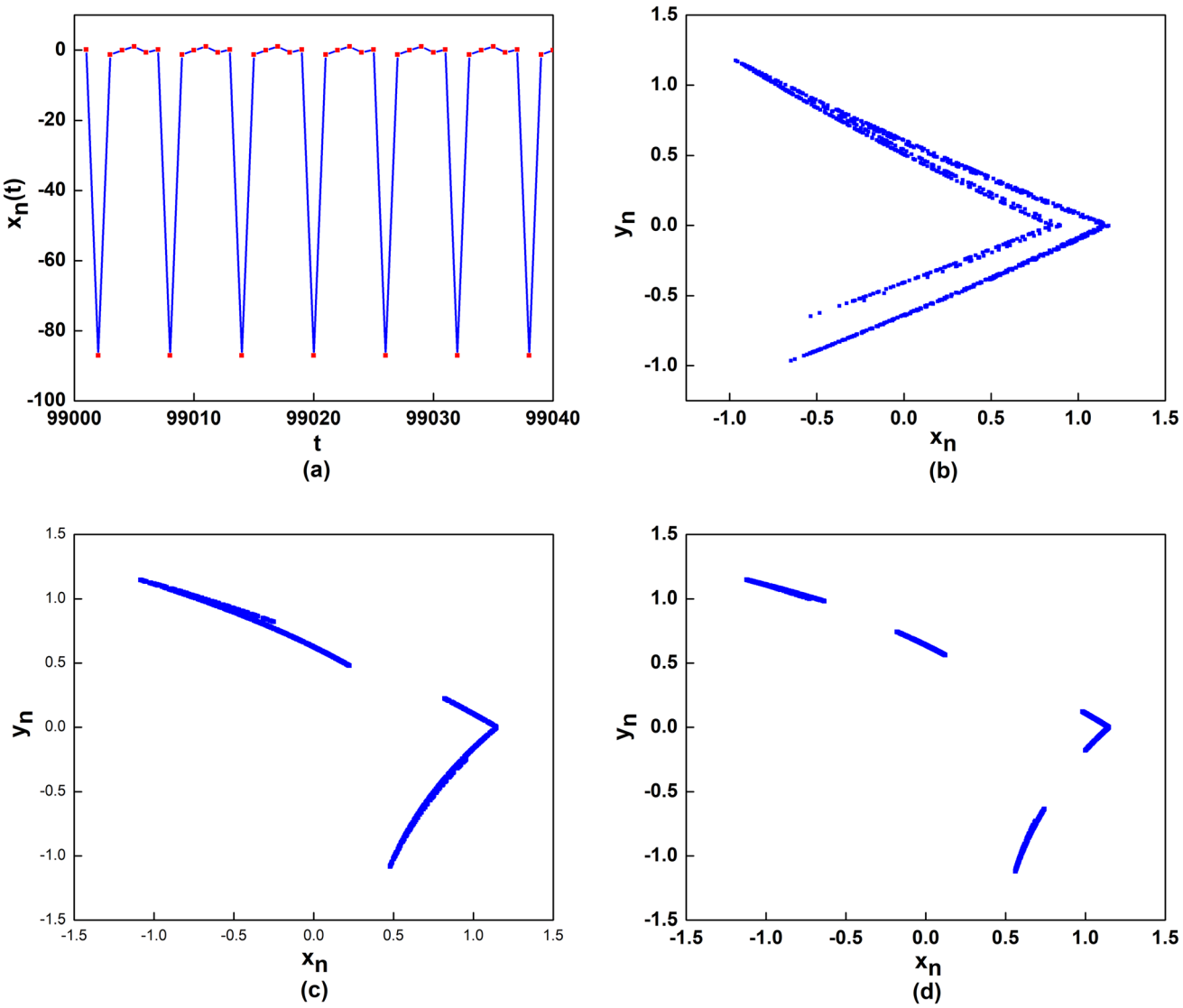

Fig. 16 (**a**) Shows the time evolution of period-6 attractor in the doubly deformed Lozi map for $\epsilon_x = -1.18$ and $\epsilon_y = 1.1$. (**b**) Existence of a strange attractor for $\epsilon_x = -0.1$. ϵ_y is fixed at 1.1 in all cases. (**c**) For $\epsilon_x = 0.45$, the strange attractor shows a single discontinuity in the range $0.22-0.8$. (**d**) For $\epsilon_x = 0.55$ the strange attractor shows multiple discontinuities in the range -0.63 to -0.17,$0.12-0.96$ and $0.75-0.99$

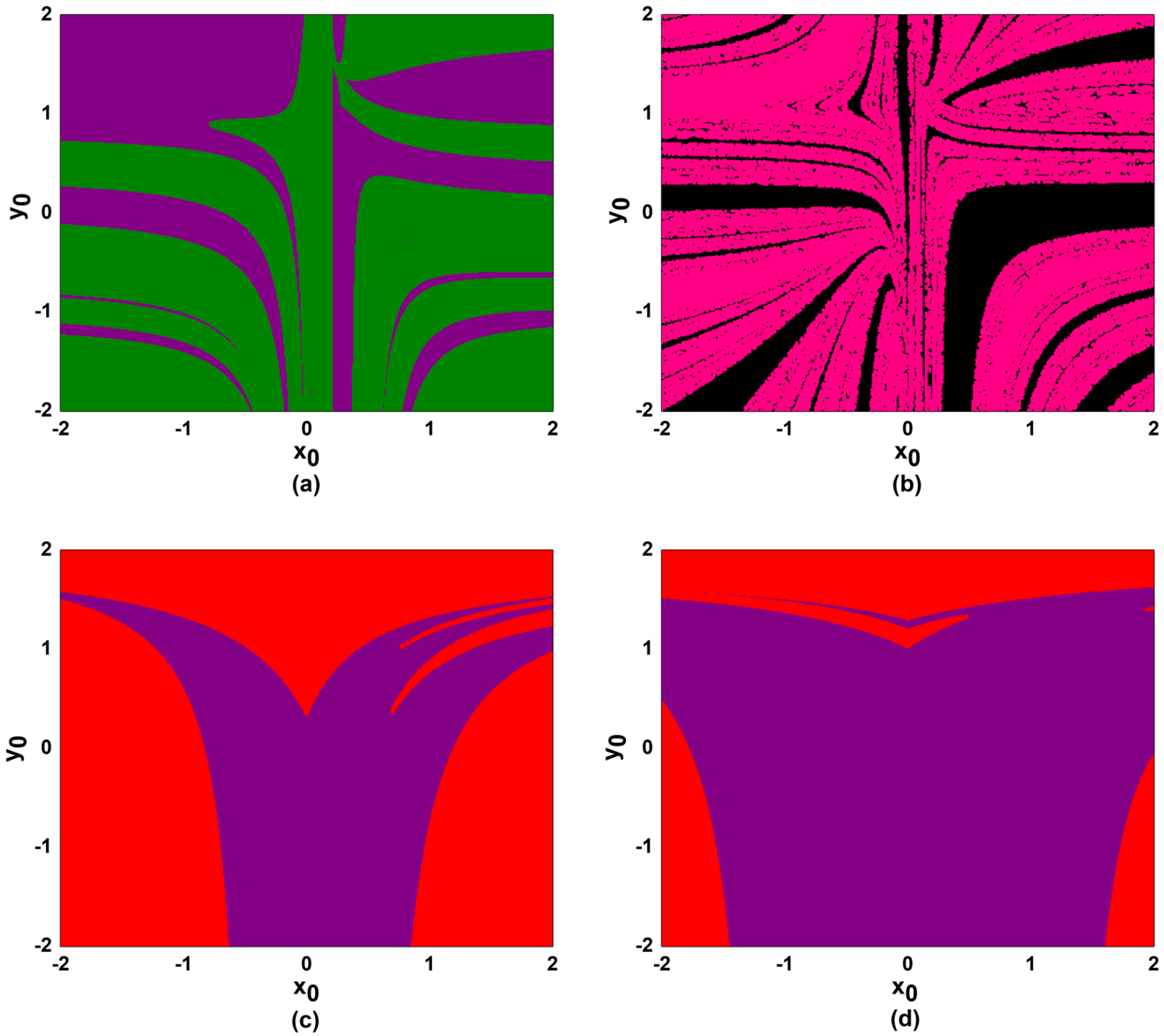

Fig. 17 Figure (**a**) shows the plot of initial conditions at $\epsilon_x = -1.18$. It shows the coexistence of period-6 (*green*) and chaotic attractor (*purple*). Figure (**b**) represents the coexistence of period-10 (*pink*) and period-8 (*black*) attractor for $\epsilon = -1.05$, (**c**) shows coexisting chaotic (*purple*) and fixed points (*red*) for $\epsilon_x = -0.1$ and (**d**) shows coexisting chaotic (*purple*) and fixed points (*red*) for $\epsilon_x = 0.0599$. The fraction of initial conditions converging to chaotic points increases with an increase in ϵ_x. In all these cases ϵ_y is fixed at 1.1

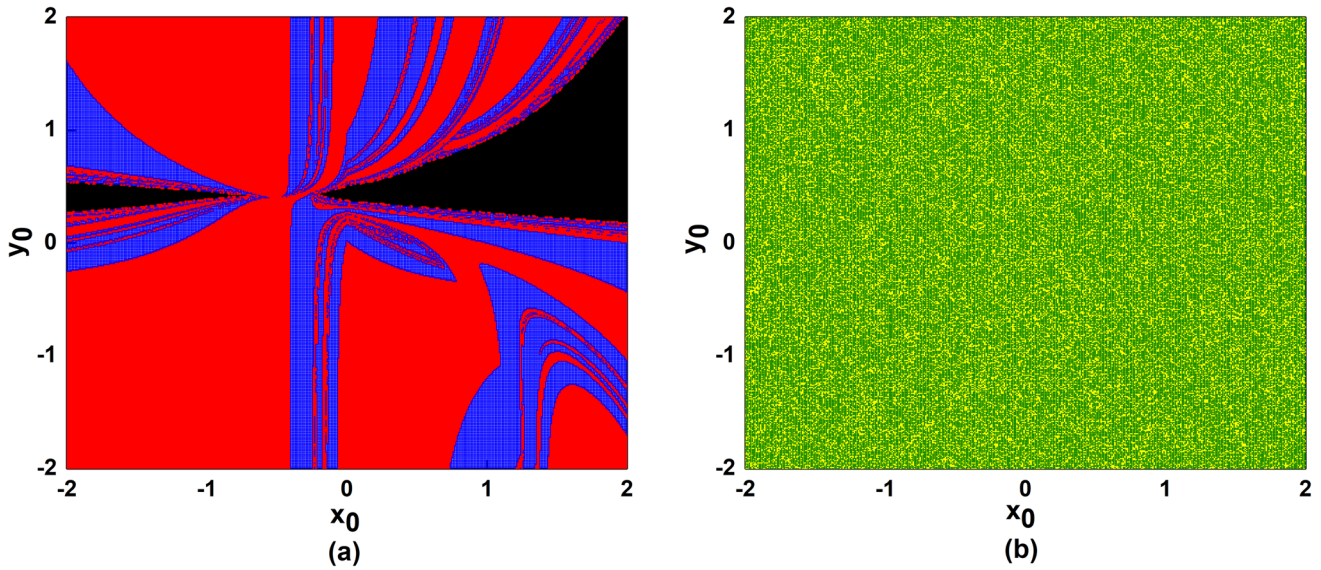

Fig. 18 Basin of attractors of doubly deformed Lozi system with (**a**)$a = 1.4,\ \ b = 0.3,\ \ \epsilon_x = -0.6599,\ \ \epsilon_y = -1.6499,$ (**b**) $a = 1.7,$ $b = 0.5,\ \epsilon_x = -0.9799,\ \epsilon_y = -1.6599$. In (**a**) initial conditions in *red* lead to period-2, *blue* lead to period-4, and *black* lead to fixed points. In (**b**), the initial conditions in *yellow* lead to chaos and green leads to period-3. Here, the basins appear completely intermingled

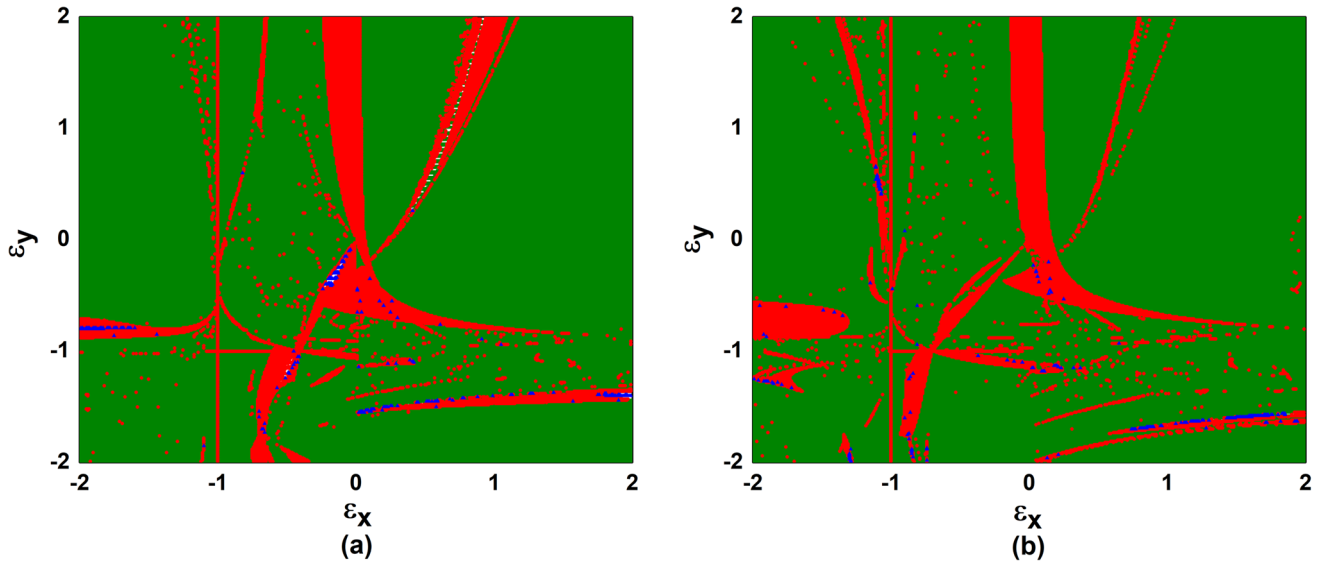

Fig. 19 Phase diagram for several attractors of doubly deformed Lozi system with (**a**) $a = 1.4$, $b = 0.3$, (**b**) $a = 1.7$, $b = 0.5$ for different combinations of ϵ_x and ϵ_y. The green color represents parameter values that lead to one attractor, red leads to two attractors, and blue leads to three attractors. Again, we observe that three attractors are obtained very rarely and are on the borderline of parameter values leading to one and two attractors

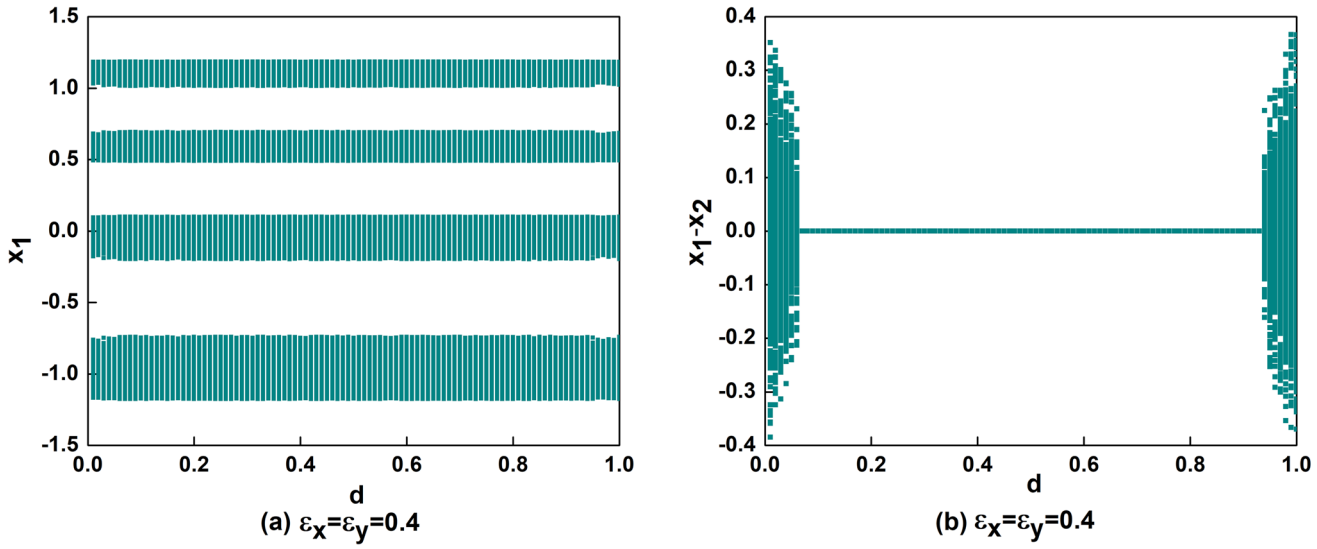

Fig. 20 We plot the last 1000 values of (**a**) $x1$ and (**b**)$x1 - x2$ after 5×10^6 iterates (for the parameter values $a = 1.7$, $b = 0.5$ and $\epsilon_x = \epsilon_y = 0.4$) as a function of coupling parameter d. We observe synchronization for $0.07 \leq d \leq 0.93$ as expected where $(x1 - x2) \sim 0$

This block-diagonalizing transformation does not depend on the variable values. Thus, the system is chaotic if a single map is in the chaotic region, and synchronized chaos is possible if $|(1 - 2d)\exp(\lambda_{max})| < 1$. Let $\epsilon_x = \epsilon_y = 0.4$. The other parameter values are $a = 1.7$ and $b = 0.5$. For $d = 0$, *i.e.,* the uncoupled case, the largest Lyapunov exponent is $\lambda_{max} = 0.143$. Thus, we observe chaotic synchronization for $0.07 \leq d \leq 0.93$ for close by initial conditions. This is the case indeed (See Fig. 20).

4. Conclusions

We study the dynamics of the Lozi map under q-deformation of a) the x variable only, b) the y variable only and c) both x and y variable. The control parameter values are $a = 1.4$ and $a = 1.7$ with different values of b. The case of the coupled q-deformed maps is studied in the last section. The bifurcation diagrams, Lyapunov exponents, phase portraits, and basins of the attractor are used to examine the underlying multistability in each case. Multistability is a significant feature. Even a slight perturbation can change the dynamics of the system from one attractor to another. In this case, the multistability is driven by initial conditions in the respective region of attraction for a given set of parameters. In the case of q-deformed x variable only, the phase diagram in the parameter space ϵ_x and b shows predominantly two regions comprising of a single attractor and a double attractor. Very few parameter values lead to three coexisting attractors. We find several coexisting attractors in the initial value plane. The different basins corresponding to different attractors can be intermingled or smoothly separated. The q-deformation of the x variable only rarely blows up to infinity. Therefore, the system remains bound for all the initial conditions studied for this case. The number of possible attractors is two or at the most three. We do not observe extreme multistability in any case.

We observe blow up to infinity in case of q-deformation of the y variable only. The phase diagram for the parameter values ϵ_y and b shows the cases where all the initial conditions lead to infinity, some initial conditions lead to blow up coexisting with initial conditions that lead to a single attractor and initial conditions that can blow up or lead to two possible attractors. Multistability can be claimed only in the last scenario. If both the variables are q-deformed, we find several coexisting attractors in the initial value plane. The phase diagram reveals several intermingled and well-separated phases. We obtain parametric regions with single and dual attractors primarily. The cases where three coexisting attractors exist often appear along the borderlines of single and double attractors. The system remains bound for all the initial conditions studied in this case, similar to the case of the q-deformed x variable.

In case of diffusively coupled q-deformed Lozi maps, we simultaneously q-deform both the variables. It is notable that, unlike the non-deformed map, the trajectories seldom escape to infinity in the case of doubly deformed and q-deformed x variables only. It implies that the system can be operated in a stable regime without blowing up. Secondly, we do not observe the same if only the y variable is deformed. Finally, in the doubly deformed case, we have a parameter regime consisting of a single chaotic attractor. It has a smooth basin. Such regime can be very useful in cryptography using chaotic synchronization. In the same

context, we have also established the synchronization criteria in doubly deformed maps. We have studied chaotic synchronization. Chaotic synchronization is observed for a range of coupling values. An analytic explanation for the same is obtained.

Acknowledgements P. M. Gade and D. D. Joshi thank the DST-SERB (CRG/2020/003993) for financial assistance.

References

[1] M Hénon *The Theory of Chaotic Attractors*, pp. 94–102 (2004)
[2] R Lozi *Le Journal de Physique Colloques* **39** 5 (1978)
[3] M Misiurewicz *Ann. New York Acad. Sci.* **357** 1 348 (1980)
[4] D Baptista, R Severino and S Vinagre *Int. J. Bifurc. Chaos Appl. Sci. Eng.* **19** 3 21 (2009)
[5] V Botella-Soler, J Castelo, J Oteo and J Ros *J. Phys. A Math. Theor.* **44** 30 305101 (2011)
[6] Z Elhadj *Lozi Mappings: Theory and Applications* (CRC Press) (2013)
[7] V Avrutin, M Schanz and S Banerjee *Nonlinearity* **19** 8 1875 (2006)
[8] P A Glendinning and D J Simpson *Trans. Math. Appl.* **4** 1 002 (2020)
[9] R Lozi *Algorithms* **16** 10 491 (2023)
[10] DD Joshi, PM Gade, S Bhalekar *Chaos Interdiscip. J. Nonlinear Sci.* **32**(11) (2022)
[11] R E Ecke, J D Farmer and D K Umberger *Nonlinearity* **2** 2 175 (1989)
[12] V I Arnold *Izv. Akad. Nauk SSSR Ser. Mat* **25** 1 21 (1961)
[13] D R da Costa, J G S Rocha, L S de Paiva and R O Medrano-T *Chaos Solitons Fractals* **144** 110688 (2021)
[14] H E Nusse, E Ott and J A Yorke *Phys. Rev. E* **49** 2 1073 (1994)
[15] Y-C Lai, C Grebogi and J Kurths *Phys. Rev. E* **59** 2907 (1999)
[16] D Aharonov, R Devaney and U Elias *Int. J. Bifurc. Chaos* **7** 02 351 (1997)
[17] R Jaganathan and S Sinha *Phys. Lett. A* **338** 3 277 (2005)
[18] L D Faddeev *Boletim da Sociedade Brasileira de Matemática - Bulletin/Brazilian Mathematical Society* **20** 1 47 (1989)
[19] M Jimbo *Int. J. Mod. Phys. A* **4** 15 3759 (1989)
[20] C Tsallis *J. Stat. Phys.* **52** 479 (1988)
[21] L Castellani, J Wess *Quantum Groups and Their Applications in Physics* (vol. 127, IOS Press) (1996)
[22] S Woronowicz *Rev. Math. Phys.* **12** 06 873 (2000)
[23] K-S Chung, W-S Chung, S-T Nam and H-J Kang *Int. J. Theor. Phys.* **33** 2019 (1994)
[24] G Gasper, M Rahman *Basic Hypergeometric Series* (vol. 96. Cambridge university press) (2011)
[25] G Andrews *The Theory of Partitions* (addision-wesley, Reading) (1976)
[26] L Carlitz *q-Bernoulli Numbers and Polynomials* (1948)
[27] F T Arecchi, R Badii and A Politi *Phys. Rev. A* **32** 402 (1985)
[28] F Prengel, A Wacker and E Schöll *Phys. Rev. B* **50** 1705 (1994)
[29] D Angeli, J E Ferrell Jr and E D Sontag *Proc. Nat. Acad. Sci.* **101** 7 1822 (2004)
[30] R M May *Nature* **269** 5628 471 (1977)
[31] D Gupta and V V M S Chandramouli *Pramana* **95** 4 175 (2021)
[32] V Patidar and K K Sud *Commun. Nonlinear Sci. Numer. Simul.* **14** 3 827 (2009)
[33] J Cánovas and M Muñoz-Guillermo *Int. J. Bifur. Chaos* **30** 08 2030021 (2020)
[34] S Ozaki and M Nunokawa *Proc. Am. Math. Soc.* **33** 2 392 (1972)
[35] V Patidar, G Purohit and K Sud *Int. J. Bifurc Chaos* **21** 05 1349 (2011)
[36] SV Iyengar, J Balakrishnan *Chaos Interdiscip. J. Nonlinear Sci.* **28** 113102 (2018)
[37] AN Pisarchik, U Feudel *Phys. Rep.* **540**(4) 167 (2014)
[38] R Carvalho, B Fernandez and R V Mendes *Phys. Lett. A* **285** 5–6 327 (2001)
[39] V Astakhov, A Shabunin, W Uhm and S Kim *Phys. Rev. E* **63** 5 056212 (2001)
[40] J Sausedo-Solorio and A Pisarchik *Phys. Lett. A* **375** 42 3677 (2011)

RP Current Trends In Applied Sciences
Vol. 2, No. 4 (October – December 2023) pp. 78–83
e-ISSN: 2583-7486

RESEARCH PLATEAU PUBLISHERS

Cite this article: S. Khangar, O.P. Chimankar, Y.S. Tamgadge, R.Y. Bakale, Ultrasonic and spectroscopic investigation of aqueous polyvinyl alcohol (PVA) solutions, *RP Cur. Tr. Appl. Sci.* 2 (2023) 78–83.

Original Research Article

Ultrasonic and spectroscopic investigation of aqueous polyvinyl alcohol (PVA) solutions

Sughanda Khangar[1,*], O.P. Chimankar[2], Y.S. Tamgadge[3], R.Y. Bakale[4]
[1]Department of Physics, Shivaji Science College, Congress Nagar, Nagpur – 440012 (MS) India
[2]PG Department of Physics, RTMNU, Nagpur – 440033 (MS) India
[3]Shri. Shivaji Arts, Commerce and Science College Motala Dist. Buldhana – 443103 (MS) India
[4] Department of Physics Mahatma Fule Mahavidyalaya, Warud India
*Corresponding author, E-mail: sugandhakhangar2000@gmail.com

ARTICLE HISTORY
Received: 30 June 2023
Revised: 10 Nov. 2023
Accepted: 11 Nov. 2023
Published online: 18 Nov. 2023

KEYWORDS
Ultrasonic velocity; Density; Viscosity; FTIR; UV.

ABSTRACT
Using distilled water as solvent, different weight percentages of polyvinyl alcohol solutions were prepared and were then examined using the FTIR, UV-visible, and ultrasonic pulse echo techniques. In physics, ultrasound is a vital and efficient research tool. Understanding the physicochemical behavior of liquids and determining the nature of molecular interactions have become increasingly important goals of the ultrasonic study of liquid mixtures. Additionally, it offers a powerful and trustworthy instrument for examining ultrasonic properties of polymer solution in the context of phase separation research. Ultrasonic velocity (u), Density (ρ) and viscosity (η) for aqueous polyvinyl alcohol have been measured at 2 MHz and at temperature range 288K-308K and at concentration range 0.05wt% to 0.3 wt% by pulse echo technique. From this data, acoustic parameters such as adiabatic compressibility (β_a), acoustic impedance (Z), relaxation time (τ) and free length (L_f) were calculated for aqueous PVA solutions. The results are interpreted as per the molecular interactions in the aqueous PVA solutions and compared with the results obtained from FTIR and UV- visible spectroscopy. PVA can be employed as a tablet binder in the pharmaceutical industry due to the interactions observed in the solutions. The strength of molecular interactions in aqueous PVA solutions is indicated by thermo acoustic parameters including ultrasonic velocity, density, viscosity, adiabatic compressibility, acoustic impedance, relaxation time, free length, etc.

1. Introduction

Many researchers have become interested in polyvinyl alcohol (PVA) because of its exceptional qualities, including hydrophilicity, biodegradability, biocompatibility, and nontoxicity. It is a non-toxic, water-soluble polymer that has been extensively used in numerous research fields [1-2], including biomedical and drug delivery systems [3]. Additionally, it possesses exceptional resistance to oil, grease, and solvents as well as film-forming and emulsifying properties. Due to its high hydrophilicity and processability, it might be combined with various polymers. High tensile strength, abrasion resistance, and oxygen barrier characteristics can be found in PVA films [3]. It is a potentially useful material with good charge storage, high dielectric strength, and dopant-dependent electrical and optical properties. It too has a backbone made of carbon chains with hydroxyl groups joined by methane carbon. These OH groups can serve as a hydrogen bonding source, which helps to create polymer blends and composites. One of the key elements affecting PVA's properties and uses is the water absorption it experiences. Additionally, PVA has a high density of hydroxyl groups, which act as cross-linking sites after being exposed to radiation, chemicalsor heat [4]. One of the main areas of study in both fundamental and practical aspects has been the spectroscopic and ultrasonic analysis of polymer solutions. A spectroscopic investigation that demonstrates substantial results on the polymer solution's spectroscopic and ultrasonic properties is required to modify and improve its properties.

2. Materials and methods

2.1 Materials

The polyvinyl alcohol solutions were made by adding a predetermined amount of water with a given weight of PVA. Then stirred it till to obtain clear solution. Then, the concentration was expressed in weight percent. Its range was set at 0.05 weight percent to 0.3 weight percent (i.e. 0.05wt%, 0.1wt%, 0.15wt%, 0.2wt%, 0.25wt%, and 0.3 wt%).

2.2 Methods

Using the MHF-400 pulser receiver at 2 MHz and a temperature range of 288 K to 308 K, the ultrasonic velocity was measured. Viscosity were measured by Oswald's viscometer's and density by Picknometer. With a precision of 0.1K, the temperature was maintained using a thermostatically regulated water circulation system with a Plasto Craft LTB -10 thermostat. The standard formulae shown below were used to determine various thermos-acoustical properties using experimental data on ultrasonic velocity, density, and viscosity [5-6].

(Eq. 1) to determine ultrasonic velocity.

$$u = (2d/t) \text{ m/sec}, \quad (1)$$

where, d is the separation between transducer and reflector and t is the travelling time period of ultrasonic wave.

(Eq. 2) to determine density

$$\rho = \frac{M_l}{M_w}\rho_w \text{ kg m}^{-3} \quad (2)$$

where, M_l and M_w are the mass of liquid and water respectively. ρ_w is the density of water.

(Eq. 3) to determine viscosity

$$\eta = \frac{\rho_l t_l}{\rho_w t_w}\eta_w \quad (3)$$

where ρ_l is the density of experimental liquid, ρ_w is the density of water, η_w is the viscosity of water, t_l is the time required to experimental liquid to flow from mark A to B in viscometer, and t_w is the time of flow of water.

(Eq. 4) to determine adiabatic compressibility

$$\beta_a = \frac{1}{u^2\rho} \quad (4)$$

(Eq. 5) to determine acoustic impedance

$$Z = \rho.u \quad (5)$$

(Eq. 6) to determine relaxation time

$$\tau = \frac{4}{3}\eta.\beta_a \quad (6)$$

(Eq. 7) to determine free length

$$L_f = K_j\beta_a^{1/2} \quad (7)$$

where K_j stand for Jacobson's constant.

2.3 Characterizations

In present work auther used UV spectrophotometer (UV-1800 pc) of Shimadzu Company for UV-vis characterization and Bruker Alpha FTIR instrument No. 10066587 for FTIR characterization and MHF-400 pulser receiver for ultrasonic characterization by pulse echo technique.

3. Results and discussion

3.1 Ultrasonic analysis

The following Figures 1(a), 1(b), 1(c), 1(d), 2(a), 2(b) and 2(c) discuss how thermo-acoustical properties change for various concentrations (wt%) at temperatures between 288 K and 308 K at 2MHz frequency:

The variation in ultrasonic velocity and density with concentration (wt%) is depicted in Figure 1(a) and 1(b). Viscosity (η) versus concentration (wt%) is plotted in Figure 1 (c).

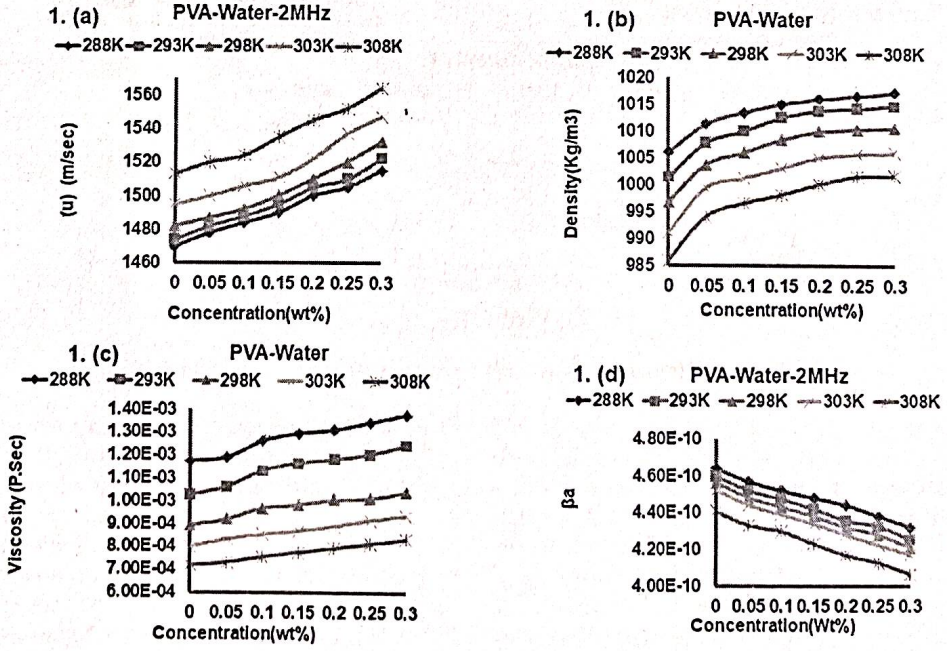

Figure 1: (a) ultrasonic velocity, (b) density, (c) viscosity, (d) adiabatic compressibility

It has been found that viscosity marginally increases as polyvinyl alcohol's weight percentage in water rises. According to Kauzman and Eyring, a mixture's viscosity is greatly influenced by its entropy, which is connected to both the liquid's structure and the interactions between its constituent molecules. As a result, molecular interaction as well as molecule size and shape have an impact on viscosity.In the study of molecular interaction, the measurement of viscosity in binary mixtures provides some trustworthy

information. The strength of the molecular interactions between interacting molecules is determined by viscosity [7].

The viscosity of the polyvinyl alcohol + water system is increased by the dipole-dipole interactions of the permanent dipoles in component molecules. The metric for intermolecular association, dissociation, or repulsion is called adiabatic compressibility. It also controls how the molecules that make up the parts are oriented.

The fluctuation of adiabatic compressibility (β_a) vs concentration (wt%) is shown in Figure1 (d). It has been found that as the concentration (wt.%) of polyvinyl alcohol in water increases, adiabatic compressibility decrease, indicating a significant intermolecular contact between the component molecules in this system and an associating property. It is obvious that several closely bound systems have formed in the PVA + Water system based on the rapid decrease in adiabatic compressibility with concentration increase. This might be brought on by a more rigid liquid structure linked to PVA's hydrogen bonds in water. Solvent molecules have been discovered to cause such a drop in compressibility in the solution [7]. According to Kiyohara and Benson, adiabatic compressibility is the product of a number of conflicting effects. The creation of hydrogen bonds between constituent molecules, interstitial accommodation, or strong dipole-dipole interactions all result in more compact structures and lower adiabatic compressibility. The observed increase in degree of connection in the component molecules is indicated by the decrease in adiabatic compressibility with concentration. Therefore, when concentration increases, the intermolecular distance reduces. The main factor that alters with structure and affects ultrasonic velocity is compressibility [7-8]. There is infinite contraction in the component molecules, as evidenced by a decrease in adiabatic compressibility. The molecules pack more tightly as adiabatic compressibility declines, which reduces the intermolecular free length. Through hydrogen bonds, the strong molecular connection between dissimilar molecules is strengthened as adiabatic compressibility increases. It is discovered that adiabatic compressibility (β_a) is practically reciprocal to acoustic impedance (Z).

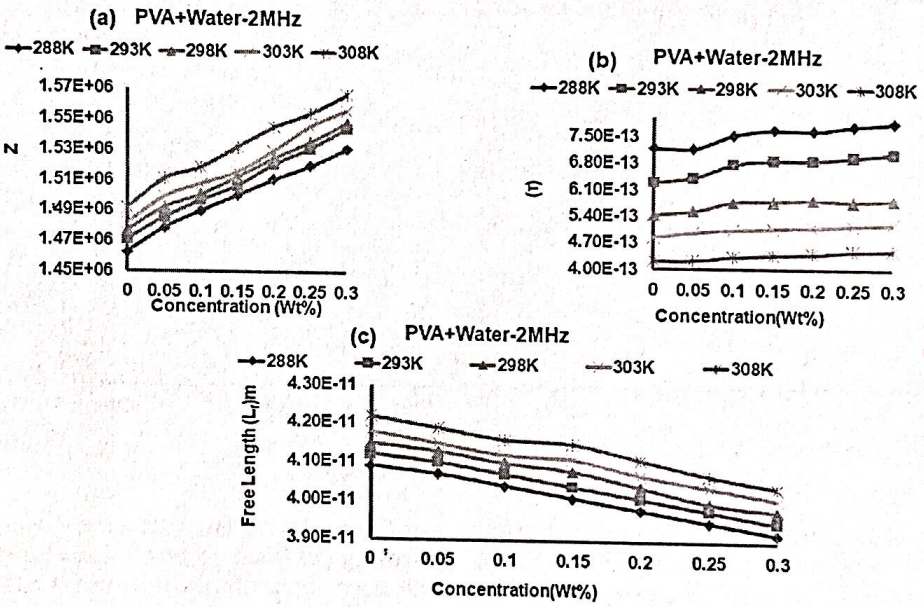

Figure 2: (a) Acoustic impedance, (b) Relaxation time, (c) Free length.

Acoustic impedance variation versus concentration can be seen in Figure 2(a). It has been found that when concentration (wt%) increases, so do the values of acoustic impedance. Because ultrasonic velocity increases with concentration, it satisfies the theoretical requirements. The decrease in intermolecular distance and relative decrease in gaps between the component molecules caused by intermolecular contact can be utilized to explaining the acoustic impedance (Z) increases with concentration. This implies that significant interactions are also present in this liquid system.

The Figure 2(b) shows the relationship between relaxation time and concentration (wt%). The fact that relaxation time slightly increases as polyvinyl alcohol content in water rises indicates that polyvinyl alcohol molecules are highly stable. Since polyvinyl alcohol has a tight structure and unstable molecules, the relaxation time is prolonged. Both the translational and the vibrational degrees of freedom can transmit energy, and both of these degrees are involved in the activity that is being seen [8]. Its behavior is determined by the liquid solution's viscosity and adiabatic compressibility. In this system, viscosity is crucial for lengthening relaxation times as concentration increases. With a rise in focus, the relaxation time rises. Due to its exceptional hydration, the solution is highly organized, and as a result, it is more likely to absorb ultrasonic energy[8-9]. Always expect that the mobility of the molecules in the solvent that is closest to the polymers will be lower than that of the molecules in pure solvent.

The curve of free length against concentration is shown in Figure 2(c). A measure of the intermolecular attraction between the constituents in binary mixes is the free length (L_f)

of a system. The intermolecular connection has weakened, as evidenced by the growth in free length. According to graphic behavior, free length decreases as polyvinyl alcohol concentration in water rises. Dipole-dipole interactions, hydrogen bonding-mediated association, or interstitial accommodation of dissimilar molecules if their sizes differ are all causes of a decrease in free length. Due to imperfect symmetry and a reduction in the amount of accessible space between the component molecules, free length decreases with concentration. Free length shortens as ultrasonic velocity quickens, exhibiting an inverse tendency that is well in line with the demands of theory. The decrease in free length as PVA concentration in water rises suggests that there are strong interactions between the solute and solvent, which may be supporting the behavior of the molecules in the binary solution that promotes structure. This results in an improvement of the closed structure, or an increase in the tightly packed structure of the component molecules. The increase in dipolar association, which creates strong hydrogen bonds in the molecules of the liquid mixes, may be the cause of the decrease in free length. Free length shortens as ultrasonic velocity quickens, exhibiting an inverse tendency that is well in line with the demands of theory. The decrease in free length as PVA concentration in water rises suggests that there are strong interactions between the solute and solvent, which may be supporting the behavior of the molecules in the binary solution that promotes structure. This results in an improvement of the closed structure, or an increase in the tightly packed structure of the component molecules. The increase in dipolar association, which creates strong hydrogen bonds in the molecules of the liquid mixtures, may be the cause of the decrease in free length [7-9].

3.2 FTIR analysis

FTIR analysis is shown in Figure 3.

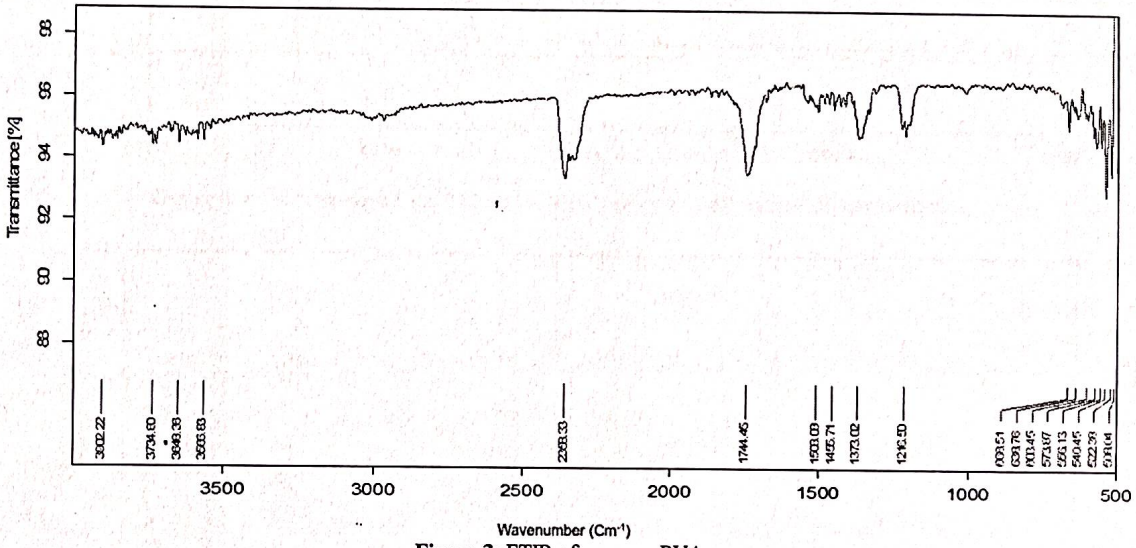

Figure 3: FTIR of aqueous PVA.

FTIR spectroscopy is a useful technique for identifying and investigating the presence of various functional groups in polymer solutions. The infrared spectra of various crystalline polymers have been extensively examined by polymer spectroscopists, but very little has been done to analyze the basic vibrations of organic polymers and copolymers. Because synthetic rubbers made of polyvinyl alcohol have such a wide range of industrial applications, it has been regarded as a significant polymer. The goal of the current inquiry is to examine the vibrational spectra of a polyvinyl alcohol polymer solution. Environmentally friendly and water soluble synthetic polymer with superior film-forming, emulsifying, and solvent- and oil-resistance capabilities is polyvinyl alcohol (PVA). Different weight percents of polymer solutions were created. Through FTIR spectroscopy, each material is examined for structural characteristics and miscibility behavior. We used a 1 (wt.%) aqueous PVA solution for the current FTIR investigation. The following graphic compares the FTIR spectra of aqueous Polyvinyl alcohol (PVA) in a 1 weight percent solution to that of pure PVA. The spectrum demonstrates the features of several functional groups, absorption, stretching, and bending frequencies. The spectral peak at 3648.36 cm^{-1} for the spectrum of an aqueous PVA solution is due to OH bonding. =C-H stretching (Olefinic) is thought to be responsible for the peak at 3000 cm^{-1}. C=O bending may be seen in the typical band at 1744.45 cm^{-1}. The C-C stretching (Aliphatic) and shifting are credited with causing the peak at 1373.02 cm^{-1}. C-O stretching and shifting is attributed to the spectral peak at 1216.50cm^{-1}.While the spectral peak at 3600 cm^{-1} in the spectrum of pure PVA is attributable to OH bonding. Between Pure PVA and an aqueous solution of 1 weight percent PVA, there is a slight shift in the OH bonding. Additionally, the peak for Pure PVA at 2917 cm^{-1} is due to =C-H stretching. As shown by the typical band at 1690 cm^{-1}, C=O bending. C-C stretching is also thought to be responsible for the peak at 1373 cm^{-1}. The 1081 cm^{-1} spectral peak is attributed to C-O stretching. Therefore, there is a slight wavelength shift in each peak. This indicates that there were no new bonds that were comparable to those in pure PVA were discovered in the aqueous PVA 1(Wt.%) solution. It is because the aqueous PVA solution has poor molecular interaction [10-13].

3.3 UV-visible analysis

Because it offers crucial details regarding the absorbance, transmittance, and reflectance of polymeric materials, UV-vis spectroscopy is a particularly intriguing approach [13]. PVA is a crucial polymer because it has excellent optical characteristics including great transparency. Figures 4 and 5 shows the UV absorbance spectra of aqueous PVA at various weight percentage concentrations.

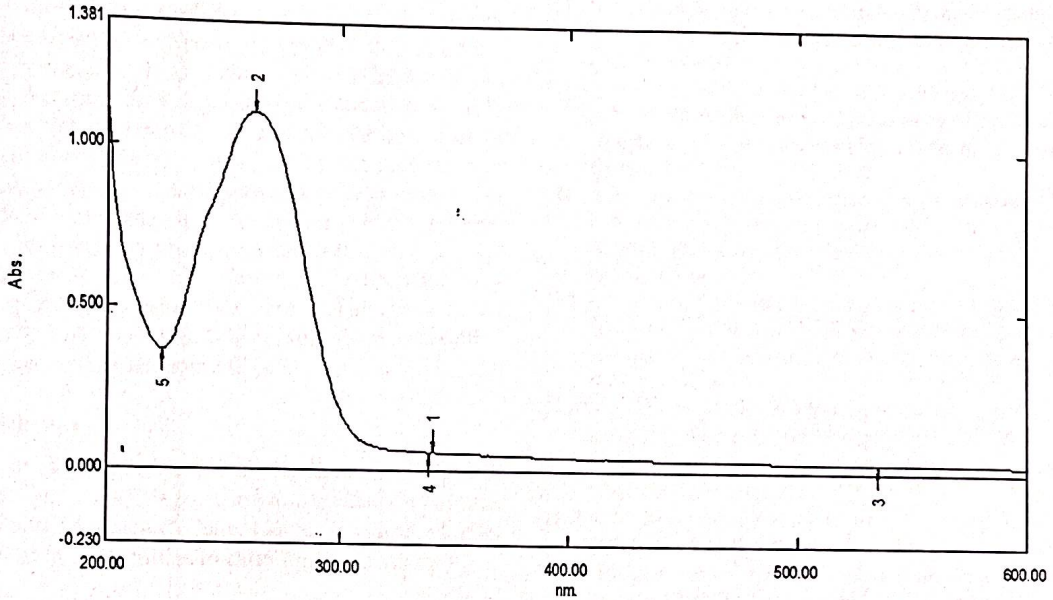

Figure 4: UV-vis aqueous PVA 0.05 wt.% solution (E_g.= 4.71 eV and λ=263 nm for peak-2.

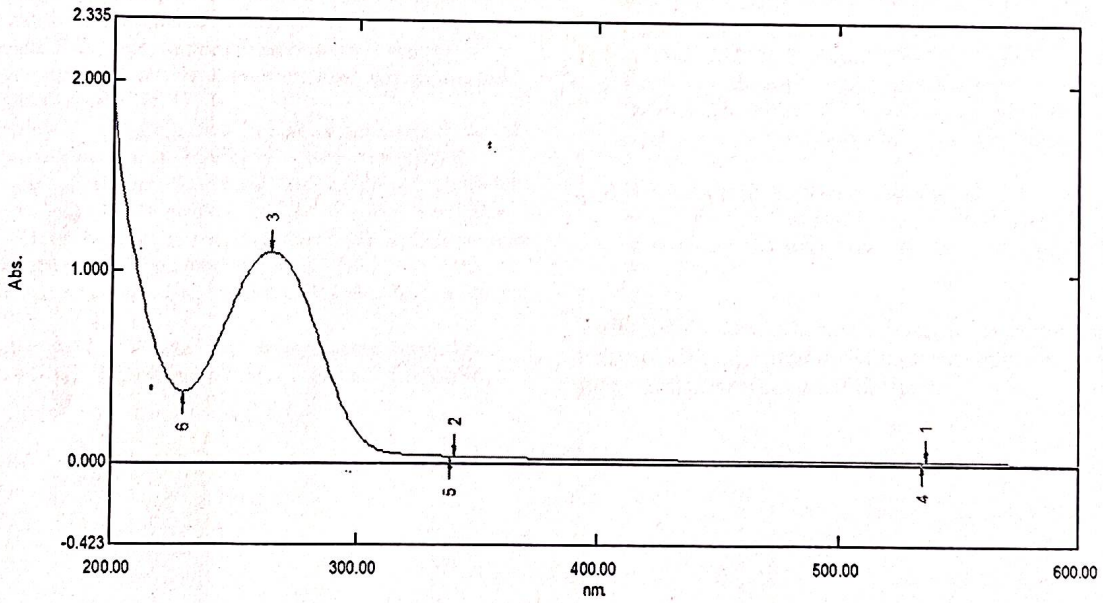

Figure 5: UV-vis aqueous PVA 0.25 wt.% solution (E_g = 4.58 eV) and λ=268.5 nm for peak-3.

PVA's absorbance spectra in water exhibits a distinctive peak at 194 nm that can be attributed to the compound's carbonyl groups C=O and C=C. There have been reports of a reasonably strong band at 270 nm, which is connected to the presence of residual acetate groups in PVA [13-15].

PVA exhibits distinctive absorbance bands associated to high-energy absorption at 263 nm for 0.05 wt%, 267.5 nm for 0.15 wt%, and 265 nm for 0.25 wt% solution. The electrical transitions n-* (R-band) and * (K-band) can be attributed to these bands, respectively. With a slight variation in the position of the bands at various concentrations (wt%) in the aqueous PVA solutions, all the bands seen in neat PVA. Thus, the UV-vis spectra revealed an absorption that was primarily in the UV region and barely detectable at visible wavelengths. For the peaks of various concentrations in weight percent listed below, energy band gaps are determined for the current inquiry. Sharp peak at wavelength 3 (or 268 nm) and energy band gap calculated as 4.62 eV are discovered for 0.25 weight percent. The peak is located at 2 (263 nm wavelength) and the energy band gap is 4.71 eV for 0.05 weight percent.

Additionally, it has been found that the energy band gap of the polymeric material reduces with an increase in the weight

percentage of the aqueous PVA solution. This leads to the conclusion that as concentration decreases, the energy band gap widens, increasing the dielectric characteristics of PVA.

4. Conclusions

The temperature affects thermoacoustical characteristics, which also depend on the concentration (wt%) of the polymer solution. The presence of weak polymer-solvent interactions is confirmed by the variation in acoustical characteristics (wt%) for various solutions. The spectral analysis clarifies specific chemical interactions that are confirmed by the measurement of thermo-acoustical characteristics. Research on thermoacoustical characteristics suggests that polymer solutions can form single phases and exhibit miscibility. FTIR study indicates that there were no new bonds that were comparable to those in pure PVA were discovered in the aqueous PVA 1(Wt.%) solution. It is because the aqueous PVA solution has poor molecular interaction.

Acknowledgements

The authors thanks to Head, P.G. Department of Physics; RTM Nagpur University, Nagpur, India and Head Department of Physics, Shivaji Science College, Congress Nagar, Nagpur, India for providing the facilities to carry out research work.

References

[1] D. Feldman, Poly (vinyl alcohol) recent contributions to engineering and medicine, *J. Comp. Sci.* **4** (2020) 175.

[2] R. Saxena, S.C. Bhatt, Molecular association studies on polyvinyl alcohol at different concentrations, *Adv. Mater. Sci. Eng.* (2018) Article ID: 1738612.

[3] P.K. Panda, K. Sadeghi, J. Seo, Recent advances in poly (vinyl alcohol)/natural polymer based films for food packaging applications: A review, *Food Pack. Shelf Life* **33** (2022) 100904.

[4] S.V. Khangar, O.P. Chimankar, R.Y. Bakale, Y.S. Tamgadge, S.H. Nimkar, S.G.B.A.U. Amravati, Frequency and temperature dependence of ultrasonic properties of aqueous PVA solutions using pulse-echo technique, *Int. J. Sci. Res. Sci. Tech.* **8** (2021) 299-303.

[5] S.V. Khangar, O.P. Chimankar, Ultrasonic investigation of dipole-induced interactions in binary solutions of cellulose aacetate with cyclohexanone and carbontetrachloride (CCl_4), *Int. J. Adv. Info. Sci. Tech.* **25** (2014) 25.

[6] S.V. Khangar, O.P. Chimankar, Ultrasonic characterization of aqueous polyvinyl pyrrolidone (PVP), *Phys. Sci. Int. J.* **4** (2014) 1352-1357.

[7] S.V. Khangar, O.P. Chimankar, Study of miscibility of aqueous polyacrylamide (PAA) solution, *Int. J. Eng. Innov. Tech.* **3** (2014) 148-150.

[8] S.U. Patil, , M.S. Deshpande, S.V. Khangar, O.P. Chimankar, A.N. Wagh, Molecular interaction study of linolic acid with α-tocopherol by ultrasonic technique, *Palegia Res. Library, Der-Chemica- Sinica* **6** (2015) 21-25.

[9] S.V. Khangar, O.P. Chimankar, D.V. Nandanwar, J.N. Ramteke, S.A. Kale, Study of highly viscous polyacryile measurements of viscosity and ultrasonic velocity, *J. Pure Appl. Ultrasonics* **41** (2015) 94-96.

[10] S.U. Patil, O. Chimankar, S.V. Khangar, M. Deshpande, Ultrasonic and spectroscopic investigation of polychloroprene and poly methyl methacrylate blends, *Proc. Mtgs. Acoust.* **38** (2019) 045018.

[11] H.S. Mansur, C.M. Sadahira, A.N. Souza, A.A. Mansur, FTIR spectroscopy characterization of poly (vinyl alcohol) hydrogel with different hydrolysis degree and chemically crosslinked with glutaraldehyde, *Mater. Sci. Eng. C* **28** (2008) 539-548.

[12] Y.S. Tamgadge, G.G. Muley, N.B. Thakre, S.V. Khangar, R.P. Ganorkar, R.Y. Bakale, Synthesis and nonlinear optical absorption of L-Valine capped Zn-doped MgO nanoparticles, *Macromolecular Symposia* **400** (2021) 2100021.

[13] T.A. Hamdalla, T. A. Hanafy, A.E. Bekheet, Influence of erbium ions on the optical and structural properties of polyvinyl alcohol, *J. Spectroscopy* (2015) Article ID: 204867.

[14] K. Deshmukh, M.B. Ahamed, R.R. Deshmukh, P.R. Bhagat, S.K. Pasha, AA. Bhagat, C. Lakhani, Influence of K_2CrO_4 doping on the structural, optical and dielectric properties of polyvinyl alcohol/K_2CrO_4 composite films, *Polymer-Plastics Tech. Eng.* **55** (2016) 231-241.

[15] H.S. Mansur, A.A. Mansur, CdSe quantum dots stabilized by carboxylic-functionalized PVA: synthesis and UV–vis spectroscopy characterization, *Mater. Chem. Phys.* **125** (2011) 709-717.

RP Current Trends In Applied Sciences
Vol. 2, No. 4 (October – December 2023) pp. 84–89
e-ISSN: 2583-7486

RESEARCH PLATEAU PUBLISHERS

Cite this article: R.Y. Bakale, Y.G. Bakale, Y.S. Tamgadge, R.P. Ganorkar, S.V. Khangar, Optical properties of polymethyl methacrylate/polyvinyl chlorideblends, *RP Cur. Tr. Appl. Sci.* 2 (2023) 84–89.

Original Research Article

Optical properties of polymethyl methacrylate/polyvinyl chlorideblends

R.Y. Bakale[1,*], Y.G. Bakale[2], Y.S. Tamgadge[3], R.P. Ganorkar[4], S.V. Khangar[5]
[1]Department of Physics, Mahatma Fule Arts, Commerce and Sitaramji Chaudhari Science Mahavidyalaya, Warud, Maharashtra, India
[2]Department of ESH, Kavikulguru Institute of Technology and Science, Ramtek, Maharashtra, India
[3]Department of Physics, Shri Shivaji Arts, Commerce and Science College, Motala, Buldana, Maharashtra, India
[4]Department of Chemistry, Mahatma Fule Arts, Commerce, and Sitaramji Chaudhari Science Mahavidyalaya, Warud, Maharashtra, India
[5]Department of Physics, Shri Shivaji Education Society Amravati, Science College, Congress Nagar, Nagpur, India
*Corresponding author, E-mail: reenabakale123@gmail.com

ARTICLE HISTORY
Received: 27 July 2023
Revised: 06 Dec. 2023
Accepted: 07 Dec. 2023
Published online: 07 Dec. 2023

KEYWORDS
Optical properties;
PVC/PMMA blends;
Optical constants.

ABSTRACT
We evaluated the optical parameters of doped polymer blends (PVC / PMMA). The energy gap (E_{opt}), absorption edge, optical permittivity, refractive index, constant B, $(n_0B)^{-1}$, and N/m* are composition-dependent. Increase the dopant concentration. The refractive index (n_0) was calculated in the range of 400 to 1000 nm and its linear or nonlinear behavior was also investigated with increasing Iodine content. The ratio of carrier concentration to the effective mass (N/m*) was evaluated.

1. Introduction

Polymer composites have grown steadily in importance over the past decade. The incorporation of transition metal salts into polyvinyl polymers, either pure or mixed in multiphase systems, can lead to large changes in various parameters of the polymers [1-3]. The study of the optical absorption spectra of solids provides important information about the band structure and energy gap of crystalline and amorphous materials. Analysis of the low-energy part of the absorption spectrum provides information about the vibrations of the atom, while the high-energy part of the spectrum provides information about the electronic state of the atoms.

The refractive index is an important parameter for the design of optical components such as prisms, windows, and optical fibers [4]. Polyaniline is used in light-emitting diodes in pure or doped form photovoltaic, sensors and supercapacitors [5]. Polyaniline is widely used as a research material due to the low cost of the monomer, ease of processing, and excellent stability [6, 7]. In transparent he studied conductive metal oxide thin films. Such transparent conductors are applied in a variety of active and passive electronic and optoelectronic devices [8], from aircraft windows to charge-coupled imaging devices [9]. Photoconductivity is one of the important classes of electro-optical properties of materials. Such studies are of interest because of the wide range of technical applications and the complexity of the phenomenon [10]. Sangwar and Mohari [11] studied the electrical, thermal, and optical band gaps of polypyrrole-filled PVC: PMMA thin films, using ammonium persulfate and p-toluenesulfonic acid as oxidants, Polypyrrole was prepared from pyrrole monomer by a chemical oxidation process, as a dopant.

Patel et al. [12] studied PVC/PMMA polymer blends were characterized by Fourier Transform Infrared Spectroscopy (FTIR), UV-VIS spectroscopy, and mechanical analysis. Ahmed [13] used a solution casting technique to create transparent films from (PMMA/PVAc) mixtures of different concentrations. To show the effect of UV radiation, we performed FTIR transmission spectra on the samples. In addition, absorbance measurements were taken at room temperature over the wavelength range 190-900 nm before and after exposure to UV and filtered radiation using a xenon arc lamp.

The work was extended to also include changes in the optical parameters such as band tail width and bandgap energy of the samples. In addition, refractive indices were calculated for samples from reflection and absorption spectra before and after exposure to UV and filtered radiation. The results indicated that no absorption minima are found in the visible wavelength range, indicating that all samples are colorless. Moreover, the increase in the refractive index values after 24 hours of exposure to UV light could be attributed to the increase in local density due to photo-induced cross-linking.

2. Objectives

The general theory of light absorption by amorphous semiconductors proposed by Mott et al. [14, 15] shows that

there are some Similarities between the energy band structure of crystalline and glassy non-metallic materials. Crystalline materials exhibit well-defined energy bands with sharp conduction and valence band edges. Glassy materials exhibit band-tailing into the normally forbidden gap [16].

Absorption at slightly higher energies (related to absorption coefficient $\alpha \geq 10^4$) can provide information about the combined density of states at the valence and conduction band edges. There are two types of optical transitions that can occur at edges in crystalline semiconductors, direct or indirect the theory of such transitions was advanced by Davis et. al [17] presentation. Both involve the interaction of electrons in the valence band with electromagnetic waves, facilitated across the fundamental gap to the conduction band.

For indirect transitions, however, there is also a simultaneous interaction with lattice vibrations. Therefore, an electron's wave vector can change during an optical transition, and the momentum change can be absorbed or emitted by the photon (radiation gives the electron negligible momentum). For amorphous materials, localized electronic states within the mobility gap are fundamentally considered. The matrix element $D(E)$ of the optical transitions between yes in different bands has the same value regardless of whether the initial states and the states are localized.

Furthermore, the density of states at the band edges is assumed to be a linear function of energy. Furthermore, transitions are unlikely if both the initial and final states are localized [17]. Mort et. al [15] have reported the general theory of optical absorption in amorphous semiconductors.

The optical absorption coefficient $\alpha(\upsilon)$ at a frequency υ is given by

$$\alpha(\vartheta) = \frac{4\pi\sigma_{min}}{cn_0\Delta E}\frac{h\vartheta - E_{opt}}{h\vartheta}^{r}. \quad (1)$$

The reflectance [17] can be calculated using the equation given by

$$T = (1 - R)\exp(-A). \quad (2)$$

The relation between the optical dielectric constant (ϵ') and the square of wavelength (λ^2) is given by [18, 19]

$$\epsilon' = \epsilon'_{\infty}\frac{e^2}{\pi c^2}\frac{N}{m^*}\lambda^2. \quad (3)$$

3. Materials and methods

Preparation of sample

The polyvinyl chloride (PVC) of standard grade product supplied by Polychem Industries Mumbai and polymethyl methacrylate (PMMA) supplied by Dental Product of India Ltd., Mumbai was used for the study. The two polymers PVC (1.5 g) and PMMA (0.5 g) were taken in the ratio of 3:1 by weight. The 1.5 g of PVC in 20 ml of tetra hydrofuran (THF) and 0.5 g of PMMA in 10 ml tetra hydrofuran were dissolved separately. After complete dissolution, the two solutions were mixed together. Iodine was added in weight percent to prepare the iodine-doped blend films, 0.2%, 0.4%, 0.6%, 0.8%, 1.0%. Each was dissolved in 5 ml of THF to prepare an iodine solution.

The iodine solution was later mixed with a homogeneous solution of PVC and PMMA. The total volume of solvent was kept constant at 35 ml. The solution was heated at a constant temperature of 333 K for 2 hours to completely dissolve the polymer and obtain a clear solution. A glass plate (15 cm × 15 cm) was used as a substrate and washed thoroughly with hot water and then with acetone.

To achieve perfect leveling and thickness uniformity of the film, the film was prepared on a thoroughly cleaned optically flat glass plate while floating in a mercury bath. The entire assembly was placed in a dust-free chamber maintained at a constant temperature (313 K). Thus, films were prepared by isothermal evaporation technique [22, 23]. The film was heated at a constant temperature of 323 K for 12 hours and at room temperature for another 12 hours to remove traces of solvent. Finally, the film was peeled off from the glass plate. It was cut into appropriately sized pieces and washed with ethyl alcohol to remove the surface contaminants.

Thickness Measurement

For increased accuracy and resolution, a compound microscope was used in combination with an accelerometer to measure minimum counts of 13 μm and 3.3 μm at the magnification of 1:10 and 1:100, was used. A small section of the sample was taken and mounted vertically to obtain a clear cross-section of the thickness. The thickness of the film used in this study is approximately 80 μm.

4. Results

The absorbance 'A' and transmittance 'T' of simple were measured at both normal incidence over the spectral range 400-1000 nm using a CART 2390 double beam auto scanning spectrophotometer (within the Regional Sophisticated Instrumentation Centre, Chennai) The 'A' and 'T' on doping rates of iodine thin films are shown in Figure 1 and Figure 2.

The results for the various optical properties listed in Table 1 and the iodine percentage are shown in Figure 3. The observed behavior indicates a forbidden direct transition for amorphous materials.

Similar behavior was reported by Tembhurkar et. al [24] and Deshmukh et. al [25] reported. The values of optical energy gap E_{opt} obtained from the extrapolation of the linear range and the constant B from the slope of the curve shown in Figure 3 are given in Table 1 respectively. Note that the value obtained by E_{opt} increases with ancestry from J_{od}. Similar behavior was reported by Deshmukh et. al [25] observed. The value of the absorption edge [24] is calculated from Figure 2 and summarized in Table 1.

Note that the values obtained for the absorption edge increase with the dopant percentage.

Table 1: Variation of Optical energy gap (E_{opt}), absorption edge, infinitely high-frequency dielectric constant (ε'_∞), refractive index (n_0), Constant B, the ratio of carrier concentration to the effective mass (N/m*) for different samples.

Sample PVC+PMMA+ % of dopant iodine	(E_{opt}) eV	Absorption edge (eV)	ε'_∞	Refractive index (n_0)	Constant B (cm^{-2} eV)	(N/m*) cm^{-3}	$(n_0B)^{-1}$ (cm^2 eV^{-1})
A1 0.2%	1.23	1.22	13.05	2.88	1.16×10^4	0.49×10^{21}	29.77×10^{-6}
B1 0.4%	1.26	1.24	12.37	2.81	1.02×10^4	0.28×10^{21}	34.79×10^{-6}
C1 0.6%	1.28	1.27	16.01	3.19	1.55×10^4	0.48×10^{21}	20.07×10^{-6}
D1 0.8%	1.31	1.30	10.41	2.69	1.15×10^4	0.46×10^{21}	32.27×10^{-6}
E1 1%	1.33	1.34	9.96	2.57	0.17×10^4	0.32×10^{21}	22.22×10^{-6}

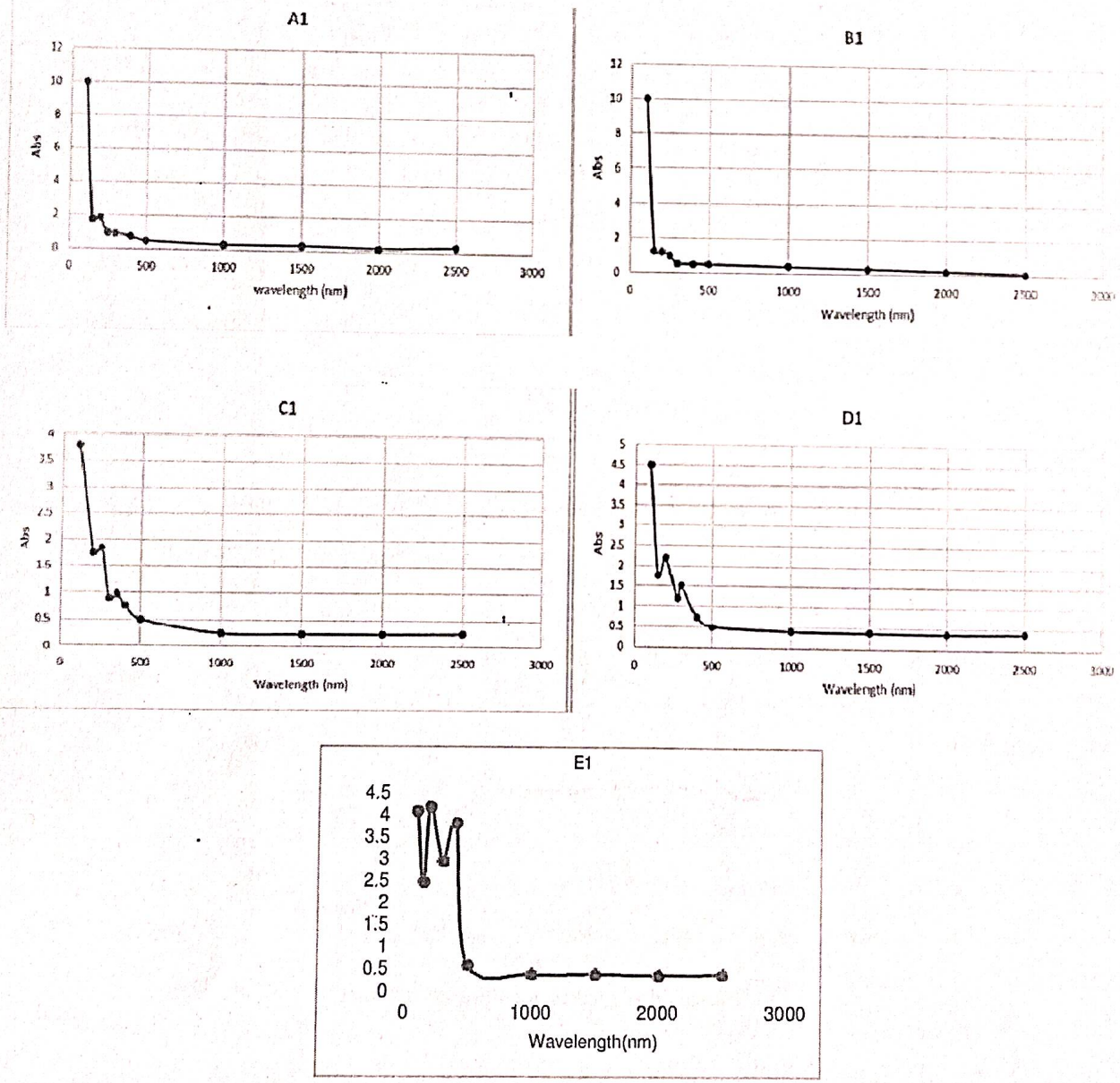

Figure 1: Absorbance spectra of iodine-doped film.

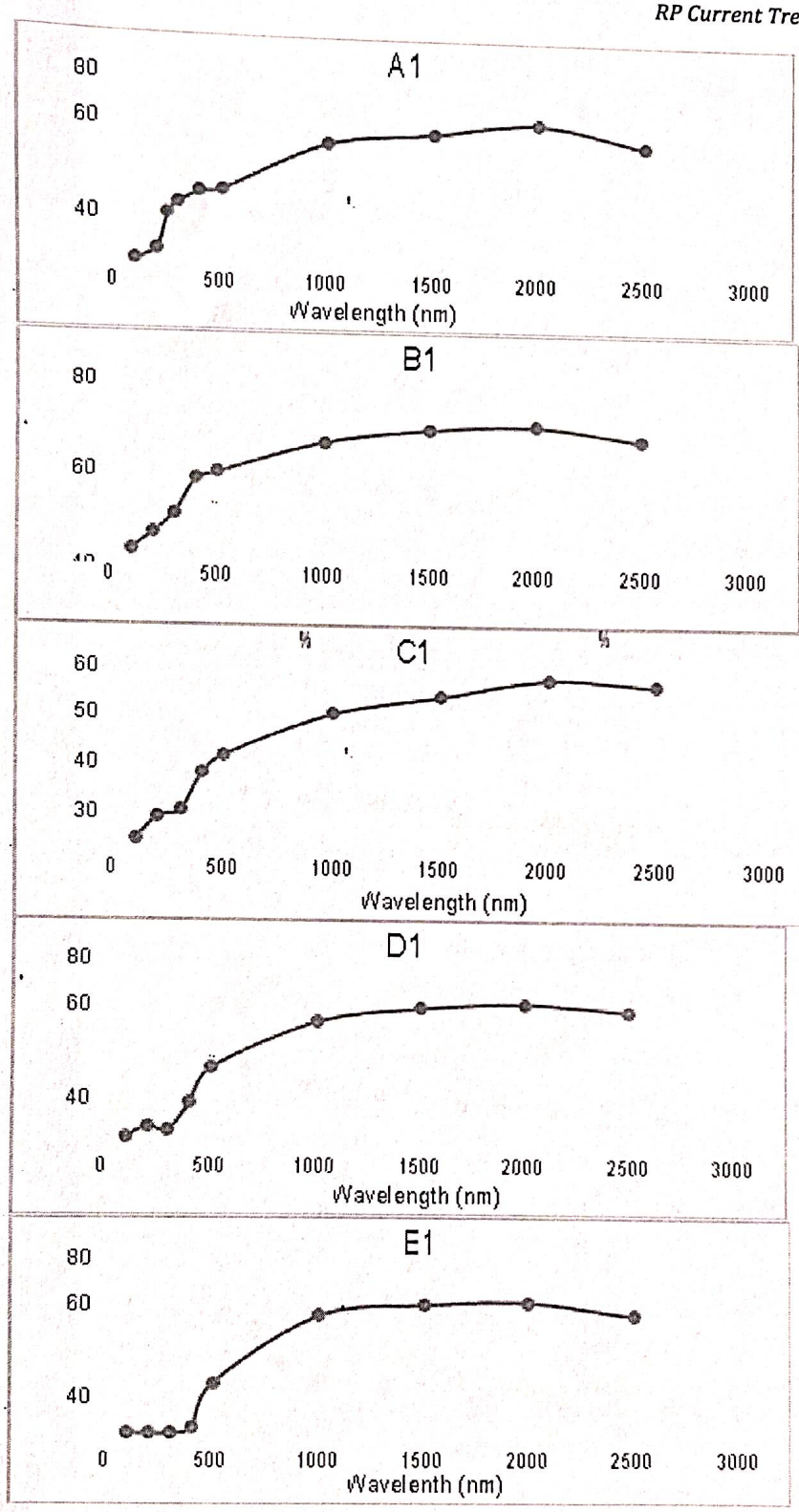

Figure 2: Transmittance spectra of iodine-doped films.

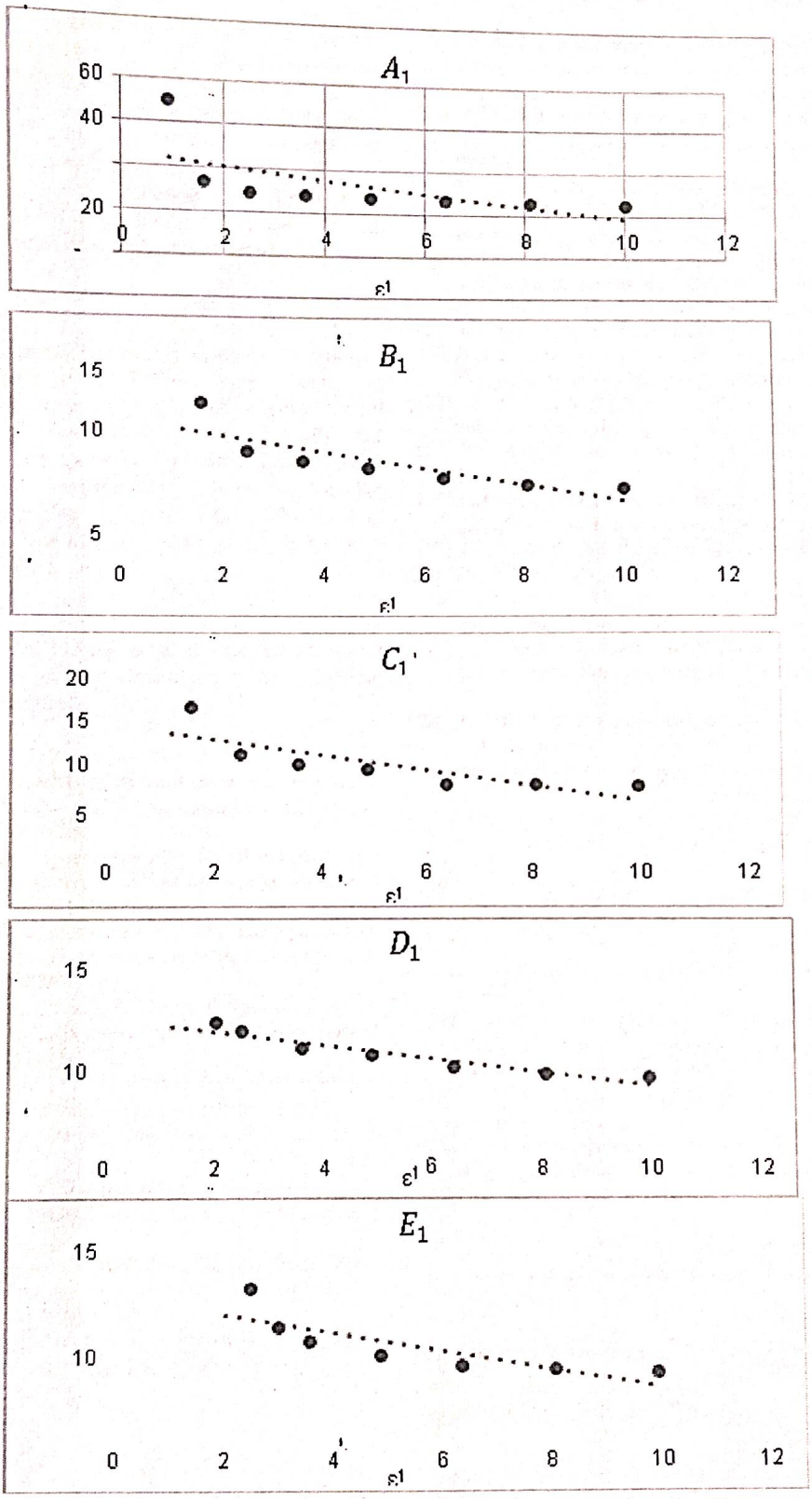

Figure 3: Variation of ε' versus $\lambda^2 \times 10$.

5. Discussions

The calculated value of $(n_0B)^{-1}$ is nonlinear. A similar observation was made in his $G_{20}Te_{80-x}Se_x$ thin films reported by Shokr et. al [26] and by Deshmukh et. al [25] was considered. A plot of permittivity $\in'$ versus λ^2 is shown in Figure 3 is linearity according to Equation 3 (effective mass carrier concentration) is shown in Table 1. Refractive index (n_0) and dielectric constant ($\in'$) values are nonlinear for all samples.

Such nonlinear behavior is observed in amorphous materials [25, 26]. The refractive index and optical permittivity are calculated over the wavelength range of 400 nm to 1000 nm. The refractive index values are nearly identical over the entire wavelength range (400 mm to 1000 nm). Therefore, the average value n_0 is given over this wavelength range.

The ratio of charge carrier concentration to the effective mass N/m* was calculated from the slope of the curve ϵ' versus λ^2. Figure 3 is consistent with values reported by other workers [25-28].

6. Conclusions

It can be concluded that the evaluated optical parameters of doped polymer blends (PVC / PMMA doped with iodine) such as optical energy gap (E_{opt}), absorption edge optical dielectric constant, refractive index, constant B. $(n_0B)^{-1}$ and N/m* are found to be compositional dependent. The refractive index (n_0) (Calculated in the range 400 to 1000 nm) is found to be nonlinear with increasing content of iodine. The ratio of carrier concentration to the effective mass (N/m*) is found to be of the order of 10^{21} cm^{-1}.

Acknowledgements

The authors also wish to put on record sincere thanks to the Regional Sophisticated Instrumentation Centre, Chennai for characterization Facilities.

References

[1] F.H. Abd El-Qader, S.A. Gafar, Study of thermal currents in $CoCl_2$-doped poly (vinyl alcohol) films irradiated with γ-rays, *J. Polim. Mater.* **10** (1993) 245.

[2] W.H. Osman, Study of optical properties of pure and MoO_3-doped polyvinyl alcohol films irradiated with γ-rays, *J. Mater Sci. Master of Electronics* **7** (1996) 1.

[3] N.H. Barkoula, K. Kocsis, Processes and influencing parameters of the solid particle erosion of polymers and their composites, *J. Mater. Sci.* **37** (2002) 3807.

[4] H.L. Ma, X.H. Zhang, J. Lucas, R. Lizaka, T. Yamagishi, T. Yamashita, Refractive index measurement of the TeX glasses, *J. Non-cryst. Solids* **161** (1993) 198.

[5] J. Mathai, S. Saravanan, M.R. Anantharaman, S. Venkatachalam, S. Jayalekshmi, Effect of iodine doping on the bandgap of plasma polymerized aniline thin films, *J. Phys. D. Appl. Phys.* **35** (2002) 2206.

[6] C. Agashe, S. Mahamuni, Doping induced changes in the physical properties of In_2O_3: Sn films, *Semicond. Sci. Technol.* **10** (1995) 172.

[7] S. Shanti, C. Subramaniam, P. Ramasamy, Optical properties of undoped, fluorine doped and antimony doped tin oxide films, *Cryst. Res. Technol.* **34** (1999) 1037.

[8] K.L. Chopra, S. Major, D.K. Pandya, Transparent conductors – A status review, *Thin Solid Films* **102** (1983) 1-46.

[9] J.S. Bhat, K.I. Moddani, A.M. Karguppikar, Influence of Zn doping on electrical and optical properties of multilayered tin oxide thin film, *Bull. Mater. Sci.* **29** (2006) 331.

[10] M. Mukharjee, P. Bose, Electro-optical studies in chemically deposited Sm/Pr doped (Cd-Pb) S film, *Ind. J. Pure Appl. Phys.* **39** (2001) 804.

[11] V. Sangawar, N. Moharil, Study of electrical, thermal and optical behavior of polypyrrole filled PVC: PMMA thin film thermo electrets, *Chem. Sci. Trans.* **1** (2012) 447-455.

[12] G. Patel, M. Suresh Kumar, P. Patel, Structural, optical and mechanical properties of PVC/PMMA polymer blend by spectroscopic techniques, *AIP Conf. Proc.* **1391** (2011) 645.

[13] M. Ahmed "Optical Study on Poly (methyl methacrylate)/ Poly (vinyl acetate) Blends", Vol.57, No.10*"International Journal of Polymeric Materials"* (2008) pp. 969-978.

[14] N.F. Mott, E.A. Davis, *Electronic process in non-crystal materials*, Clarendon Press, Oxford (1979).

[15] N.F. Mott, Electrons in disordered structures, *Adv. Phys* **16** (1967) 49-144.

[16] T.H. Rashed, G. Salem Abd. El, Optical absorption in zinc phosphate glasses, *Ind. J. Pure Appl. Phys.* **22** (1984) 185.

[17] T.S. Moss, *Optical Properties of Semiconductors*, Academic Press, New York (1959).

[18] C.I.F. Bottcher, *Theory of Electric Polarization,* Elsevier, Amsterdam (1952), p. 376.

[19] W.G. Spitzer, H.Y. Fan, Determination of optical constants and carrier effective mass of semiconductors, *Phys. Rev.* **106** (1957) 882.

[20] J.P. Hirde, Y.D. Tembhurkar, Optical and structural properties of II-VI solid-solution thin films of $Cd_xZn_{1-x}S$ deposited by spray pyrolysis, *Ind. J. Pure Appl. Phys.* **28** (1990) 585.

[21] Y.D. Tembhurkar, J.P. Hirde, Structural, optical and electrical properties of spray pyrolytically deposited films of copper indium diselenide, *Thin Solid Films Bull. Mater Sci.* **15** (1992) 143-148.

[22] A. Narayan, H.P. Singh, Electrical conduction in semiconducting PVC-PMMA thin film, *Ind. J. Pure. Appl. Phys.* **25** (1983) 30.

[23] R. Bahri, B.R. Sood, Effect of iodine doping on photoconductivity of polystyrene thin films, *Thin Solid Film,* **100** (1983) L5.

[24] Y.D. Tembhurkar, J.P. Hirde, Structural, optical and electrical properties of spray pyrolytically deposited films of copper indium diselenide, *Bull. Mater Sci.* **15** (1992) 143-148.

[25] S.H. Deshmukh, *PhD Thesis*, SGB Amravati University, Amravati (2007).

[26] E. Kh. Shokr, Optical properties of glassy $Ge_{20}Te_{80-x}Se_x$ thin films, *Ind. J. Pure Appl. Phys.* **30** (1992) 271.

[27] S.B. Sawarkar, *Ph D Thesis,* Amravati University, Amravati (2002).

[28] D.K. Burghate, V.S. Deogaonkar, S.V. Pakade, S.P. Yawale, Optical properties of lead-bismuth-titanate glasses, *Ind. J. Pure Appl. Phys.* **33** (1995) 683.

ISSN : 2347-4777

INTERNATIONAL JOURNAL OF CULTURAL STUDIES AND SOCIAL SCIENCES

(UGC approved Multi-disciplinary Peer-Reviewed Journal)
UGC Journal Serial No.49228 in 2019 list
Currently Indexed in UGC CARE LIST, Serial No.159 in 2022 list

Vol-20, Issue-1, No.20, January - June: 2024

Eds.
Amitava Roy, Ronan Paterson,
Bryan Reynolds, Subir Dhar, Papia Mitra

A Special Publication of
Tagore Gandhi Institute
The Shakespeare Society of Eastern India.

ap

Dr. Dinesh Dhage
20-26

INTERNATIONAL JOURNALOF CULTURAL STUDIES AND SOCIAL SCIENCES

(UGC CARE approved Multi-disciplinary Peer-Reviewed Journal)

Vol. - XX, Issue-1, No.20, January-June: 2024

ISSN : 2347-4777

AVANTGARDE PRESS

TAGORE–GANDHI INSTITUTE / SHAKESPEARE SOCIETYAVANTGARDE PRESS

International Journal of Cultural Studies and Social Sciences

बॅकींग क्षेत्राचे शेती क्षेत्राच्या विकासात योगदान

प्रा. दिनेश महादेव ढगे, श्री शिवाजी कला, वाणिज्य व विज्ञान महाविद्यालय, मोताळा जि. बुलढाणा
dineshmdhage@gmail.com Mobile No 9922515030

प्रस्तावना:-

प्रत्येक देशाच्या आर्थिक विकासात बँकिंग क्षेत्र अत्यंत महत्वपुर्ण स्वरूपाचे आहे. भारतात पाष्चात्त्य बँकिंग प्रणालीची सुरूवात 19 व्या शतकाच्या प्रारंभी झाली. ईस्ट इंडिया कंपनीच्या कर्मचा-यांची सुरू केलेल्या त्यावेळेच्या वाणिज्य अधिकोशांना 'एजन्सी हाउसेस'असे म्हणत असत. पहिली संयुक्त भांडवली बॅक म्हणुन 'बॅक ऑफ हिंदुस्थान'या नावाने ओळखण्यात येवु लागली. सन 1905 मध्ये सुरू झालेल्या स्वदेशी चळचळीने भारतीय बॅकांच्या स्थापनेला चालना मिळाली. सन 1920 मध्ये प्रांतीय बॅकांचे एकत्रिकरण करून 'इंपिरियल बॅक'निर्माण करण्यात आली. त्याच बँकेचे पुढे केंद्रीय बॅकेत रूपांतर करण्यात आले. सन 1955 पर्यंत तिचे स्थान फार महत्वपुर्ण होते. या 1955 मध्ये बॅकांचे एकत्रिकरण करण्यात आले. व स्टेट बॅक ऑफ इंडियाची निर्मिती करण्यात आली. वाणिज्य कायदा करून बॅकेच्या व्यवहारांचे नियमन करण्याचे व्यापक अधिकार आर. बी. आय. ला देण्यात आले. भारताच्या आर्थिक विकासात सुध्दा बॅकांची भुमिका महत्वपुर्ण दिसुन येते. शेती व्यवसायाला भारतीय अर्थव्यवस्थेचा कणा म्हटले जाते. त्यामुळे निश्चितच शेती क्षेत्राचा विकास म्हणजे भारतीय अर्थव्यवस्थेला बळकट स्वरूप प्राप्त करून देणे होये. त्यामुळे भारताच्या सर्वांगीण विकासाकरीता भारतीय बॅकांनी शेतीश्रेत्रात महत्वपुर्ण भुमिका निभावलेली दिसुन येते.

शेती विकासात योगदान:-

दिनांक 19 जुलै 1969 या दिवशी भारत सरकारने 14 प्रमुख बॅकांचे राष्ट्रीयकरण केले. ज्या बॅकांचे राष्ट्रीयकरण करण्यात आले त्या बॅकांचा अधिकार भारत सरकार ला देण्यात आला. भारतीय कृषी व ग्रामीण अर्थवस्थेला अधिक बळकट करण्याकरीता या कायदयाचा आधार घेवुन पुढे सन 1980 ला परत बॅकांचे राष्ट्रीयकरण करण्यात आले त्यामुळे पुढील उद्देश दिसुन येतात.

1) बॅकांवरील मुठभर उद्योगपतीचे नियंत्रण दुर करणे.
2) शेती लघुउद्योग व निर्यात क्षेत्रांना आवश्यक प्रमाणात कर्ज सुविधा उपब्लध करून देण्यात याव्यात.
3) बॅक व्यवस्थापन कायदे व्यावसायीक दृष्टीकोणातुन व्हावे.
4) नविन शेती उद्योगांना सुलभ व सहज वित्तपुरवठा व्हावा व उत्तेजन मिळावे.
5) बॅक कर्मचा-यांना आवश्यक अशा प्रशिक्षण सेवा सुविधा मिळाव्यात.

यापासुन भारतीय बॅक व्यवसायाचे काम फार पुर्वीपासुन झालेले दिसुन येते. त्यामुळे सावकार व सराफीवर्ग यापासुन शेतक-यांची लघुउद्योगाची तसेच मजुरांची होणा-या पिळवणुकीपासुन सुटका झाली. त्यामुळे बॅकेच्या राष्ट्रीयकरणामुळे भारतीय शेतीच्या विकासाला चालना मिळाली. ज्यामुळे बॅकांच्या शाखांचा विस्तार झाला. त्याचा उपयोग शेती लघुउद्योग व शेतीपुरक व्यवसायांना भांडवलाचा पुरवठा वाढत्या प्रमाणात व्हायला सुरूवात झाली. बॅकांचे राष्ट्रीयकारणामुळे सन 1996 मध्ये 34000 बॅकांच्या शाखा दिसुन येतात. त्यापैकी 75 टक्के शाखा खेडयातुन उद्यडण्यात आल्यात. कारण भारत हा खेडयाचा देश म्हटला जातो. बहुतांश खेडयातील जनता ही शेतीवर अवलंबुन आहे. त्यामुळे शेतीचा विकास हा खेडयांच्या विकासावर दिसुन येतो. त्यादृष्टीने या बॅकेच्या शाखाच्या विस्ताराची सरासरी शेतकरी लोकसंख्या 65000 वरून 14000 पर्यंत कमी झाल्याचे दिसुन येते. त्यामुळे निश्चितच शेतकरी व शेतीचा विकास झालेला दिसुन येतो.

मार्च 2011 अखेर पर्यंत बॅकांचा ग्रामीण भागातील शेतीच्या विकासाकरीता झालेला विस्तार दिसुन येतो.

बॅकेचे नाव	ग्रामिण शाखा	शहरी शाखा	एकुण
सार्वजनिक श्रेत्रातील बॅका राष्ट्रीयकृत बॅक 20 स्टेट बॅकसमुह 06	20387 14185 6202	41824 30113 11712	62291 44290 17913
ब. खाजगी श्रेत्रांतील बॅका जुन्या खाजगी बॅका 14 नविन खाजगी बॅका 7	1311 764 547	10291 4093 6238	11602 4817 6785
क. परकीय बॅका 36	07	310	317

वरील माहीती ही आर. बी. आय. च्या बुलेटीन डिसेबर 2011 मध्ये दिलेल्या सर्वेवरून असे दिसुन येते की सार्वजनिक व खाजगी बॅका यांनी ग्रामीण भागात शाखा उघडण्यास सुरूवात मोठया प्रमाणावर केलेली आहे. सन 1969 मध्ये 65000 लोकांमागे एक बॅक असे प्रमाण होते ते प्रमाण बदलुन कमी झाल्याचे दिसुन येते. याकरीता सन 2010-2011 साली 13466 इतके प्रमाण कमी झालेले दिसुन येत आहे. यावरून असे लक्षात येते की, भारतीय अर्थव्यवस्थेला बळकट करण्याच्या दृष्टीकोनातुन विविध बॅकांचे आर्थिक योगदान तथा भांडवलाचे प्रमाण, शेती, शेतीपुरक व्यवसाय, लघुउद्योग याकरीता हे वाढते आहे. आणि यामधुन भारतीय अर्थव्यवस्थेला अधिक बळकट व विकासीत करण्याकरीता ज्या शेतीला भारतीय अर्थवस्थेचा कणा असे म्हणतो त्या शेतीला सर्वागीन विकसीत करण्याकरीता भारतीय बॅकींगचे अधिक सुलभ व मोठया प्रमाणावर योगदान दिसुन येते. याचा परीणाम म्हणजे देशातील शेतकरी हा बॅकींगच्या, विकासाच्या वर्तुळात ओढला गेला. कधीतरी आपला देश अन्नधान्याच्या बाबतीत इतर देशावर अवलबुंन होता. तो यानंतर केवळ स्वावलबीत झाला असे नाही तर अतीरीक्त अन्नधान्य निर्यात करू लागला. त्याबरोबरच शेतीकरी गाई म्हसी पाडु लागला. दुधाचा व्यवसाय करू लागला. आणि यासाठी सार्वजनिक श्रेत्रातील बॅका कर्ज देवु लागल्या. यातुन दुग्ध क्रांती शक्य झाली. शेतकरी शेळया, मेंढया, कोंबडया पाळू लागल्या. मासेमारीचा यासारखे व्यवसाय करू लागली. फळबाग तयार करू लागला. यातुन निर्सगाच्या मनमानीमुळे अस्थिर जिवन जगणा-या शेतक-यांला पुरक उद्योगांचा आधार मिळु लागला. शेतक-यांच्या जीवनात स्थैर्य निर्माण होउ लागले. दरडोई उत्पन्नात वाढ होउ लागली. तसेच राष्ट्रीय सकल घरेलु उत्पादनात, राष्ट्रीय उत्पनात देखील शेतीचा वाटा वाढला. शेती व पुरक उद्योगात मोठया प्रमाणात रोजगार निर्माण झाला. यावरून असे दिसुन येते की भारतीय बॅकींगचे योगदान शेती क्षेत्राच्या विकासामध्ये अनन्य साधारण महत्व आहे हे सुर्यप्रकाशासारखे सत्य आहे.

संदर्भः-

1. भारतीय अर्थव्यवस्था - रंजन कोळंबे
2. पैशा आणि वित्तीय रचना - डॉ. सी. जे. जोशी, ए. सी. जोशी
3. आर.बी.आय. मथली बुलेटीन डिसेबर 2011, 2012, 2016
4. भारतीय अर्थव्यवस्था - प्रा. प्र. रा. कुलकर्णी